



Improving Methods for X-ray Absorption Spectroscopy Studies of Metalloproteins

Molich, Ulf

Publication date:
2020

Document Version
Publisher's PDF, also known as Version of record

[Link back to DTU Orbit](#)

Citation (APA):
Molich, U. (2020). *Improving Methods for X-ray Absorption Spectroscopy Studies of Metalloproteins*. Technical University of Denmark.

General rights

Copyright and moral rights for the publications made accessible in the public portal are retained by the authors and/or other copyright owners and it is a condition of accessing publications that users recognise and abide by the legal requirements associated with these rights.

- Users may download and print one copy of any publication from the public portal for the purpose of private study or research.
- You may not further distribute the material or use it for any profit-making activity or commercial gain
- You may freely distribute the URL identifying the publication in the public portal

If you believe that this document breaches copyright please contact us providing details, and we will remove access to the work immediately and investigate your claim.

Improving Methods
for
X-ray Absorption Spectroscopy
Studies
of
Metalloproteins

PhD Thesis
Ulf Molich

X-ray Group
Department of Chemistry
Technical University of Denmark

Preface

This dissertation was written as a conclusion to three years' work between December 2015 and December 2019 to achieve the doctoral degree at the Technical University of Denmark in Kongens Lyngby. The work has primarily been carried out in the X-ray group at the Department of Chemistry, under supervision of Professor Pernille Harris (main supervisor) and Emeritus Kenny Ståhl (co-supervisor). Part of the work was carried out at the MAX IV Facility in Lund, Sweden under supervision of Dr. Kajsa Sigfridsson Clauss. The scholarship was paid for by the Department of Chemistry and the European Union Interreg project ESS&MAX IV Cross Border Science and Society, MAX4ESSFUN, DTU-003.

First, I would like to thank my supervisors, Pernille Harris and Kenny Ståhl, for accepting me as a PhD student, for their great support, their wise inputs, their relaxed nature, and their tongue-in-cheek sense of humor. Their perception of science and their decency have been a great inspiration, and their dedication to obtain results on our synchrotron trips has been invaluable.

Special thanks goes to Kajsa Sigfridsson Clauss for her collaboration on the flow cell project, invaluable help on synchrotron trips, and assisting with the following data treatment. Her highly professional inputs have been instrumental in the work related to this dissertation.

I would like to thank Christian Grundahl Frankær for introducing me to the software and method of X-ray absorption spectroscopy, and him and his student, Christian Sørensen, for preparing samples and collecting data on plastocyanin. In that regard, I would also like to thank David Frej Nielsen for helping me prepare fresh plastocyanin samples.

I thank Arun Kumar Somavarapu, Daniel Szunyogh, Kasper Planeta Kepp, and Lars Hemmingsen for introducing me to the preparation protocol on amyloid- β and for valuable input on the project.

I would like to thank Aghiad Ghazal and Dörthe Haase for their fruitful collaboration and help in the flow cell project.

I would also like to thank the beamline staff at both at SAMBA at SOLEIL and BM30B FAME at ESRF for their support, and DanScatt for funding the synchrotron trips.

I owe Norman Binsted thanks for supporting me on the use *Excurve*, and Yves Joly for support and discussions on the use of *FDMNES*, as well as being great company at two XAFS conferences.

Much appreciation goes to Line Ryberg and Tine Frimann for following my path from September 2010 when we started our studies together, until they finished their respective PhD studies, but also for their inputs, discussions, and the many social events we have enjoyed together.

I would like to thank the many people with which I have shared office; Maria Blanner Bang, Alexandre Voute, Jinfang Li, Diptesh Dey, Natalia Skawińska and Andreas Tosstorff for their fantastic mood, and scientific and political discussions; the colleagues that I have shared Friday breakfasts with and the rest of the people at the Department of Chemistry, many of whom I have talked to about my project.

Thank you to Nicklas Møller for beating me, Friday after Friday, in the honorable game of foosball, but also for taking my mind off my work when needed.

Finally, I would like to thank my brothers and parents for bearing with my absence, both physically and mentally, during the last few months, and for helping me when I needed it. In that regard, a special thanks to my wonderful girlfriend, Helene, who have taken care of any issues that could have distracted me in the final months of writing, for her patience, and for her love, for which I am deeply grateful.

Kongens Lyngby, December 14, 2019

Ulf Molich

Abstract

X-ray absorption spectroscopy (XAS) is a widely used technique within biochemistry to analyze the structure around metal ions in proteins. A spectrum consists of two parts; the X-ray Absorption Near Edge Structure (XANES) and the Extended X-ray Absorption Fine Structure (EXAFS), which both give information about the local structure around a specific element (e.g. copper), but are analyzed in different ways. The use of XAS in biochemistry is complicated by radiation damage, e.g. reduction of Cu(II) to Cu(I).

In this thesis, the preliminary work on a microfluidics flow cell for the new XAS beamline, Balder, at the MAX IV Laboratory synchrotron in Lund, Sweden is presented, and the flow capabilities are proven sufficient to avoid radiation damage with the flux expected for the beamline.

To explore the advantages of XAS in the analysis of metalloproteins, data was collected on *Anabaena Variabilis* plastocyanin, a protein well described in literature using X-ray diffraction giving ultrahigh resolution crystal structures. The XAS data showed clear indication of photoreduction, and the fitted models bare close resemblance to the crystal structures, thus indicating that the crystal structures published are also a result of radiation damage. The data is compared to previously collected data with little to no photoreduction, and a difference in histidine distances are found, although the data quality is lower for this dataset. In an attempt to improve the fitting procedure, a Design of Experiment was utilized to vary the fitted parameters in a statistical feasible way. While promising initial results showed good fits to the data, the time limit of this thesis did not allow for a better fit than achieved by conventional methods to be found.

XAS was also deployed to analyze the binding of Cu(II) and Zn(II) to the amyloid- β peptide (A β), related to Alzheimer's Disease, and two variants of it with a mutation on the second position. For Cu(II)A β , the fibrillar coordination was found to depend on pH and the variant, with several models giving reasonable fits, possibly as a result of a mixture of several coordinations in the solution. For Zn(II)A β , the coordination was found to be the same across pH and variant, and was best fitted with a tetrahedral model of two histidines, a carboxylic group of either a glutamate or aspartate, and another oxygen or nitrogen ligand.

Resumé

Røntgenabsorptionsspektroskopi (XAS) er en udbredt metode inden for biokemi til at analysere strukturen omkring metalioner i proteiner. Et spektrum består af to dele; X-ray Absorption Near Edge Structure (XANES) og Extended X-ray Absorption Fine Structure (EXAFS), der begge bidrager med information om den lokale struktur omkring et specifikt grundstof (f.eks. kobber), men analyseres på forskellig vis. Brugen af XAS i biokemi kompliceres af stråleskade, f.eks. reduktion af Cu(II) til Cu(I).

I denne afhandling præsenteres det indledende arbejde på en mikrofluidcelle til den nye XAS beamline, Balder, ved MAX IV synkrotronen i Lund, Sverige, og flydeegenskaberne bevises tilstrækkelige til at undgå stråleskade ved den flux der forventes på beamlinen.

For at udforske fordelene ved XAS i undersøgelser af metalloproteiner, blev der samlet data på *Anabaena Variabilis* plastocyanin – et protein der er velbeskrevet i litteraturen med krystalstrukturer af ultrahøj opløsning løst fra røntgendiffraktionseksperimenter. XAS dataen viste en klar indikation af fotoreduktion, og de forfinede modeller lignede meget de publicerede krystalstrukturer, hvilket gav indikationer om at disse strukturer også er påvirkede af fotoreduktion. Dataen bliver også sammenlignet med tidligere data med lidt eller ingen fotoreduktion, og en forskel i histidinafstandene kan ses, selvom datakvaliteten er lavere for dette datasæt. I et forsøg på at forbedre forfiningsproceduren udnyttes et Eksperimentdesign til at variere de forfinede parametre på en statistisk fordelagtig måde. Selvom de indledende resultater var lovende og viste en god sammenhæng med dataen, tidsbegrænsningen på arbejdet umuliggjorde at finde en sammenhæng bedre end den der var fundet med konventionelle metoder.

XAS blev også anvendt til at analysere bindingen af Cu(II) og Zn(II) i amyloid- β peptidet ($A\beta$), relateret til Alzheimers, og to varianter af det med en mutation på anden position. For Cu(II) $A\beta$ blev koordinationen i fibriller bestemt til at være afhængig af pH og varianten, med flere modeller der viste gode sammenhænge med data, muligvis som et resultat af en blanding af flere koordinationer i opløsningen. For Zn(II) $A\beta$ blev en tetraedermodel bestående af to histidiner, en karboxylgruppe fra enten glutamat eller aspartat, og endnu en oxygen eller nitrogen ligand fundet til at passe bedst med data, på tværs af variant og pH.

List of Abbreviations

AD	-	Alzheimer's Disease
A β	-	Amyloid- β
<i>A.v.</i>	-	<i>Anabaena Variabilis</i>
APP	-	Amyloid Precursor Protein
BioXAS	-	Biological X-ray Absorption Spectroscopy
DFT	-	Density Function Theory
DoE	-	Design of Experiment
DTAB	-	Dodecyltrimethylammonium Bromide
cryo-EM	-	Cryogenic Electron Microscopy
EM	-	N-ethylmorpholine
EPR	-	Electron Paramagnetic Resonance
ESRF	-	European Synchrotron Radiation Facility, in Grenoble, France
EXAFS	-	Extended X-ray Absorption Fine Structure
FEP	-	Fluorinated Ethylene Propylene
FT	-	Fourier Transform
HEPES	-	4-(2-hydroxyethyl)-1-piperazineethanesulfonic acid
HFIP	-	Hexafluoroisopropanol / Hexafluoro-2-propanol
HPLC	-	High-Performance Liquid Chromatography
HSA	-	Human Serum Albumin
MAX II	-	MAX II Synchrotron, MAX-lab, National electron accelerator laboratory for synchrotron radiation research, nuclear physics and accelerator physics (Lund University, Sweden)
MAX IV	-	MAX IV Laboratory, Synchrotron Facility in Lund, Sweden
MES	-	2-(N-morpholino)ethanesulfonic acid
MOPS	-	3-(N-morpholino)propanesulfonic acid
NaPi	-	Sodium Phosphate
NIST	-	National Institute of Standards and Technology

NMR	-	Nuclear Magnetic Resonance
PBS	-	Phosphate-buffered Saline
PC	-	Plastocyanin
PC(I)	-	Plastocyanin with Cu(I)
PC(II)	-	Plastocyanin with Cu(II)
PC(II) _c	-	Crystalline Plastocyanin with Cu(II)
PC(II) _s	-	Plastocyanin with Cu(II) in solution
PDB	-	Protein Data Bank
RMSD	-	Root Mean Square Deviation
SDS	-	Sodium Dodecyl Sulfate
SOLEIL	-	Synchrotron SOLEIL, in Saint-Aubin, France
SSRL	-	Stanford Synchrotron Radiation Laboratory in California, USA
ThT	-	Thioflavin T
Tris	-	Tris(hydroxymethyl)aminomethane
UV	-	Ultraviolet
XANES	-	X-ray Absorption Near Edge Structure
XAS	-	X-ray Absorption Spectroscopy
XRD	-	X-ray Diffraction

Standard 3-letter abbreviations for the 20 natural amino acids are used throughout the thesis.

Amyloid- β samples are denoted (M-var)_{pH}, where M is the metal, var is the variant of amyloid- β , either WT (wild-type), A2T or A2V, and pH is the pH of the buffer solution containing the sample.

Contents

1	Introduction.....	5
1.1	Motivation	5
1.2	Overview of Thesis	5
2	Introduction to X-ray Absorption Spectroscopy	7
2.1	History.....	7
2.2	XAS.....	7
2.3	XANES.....	9
2.4	EXAFS	11
2.5	Experimental Setup.....	15
2.6	Data Treatment.....	16
3	Flow Cell for a Bio-XAS Beamline	19
3.1	Motivation	19
3.2	Preliminary calculations.....	19
3.3	Chip Design	20
3.4	Chip Fabrication	21
3.5	Flow Tests	22
3.6	Discussion and Conclusions	27
4	XAS Investigations of Plastocyanin	29
4.1	Background.....	29
4.2	Experimental.....	31
4.2.1	Protein Purification.....	31
4.2.2	Crystal Preparation for MAX II.....	32
4.2.3	Solution Preparation for ESRF	32
4.2.4	Data Collection, MAX II.....	33
4.2.5	Data Collection, ESRF	33
4.2.6	Data Treatment.....	34
4.2.7	EXAFS Refinements.....	35
4.2.8	XANES Simulations.....	35

4.3	Results.....	35
4.3.1	Experimental XANES.....	35
4.3.2	EXAFS Refinements.....	38
4.3.3	XANES Simulations.....	44
4.4	Discussion	47
4.4.1	Effect of cryoprotectants	49
4.4.2	Angles.....	49
4.4.3	XANES Fit.....	50
4.5	Conclusion.....	50
5	Using Design of Experiment to Optimize EXAFS Refinements	51
5.1	Introduction	51
5.2	Methods.....	52
5.3	Results and Discussion.....	53
6	The Coordination of Cu(II) and Zn(II) in Amyloid- β Fibrils	55
6.1	Biological Background.....	55
6.1.1	The Structure of A β	56
6.1.2	The Role of Metals	57
6.1.3	Variants	57
6.2	Coordination of Metals in A β	58
6.2.1	Coordination of Cu(II).....	60
6.2.2	Coordination of Zn(II).....	65
6.3	Experimental.....	66
6.3.1	Sample Preparation	66
6.3.2	ThT Fluorescence.....	67
6.3.3	XAS Data Collection, Zn(II)A β	67
6.3.4	XAS Data Collection, Cu(II)A β	68
6.3.5	EXAFS Refinements.....	68
6.4	Results and Discussion.....	69
6.4.1	ThT Fluorescence CuA β	69
6.4.2	ThT Fluorescence ZnA β	71
6.4.3	Copper XAS	72
6.4.4	Zinc XAS.....	80

6.5	Conclusive Remarks.....	85
7	Conclusion and Perspectives	87
7.1	Microfluidics Flow Cell for BioXAS.....	87
7.2	XAS Investigations of Metals in Biological Systems.....	87
7.3	Statistical Analysis of EXAFS Parameters	89
	Bibliography	91
Appendix A	A β ThT Fluorescence Diagrams.....	103
Appendix B	EXAFS Refinements of CuA β	107
Appendix C	EXAFS Refinements of ZnA β	117

1

Introduction

X-ray absorption spectroscopy (XAS) is a technique that, since it matured, has been widely used to gain knowledge within biochemical catalysis. XAS is an element specific method that may be used to characterize the structure around the metal center of metalloproteins, a group of proteins that is often related to important functions in biological systems. Notable examples include studies of manganese in the photosynthetic oxygen-evolving complex [1,2], iron in cytochrome C [3], the blue copper proteins [4], and the binding of zinc and copper in superoxide dismutases [5,6].

1.1 Motivation

With the opening of the new, next-generation synchrotron in Lund, MAX IV, and the XAS beamline, Balder (<https://www.maxiv.lu.se/accelerators-beamlines/beam-lines/balder/>), a substantial improvement of biological XAS (BioXAS) is expected. The quality of the results obtained by BioXAS is currently hampered by radiation damage, and sample quantities required [7], so faster measurements using small amounts of sample would greatly benefit the possible outcome of this research area. At the same time, development in computational resources available could improve the theoretical interpretation of XAS data.

1.2 Overview of Thesis

This thesis consists of an introduction to the method of XAS, found in Chapter 2, three projects in Chapter 3-6, and an overall conclusion in Chapter 7. In chronological order, the first project describes the development of a microfluidics flow cell for biological samples at the Balder beamline at MAX IV. Flow experiments were conducted to test if the equipment could achieve flow rates that would prevent radiation damage, even at room temperature. However, as the commissioning of the beamline was not completed within the limited time of the current project, it is yet to be tested in the actual beam.

The second project, described in Chapter 4, is on XAS investigations of *Anabaena Variabilis* plastocyanin, which is a well described protein in literature and thus ideal for benchmarking of the method. Data was collected on both the oxidized and reduced form of the protein, and at three pH values,

as crystal structures exists for these. Furthermore, the refinement of the models to fit this data was attempted optimized by the use of a Design of Experiment, described in Chapter 5.

Finally, an XAS investigation of wild-type and two variant 1-40 forms of amyloid- β was performed at three pH values to find, if any, differences in the coordination of copper and zinc across the variants and pH.

2

Introduction to X-ray Absorption Spectroscopy

XAS was discovered in the first half of the 20th century, but it took many years until a theory was developed to describe the phenomenon. Since then, the method has gone from a highly criticized niche, to something biochemists use routinely to study metals in biological systems [8].

This chapter gives a short introduction to the history and theory of XAS. The theory of EXAFS was inspired by the great lecture notes by Sakura Pascarelli (ESRF, Grenoble, France) [9].

2.1 History

While X-rays were discovered by Röntgen in 1895, the first X-ray absorption edge was measured by Maurice de Broglie in 1913 [10]. In the following years, the experimental method was developed and the fine structure was discovered [11]. Until 1971, the fine structure was described by the Kronig theory [12], which had a simple equation that was easily calculated with the tools available at the time. In 1971, the collaboration of Edward Stern, Dale Sayers and Farrel Lytle resulted in the first version of the *EXAFS equation* [13] used throughout this thesis. They treated the outgoing photoelectron as a spherical wave that is scattered off the neighboring atoms, and summed the individual waves into a total scattered wave.

The first XAS experiment [7] on a biological system was performed in 1975 by Shulman *et al.* [14].

2.2 XAS

XAS is a technique that exploits the fact that all elements have specific binding energies for their core electrons. By putting a sample in a monochromatic X-ray beam (X-rays of one wavelength), where the wavelength may be varied, and scanning a range of energies (wavelengths), a specific element may be probed.

When the energy of the incoming X-rays reach the binding energy of the core electrons of the specific element, e.g. the 1s electrons to measure the K-edge, an electron is excited to a higher unoccupied state. If the energy is high enough, the electron is excited to the continuum (Figure 1A), giving a photoelectron that is emitted in all directions from the atom. When the energy of the incoming X-

ray is further increased, the excess energy is converted into kinetic energy (E_{kin}) for the photoelectron (Figure 1B). A few femtoseconds after the electron is excited, the core hole is filled by another electron from the atom. For the heavy elements treated in this thesis, fluorescence radiation is emitted as a result (Figure 1C).

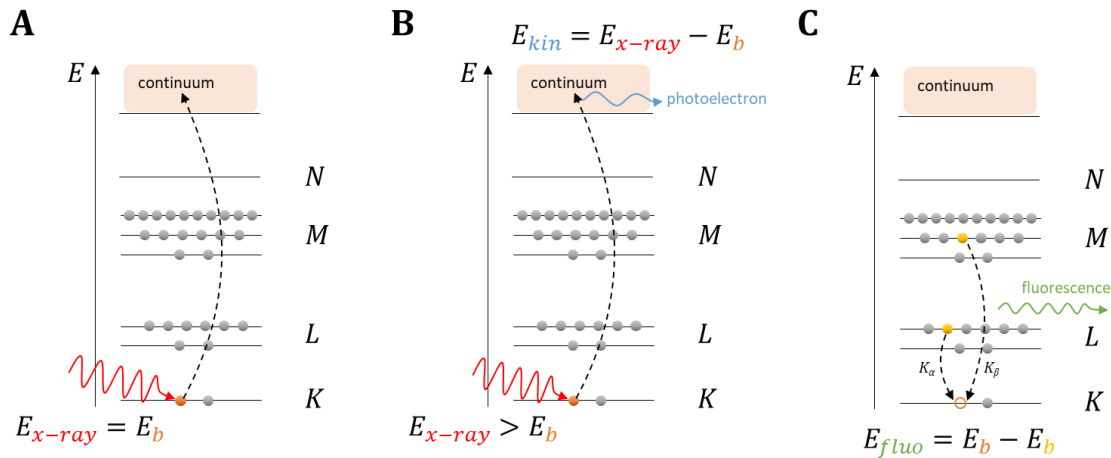


Figure 1 – The X-ray absorption event for the Cu(I) ion. A) When the energy of the incoming X-ray is equal to the binding energy of the core electron, the electron is excited to the continuum. B) When the energy is increased, the excess energy is converted into kinetic energy of the photoelectron leaving the atom. C) Finally, radiative de-excitation occurs, in which an electron from either the L-shell or the M-shell fills the core hole, thereby emitting a fluorescent X-ray.

In a standard transmission XAS experiment, the intensity of the X-ray beam is measured before and after the sample, as seen in Figure 2, enabling the calculation of the linear absorption coefficient, μ .

$$I = I_0 \cdot e^{-\mu t} \quad (1)$$

$$\mu(E) \cdot t = \ln\left(\frac{I_0}{I}\right) \quad (2)$$

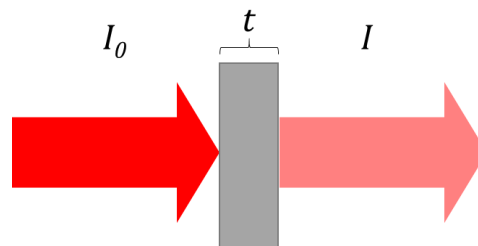


Figure 2 – Principle drawing of the quantities in an XAS transmission experiment. Red arrows are the X-ray beam, grey box is the sample of thickness t .

I_0 and I are the intensities of the beam before and after the sample, respectively, measured in photons per second, and t is the thickness of the sample. How to extract $\mu(E)$ from the intensities will be treated in section 2.6.

It may also be useful to measure the fluorescence, using a detector positioned perpendicular to the beam direction. This is done under the assumption that μ is proportional to the intensity of the fluorescence signal relative to I_0 .

$$\mu(E) \approx \frac{I_f}{I_0} \quad (3)$$

While this is not an exact measurement of μ , it is a necessity e.g. if your sample is very dilute, as the solute absorbs most of the X-rays, giving very little contrast between background and sample signal in a transmission experiment.

In the present work, all measurements are of fluorescence, because of the relative low concentrations of protein (and thereby the element in question) in the solution.

The fundamental theoretical equation used to calculate XAS is Fermi's Golden Rule

$$\mu(E) \propto \sum_{f}^{E_f > E_F} |\langle \Psi_f | \hat{\varepsilon} \cdot \mathbf{r} | \Psi_i \rangle|^2 \quad (4)$$

where ε is the photon wave vector, \mathbf{r} is the positional vector for the electron, and Ψ_i and Ψ_f are the initial and final states of the electron, respectively. The equation states that the absorption is proportional to the sum of all excitations from an initial state i to a final state f . It can be solved either by calculating the initial state and the final state accurately, which is quite difficult as the final state is an excited one, or by using multiple scattering theory, which uses a Green's function and leaves out the final state.

To understand the phenomena presented later, some quantum mechanics is needed. Here, the electrons are described by the wavefunction, $\psi(\mathbf{r}, t)$, which is the probability amplitude of finding an electron at position \mathbf{r} at time t . The integral of its square modulus must equal 1, as there is a 100% chance that the electron is somewhere at any time t

$$\int_{-\infty}^{\infty} \int_{-\infty}^{\infty} \int_{-\infty}^{\infty} \psi(\mathbf{r}, t) \psi^*(\mathbf{r}, t) dx dy dz = 1 \quad (5)$$

A full XAS spectrum is typically divided into two parts:

X-ray Absorption Near Edge Structure (**XANES**)

Extended X-ray Absorption Fine Structure (**EXAFS**)

2.3 XANES

The XANES is the part of the spectrum from 20 eV below the edge to about 30 eV above. It consists of several subparts, often divided as seen in Figure 3.

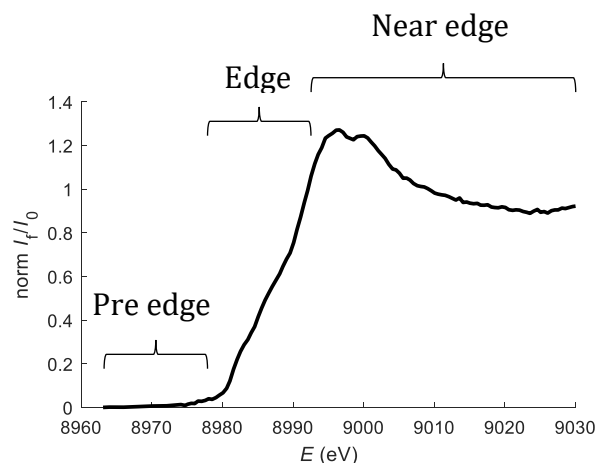


Figure 3 – Subparts of the XANES area.

The pre-edge is characterized by small features that correspond to excitations to lower states within the atom. The energy and availability of these depend primarily on the oxidation state of the metal. One example is the characteristic small peak at 8979 eV seen in Cu(II) spectra, corresponding to a $1s \rightarrow 3d$ transition, which is not possible in Cu(I) compounds as the 3d orbital is full [15].

The edge may have more intense features, corresponding to excitations of the core electron to higher unoccupied states. These are largely affected by the liganding around the metal. One good example is that of Cu(I), where the number of ligands affect the degeneracy of the unoccupied 4p-orbitals [15,16]. When Cu(I) is in a linear or slightly bended 2-coordination, the doubly degenerate $4p_{x,y}$ state (Figure 4A) will result in an intense pre-edge peak (Figure 4B). For 3- and 4-coordinated Cu(I) compounds, this peak is much less intense and shifts to higher energies, as ligands push the energy levels of $4p_y$ and $4p_x$ upwards.

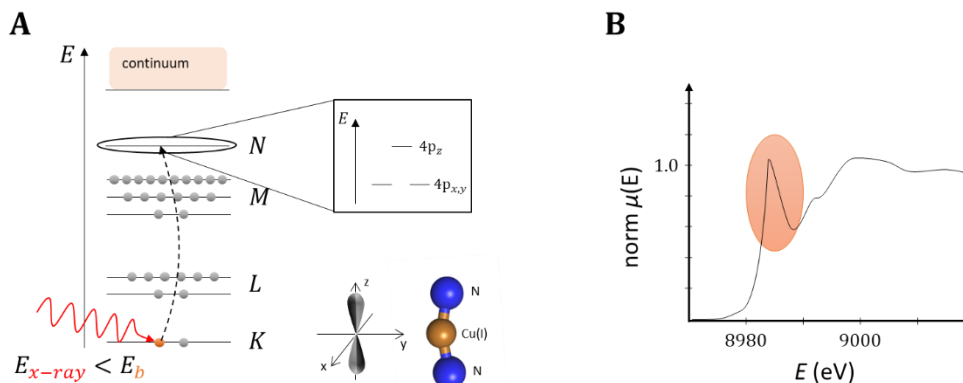


Figure 4 – A) Excitation of a core electron to an unoccupied orbital, here $4p$. The energy level of each $4p$ -orbital depends on its orientation compared to the ligands. Here, the $4p_z$ is pointing towards the two nitrogen ligands, causing it to be at a higher energy than the $4p_x$ and the $4p_y$. B) This results in an intense pre-edge peak, here seen in the experimental spectrum of $[\text{Cu}(\text{xyz})_2](\text{BF}_4)_2$ [17]. Adapted from [15].

To analyze XANES spectra in a quantitative manner, a theory that allows calculations of spectra is needed to compare with experiments. While the theory behind EXAFS is well developed, the theory of excited states, which XANES is a result of, is less matured [18]. Several XANES codes are available. The *FEFF9* code [19] is most widely used, and it employs the standard quasi-particle theory, which attempts to take the excited final states into consideration as well [18]. *FDMNES* [20] and *MXAN* [21] are examples of codes that use the standard density functional theory (DFT), which can only calculate ground states. While other codes employ the muffin-tin approximation, which assumes the potential energy between atoms to be constant, *FDMNES* utilizes the finite difference method, which circumvents this [20].

2.4 EXAFS

The EXAFS is characterized by a wavy tail at energies well above the absorption edge, often continuing more than 600 eV after the edge. Remembering equations (4) and (5), the absorption coefficient is proportional to the probability that the absorption event occurs, which in turn is proportional to the probability of finding the electron at a specific point in time and space. Thus, a wavy absorption coefficient will occur if the probability of finding the electron at the center changes as a function of the energy of the incoming X-ray.

Looking at the isolated atom, and remembering from Figure 1 that for $E > E_0$ the kinetic energy for the photoelectron is $E_{\text{kin}} = E - E_0$, the photoelectron will be further and further away from the center with increasing energy, and thus, the probability of absorption will decrease gradually, as seen to the left in Figure 5. In a nonisolated system as seen to the right, the photoelectron will backscatter off the neighboring atoms in a fully elastic process, i.e. the wavelength of the backscattered wave is the same as that of the photoelectron ($E_{\text{kin}} = E_{\text{backscatter}}$). The amplitude of the backscattered wave, however, will

depend on the type of atom and its spatial distribution (the Debye-Waller factor).

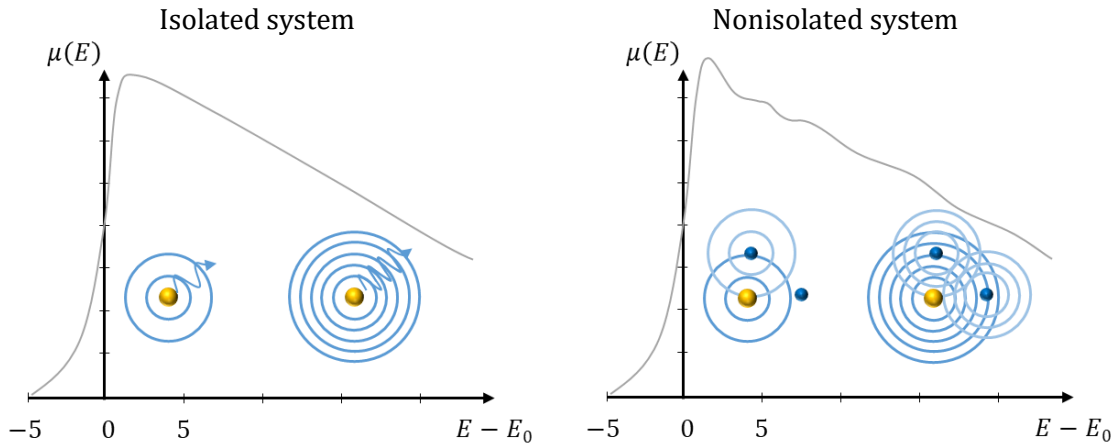


Figure 5 – Absorption coefficient as a function of energy in an isolated and a nonisolated system, respectively. In each plot, there are two models of a heavy atom that has absorbed an X-ray of low and high energy, E , respectively, which gives rise to a photoelectron of energy $E - E_0$. In the nonisolated system, the backscattered waves will have identical energies, but different amplitudes.

As the distances to the atoms are kept constant while the energy, and thus the wavelength, of the outgoing photoelectron changes, the interference pattern experienced at the center will change. This is what gives rise to the EXAFS signal. At higher energies, the backscattered waves may even scatter off other atoms as well, before affecting the absorption probability back at the center. This process is called multiple scattering.

The EXAFS is limited by the core-hole lifetime, i.e. the few femtoseconds before an electron from a higher level of the atom occupies the core hole. This results in a limit as to how far from the central atom there will be information available, as the backscattered wave must be able to return to the central atom before the core-hole is closed, to be able to affect the absorption probability.

To extract the EXAFS signal from the absorption coefficient, the oscillations needs to be isolated. First, the background function, $\mu_0(E)$, is subtracted from the normalized spectrum (Figure 6A, result in Figure 6B), and secondly, the X-variable is changed from the energy of the incoming X-ray to be the wavenumber of the photoelectron, k (Figure 6C).

$$\chi(E) = \mu(E) - \mu_0(E) \quad (6)$$

$$k = \sqrt{\frac{2m_e(E - E_0)}{\hbar^2}} \quad (7)$$

where m_e is the mass of the electron, E_0 is the energy of the edge, and \hbar is Planck's constant.

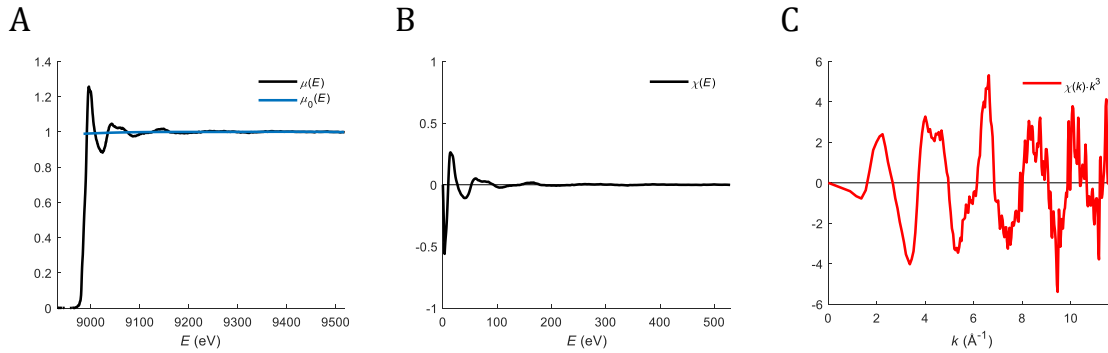


Figure 6 – Extraction of the EXAFS signal from the normalized data. A) The normalized data (black) with a spline function (blue) simulating the background signal. B) The EXAFS signal as a function of E . C) The k^3 -weighted EXAFS signal as a function of the wavenumber, k .

The EXAFS signal will depend on all paths to neighboring atoms, and each path may be approximated as a damped sine wave with amplitude A , and phase ψ . The sum of all paths will give the EXAFS signal.

$$\chi(k) = \sum_j A_j(k) \cdot \sin(\psi_j) \quad (8)$$

For symmetric compounds, it may be useful to group identical atoms (relative to the absorbing atom) in shells.

When calculating theoretical EXAFS spectra, the EXAFS equation is used [13]

$$\chi(k) = \sum_j N_j S_0^2 f_j(k) \cdot e^{-\frac{2R_j}{\lambda(k)}} \cdot \frac{e^{-2k^2\sigma_j^2}}{kR_j^2} \cdot \sin(2kR_j + \Phi_j(k)) \quad (9)$$

where

N_j is the number of atoms in the j 'th shell. It may be refined, but throughout the work in this thesis, it is kept constant at 1 to lower the number of parameters. Instead, initial models may contain different numbers of atoms.

R_j is the distance between the absorbing atom and the backscattering atom(s) in the j 'th shell. In a multiple scattering event, R_j is half the total path length. As the distance to each atom in the model is refined, this parameter changes accordingly.

σ_j^2 is the mean squared displacement of the atom(s) in the j 'th shell, also known as the Debye-Waller factor. It accounts for thermal vibrations, and general disorder in the positions of the atoms. This parameter is refined, and a large value may indicate an error in the model, or a mixture of several species in the sample.

S_0^2 is the electron reduction factor. It stems from the interaction between the photoelectron and electrons in the outer shells of the absorbing

atom. At high kinetic energies of the photoelectron, the outer shell electrons may be excited, slightly reducing the energy of the photoelectron, compared to the expected $(E - E_0)$. This causes a phase shift and thus destructive interference affecting the total EXAFS amplitude. Experiments find that typical values are $S_0^2 \approx 0.85 - 1.1$ [22], but measurements on known model compound should be performed along the samples in question to give a good estimate of its value.

$f(k)$ is the backscattering amplitude. It depends on the nature of the backscattering atom; light atoms will have high amplitudes at low values of k , whereas heavy atoms will have higher amplitudes at high values of k .

$\lambda(k)$ is the mean free path of the photoelectron. It is the limiting factor in how far away from the absorbing atom information can be found. The mean free path depends partly on the core hole lifetime and partly on the kinetic energy of the photoelectron (and thus, k).

$2kR_j + \Phi_j(k)$ is the phase, of which $2kR_j$ is directly related to the distance to the backscattering atom and the phase of the outgoing photoelectron, and $\Phi_j(k)$ is the phase shift caused by interaction between the photoelectron and the Coulomb potential between the absorbing and the backscattering atom.

The moment that led to the breakthrough in discovering the quantitative use of EXAFS was when a Fourier Transform (FT) was applied to the signal [23]. The FT of the data presented in Figure 6C can be seen in Figure 7. The graph is similar to a radial distribution function, but is different due to the phase shift, which have to be corrected for to have the peaks at the distances corresponding to the positions of the neighboring shells.

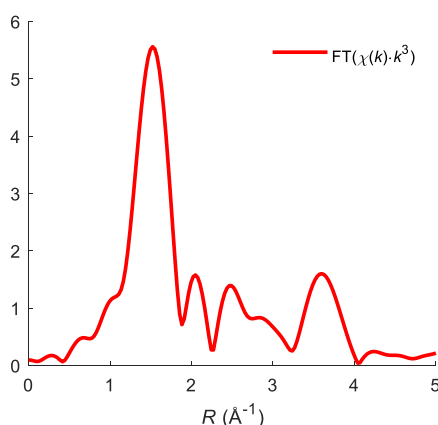


Figure 7 – An example of a Fourier Transform (FT) of the k^3 -weighted $\chi(k)$ function

2.5 Experimental Setup

XAS is most commonly performed at synchrotrons, although experiments have been performed on laboratory scale [24]. At the synchrotron, electrons are accelerated up to near the speed of light, and stored inside a ring. Every time the path of an electron is changed to keep it inside the ring, X-rays are generated and sent to a beamline. A schematic presentation of the beamline Balder at MAX IV can be seen in Figure 8. To create high intensity X-rays, a magnetic device called a wiggler is inserted in the ring. The wiggler consists of several magnets with alternating dipoles, such that the X-rays generated each time the electrons wiggle create positive interference, giving an X-ray beam with very high intensity over a broad range of wavelengths. Some of the optical equipment used to tune the beam is also shown in Figure 8. Slits are used to cut the beam. The collimating mirror is used to make all photons parallel. The monochromator consists of two silicon crystals, the first one of which, when hit by a beam of multiple wavelengths, only diffracts a beam of one wavelength. The second crystal diffracts the beam to make it parallel to the incoming beam. The crystals may be rotated to select which wavelength is allowed to pass through, which is crucial in XAS experiments. The smallest angle the monochromator is able to turn defines the energy resolution of the experiment. A focusing mirror is positioned towards the sample, to focus the beam so that the focal point is on the sample.

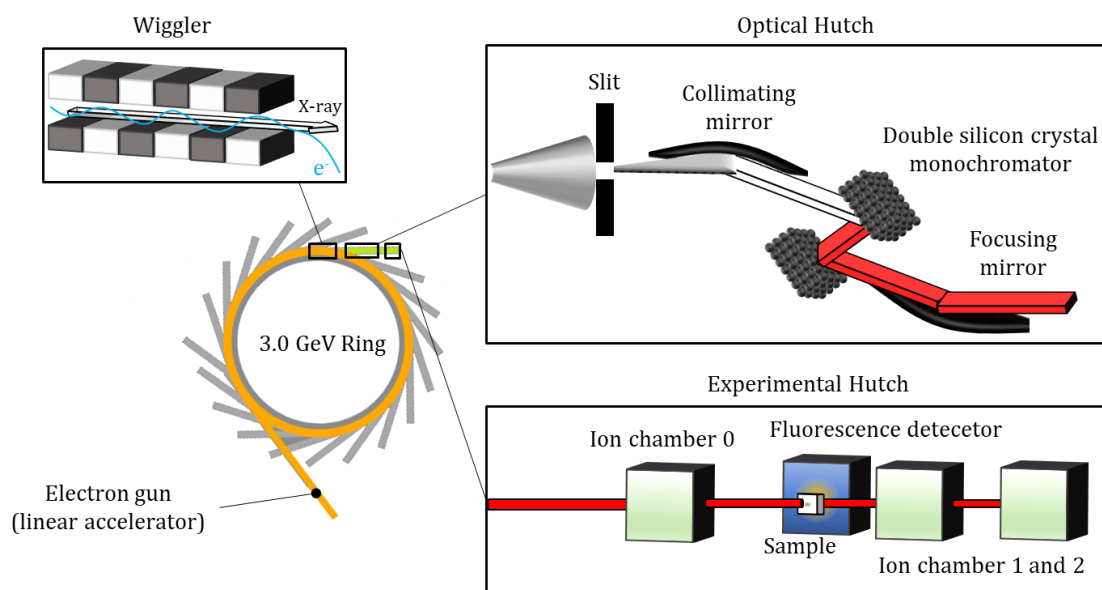


Figure 8 – Schematic presentation of an XAS beamline, with basis in the Balder beamline at MAX IV. Electrons are accelerated up to near the speed of light in the linear accelerator, and shot into the ring, where the electrons are directed using magnets. Wigglers make the electrons wiggle, and create highly intense X-rays that are sent to the beamlines. The beamline consist of an optical and an experimental hutch. In the optical hutch, slits and mirrors tune the dimensions and direction of the beam, while a monochromator only allow X-rays of a certain wavelength to pass through. In the experimental hutch, ion chambers count photons, and if a fluorescence experiment is conducted, the sample is turned 45° to the beam direction to give a signal on the fluorescence detector. After the sample, two ion chambers with a reference foil of the element scanned in between them are placed.

In the experimental hutch of the beamline, several ion chambers count photons passing through. A typical setup includes one ion chamber before, and two after the sample, with a reference foil in between them. If a fluorescence experiment is being conducted, the sample is turned 45° to the beam direction, to send the fluorescence signal to the detector that is positioned perpendicular to the beam direction.

To protect the sample from radiation damage, it may be placed in a cryostat with windows of low absorbing material, or continuously replaced in a flow cell.

2.6 Data Treatment

Several steps are performed to normalize XAS data to enable spectra comparison across sample conditions, and to extract the EXAFS signal.

Baseline correction sets the signal before the edge to 0 by subtracting a linear function fitted to a user defined range (Figure 9A). This step is straightforward for all data treated in this dissertation, but may be complicated by noise or intense pre-edge signals.

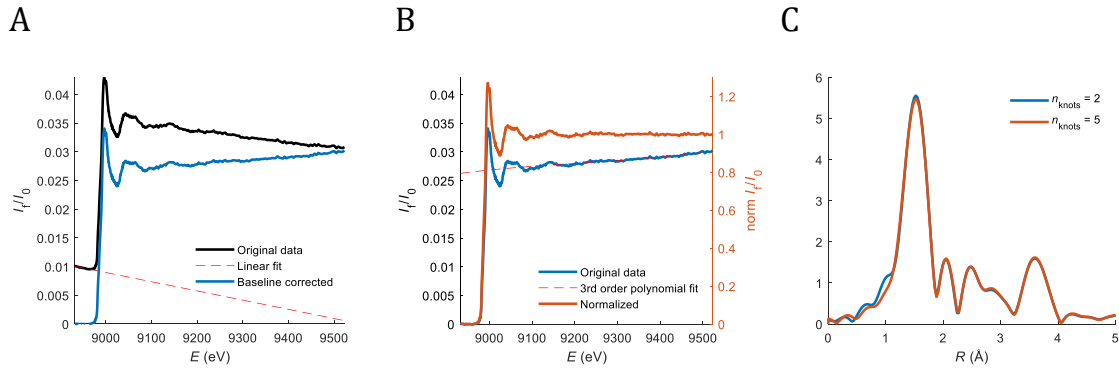


Figure 9 – Examples of the steps in extraction of the $\chi(k)$ signal. A) Baseline correction B) Edge step normalization C) Effect of the number of knots for the spline used for extraction of the $\chi(k)$ signal.

Normalization is the division by a polynomial fit to the EXAFS range (Figure 9B). It is done to eliminate differences in spectra due to anything irrelevant to the experiment, i.e. sample thickness, concentration, detector position, etc. The polynomial order and the fit range is somewhat a matter of individual preference. In the current work, only third order polynomials have been used, while the range has been optimized for each experiment to give as flat data as possible.

Finally, as also described in section 2.4, for the extraction of the $\chi(k)$ signal, an E_0 is set, and a spline function is fitted to the data to resemble the background signal, i.e. the isolated atom. While the E_0 for some data treatments was set to the tabulated K -edge energy, for others, it was changed after an initial refinement of the first shell of atoms. This was done, as studies have shown a large E_f may result in erroneous parameters [25]. The effect of the number of knots for the spline function was observed in the FT, as can be seen in Figure 9C. The value was chosen to give as low and smooth a signal as possible before the main peak, without affecting the rest of the features.

The number of independent parameters, N_{ind} , is defined as [26]

$$N_{ind} = \frac{2 \cdot \Delta k \cdot \Delta r}{\pi} + 2 \quad (10)$$

To avoid overfitting the data by inclusion of too many parameters, the number of parameters should be well below the N_{ind} .

Fits to EXAFS data were evaluated using R_{EXAFS} [27]

$$R_{EXAFS} = \sum_i^N \frac{1}{\sigma_i} (|\chi_{exp}(k_i) - \chi_{theo}(k_i)|) \cdot 100\% \quad (11)$$

Quality of XANES fits was calculated using an R-factor defined as the Root Mean Square Deviation (RMSD)

$$R_{\text{XANES}} = \sqrt{\frac{1}{N} \sum_i^N (\mu_{\text{exp}}(E_i) - \mu_{\text{cal}}(E_i))^2} \quad (12)$$

3

Flow Cell for a Bio-XAS Beamline

The following chapter describes the work that was carried out during my first year as a PhD student. The work was mainly carried out at the MAX IV Laboratory in Lund, Sweden, in close collaboration with Dr. Kajsa Sigfridsson Clauss.

3.1 Motivation

With the opening of MAX IV in May 2016, the new XAS beamline (Balder) was being established with the aim of providing a better beamline to biological and catalysis users. The plan for the biological users was to provide a beamline that could do fast data collection, but also allow studies at room temperature. To avoid radiation damage, the idea was to use a microfluidics device to flow the sample fast enough through the beam, that the sample was replaced with new sample before radiation damage could be detected – similar to the *diffract before destroy* approach [28]. Several studies have shown microfluidics to be a feasible way to handle samples at synchrotron light sources [29–31].

3.2 Preliminary calculations

In order to calculate the dimensions of the flow cell, certain considerations were required. The amount of sample in the beam to get a reasonable signal, consuming as little sample as possible, and avoiding radiation damage.

To calculate the dose absorbed by a protein solution, the equation from [32] is used

$$\text{Absorbed Energy} = E_{\text{incident}} \left(1 - e^{-\left(\frac{\mu}{\rho}\right) \cdot x} \right) \quad (13)$$

Where $\frac{\mu}{\rho}$ is the mass attenuation coefficient and $x = t \cdot \rho$, of which t is the sample thickness and ρ is the density. It may be calculated for a mixture using

$$\frac{\mu}{\rho} = \sum_i w_i \left(\frac{\mu}{\rho}\right)_i \quad (14)$$

Where w_i and $\left(\frac{\mu}{\rho}\right)_i$ are the weight fraction and the mass attenuation coefficient, respectively, for element i . E_{incident} is the photon flux times the energy of the

beam, and given in units of J/s. Using a flux of 10^{13} photons per second and an X-ray energy of 9300 eV, the incident energy flux is found to be

$$E_{\text{incident}} = 10^{13} \text{ photons} \cdot \text{s}^{-1} \cdot 9300 \text{ eV} = 0.0149 \text{ J} \cdot \text{s}^{-1}$$

Using a 1 mM *Anabaena Variabilis* plastocyanin solution as a test protein, the mass attenuation coefficient, $\left(\frac{\mu}{\rho}\right)_{\text{PC}}$, was calculated with the contribution of each atom found in the National Institute of Standards and Technology (NIST) tables, see Table 1 [33].

Table 1 - Mass attenuation coefficients for various elements included in preliminary calculations.

Element	μ/ρ (cm²/g)
C	4.576
H	0.3914
N	7.562
O	11.63
S	94.65
Cu	52.55

The $\left(\frac{\mu}{\rho}\right)_{\text{PC}}$ was calculated to be 10.35 cm²/g, mostly due to the high content of water. Using equation (13) and the values found, the absorbed dose of a 1 mM plastocyanin solution becomes

$$\begin{aligned} \text{Absorbed energy} &= 1.49 \cdot 10^{-2} \frac{\text{J}}{\text{s}} \cdot \left(1 - e^{-10.35 \frac{\text{cm}^2}{\text{g}} \cdot 1.01 \frac{\text{g}}{\text{cm}^3} \cdot 0.04 \text{ cm}}\right) \\ &= 9.66 \cdot 10^{-3} \frac{\text{J}}{\text{s}} \end{aligned}$$

To get the dose in Grays (J/kg) per second from the absorbed energy, we divide by the mass of the medium absorbing the beam. Considering a beam size of 200 μm \cdot 200 μm , a thickness or height of the sample of 400 μm , and a density of 1.01 g/cm³, the total mass hit by the beam is $1.6 \cdot 10^{-8}$ kg, giving

$$\text{Dose per time} = 315.0 \text{ kGy/s}$$

As SAXS studies have shown changes in signal as a function of dose at 2.37-51.24 kGy [34] or a critical dose as low as 0.6 kGy [35], the time scale of radiation damage in the current example is expected to be in the millisecond range. Thus, following the idea of replacing the sample before it is destroyed, the molecules should move with a velocity of 100 $\mu\text{m}/\text{ms}$.

3.3 Chip Design

The design of the chip had very few requirements, as no mixing of species was part of the initial idea. The chip should consist of a relatively narrow channel of

minimum 200 μm (to fit with the proposed beam size), and a depth or height of about 1000 μm to have enough signal for fluorescence experiments. At the same time, a system should be developed to consume as little sample as possible.

The chip material should be as transparent to X-rays as possible. While the body of the chip is somewhat irrelevant, a window where the measurement takes place is often used. Examples of window materials include borosilicate [30], SiN [31], and Topas [36].

In a collaboration with Aghiad Ghazal (previously University of Copenhagen, now Novo Nordisk), a homemade chip made of three layers of pure Kapton foil of different thicknesses was decided as a point to explore. The chip should be a 500 μm thick layer of Kapton foil, with fluorinated ethylene propylene (FEP) on both sides to work as glue, and two 12 μm thick layers on each side. A 100 μm wide channel should then be cut into the middle layer. The schematic may be seen in Figure 10. Based on previous work by Aghiad Ghazal *et al.* [37], the chip should then be mounted into a chip holder with an interface for microfluidics connections.

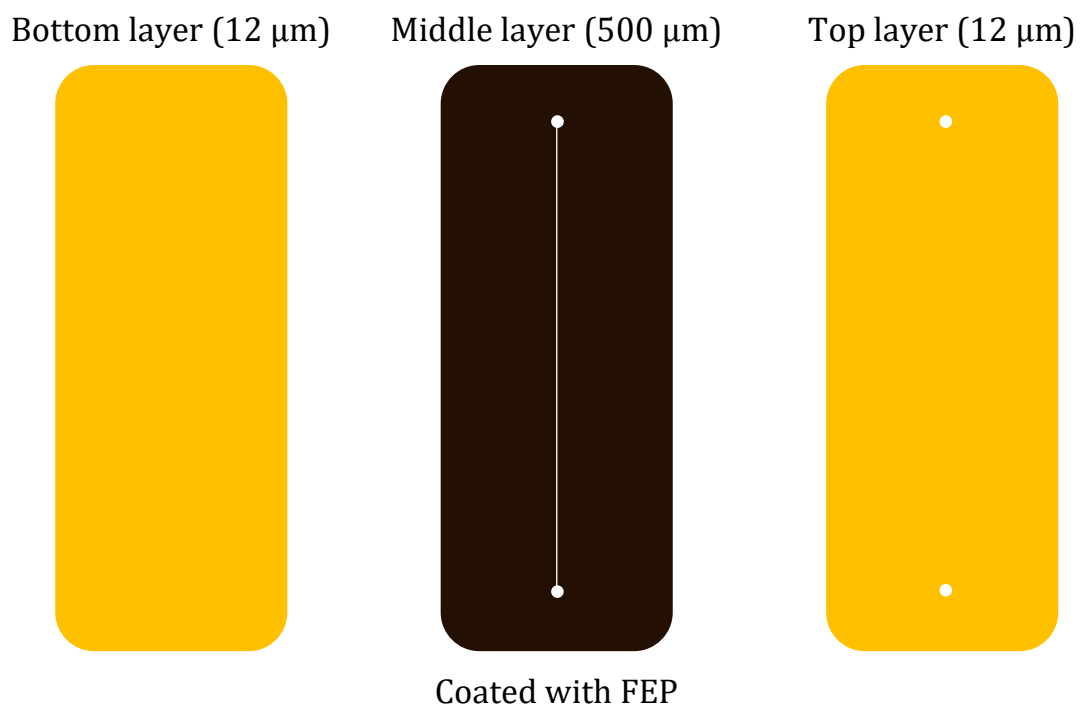


Figure 10 – Schematic design of layers of Kapton, constituting the flow cell. Middle layer is coated with FEP.

3.4 Chip Fabrication

The 100 μm wide and 500 μm deep channel was cut into the middle layer, using a *microSTRUCT vario* UV laser from *3D-Micromac*. As the beam is shaped as a cone, one layer of 100 μm was drilled at a time to make the walls of the channel

as straight as possible. Nonetheless, a difference in width could be seen between the top and the bottom, as presented in Figure 11.

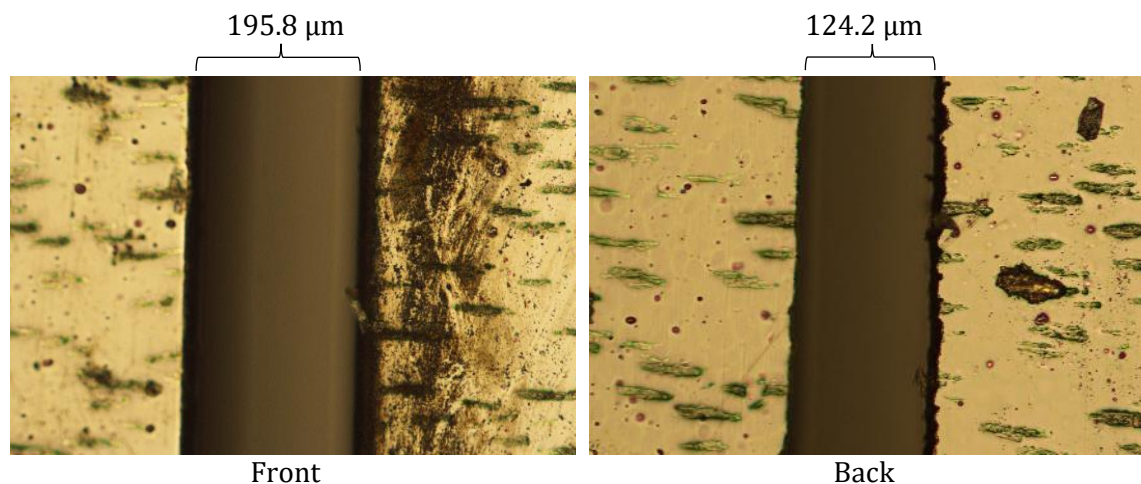


Figure 11 – Microscope pictures of the lasercut middle layer for the flow cell.

A heating press was used to glue the three layers together. However, air bubbles could not be avoided, as seen with the test shown in Figure 12.



Figure 12 – Air bubbles between the thin top layer and the thick middle layer of Kapton foil after using a heating press to glue the layers together.

Due to the non-uniform nature of the channel, and the challenges with gluing the layers together, the pure Kapton chip was cancelled.

3.5 Flow Tests

A simple cross-shaped channel chip was purchased from *Microfluidics Chipshop*. The chip measures 1.65 cm × 9.55 cm with three Luer inlets and one Luer outlet, having a 200 μm × 200 μm × 87.0 mm mixing channel, see Figure 13. These dimensions compares with that of a previous study also doing XAS [38].

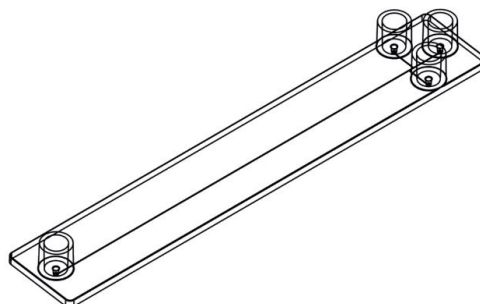


Figure 13 – Schematic design of cross-shaped straight channel chip purchased from Microfluidics Chipshop.

To be able to control pressure and flow, an *OB1 MK3* microfluidic flow control system was purchased from *Elveflow*. It is equipped with three pressure outlets in the 0-200 mbar range and one in the 0-2000 mbar range. Furthermore, flow sensors for all channels measuring flows between 0 and ± 1 mL/min were also acquired from *Elveflow*.

A series of flow measurements to establish the correlation between viscosity and flow rate were conducted. For these tests, the setup outlined in the top of Figure 14 was used, and the cross channel chip was utilized using one inlet, while the other two were sealed with film and male Luer fittings as seen in the bottom of Figure 14. The experiments were accomplished by first filling an 1.5 ml tube with the sample and mounting all fittings. A pressure of 50 mbar was put on, and the system was allowed to replace the previous sample until any air bubbles between each sample were through, or until 0.5 ml of sample was drained. Flow rates were measured for 20 seconds at 50, 75, 100, 150, and 200 mbar.

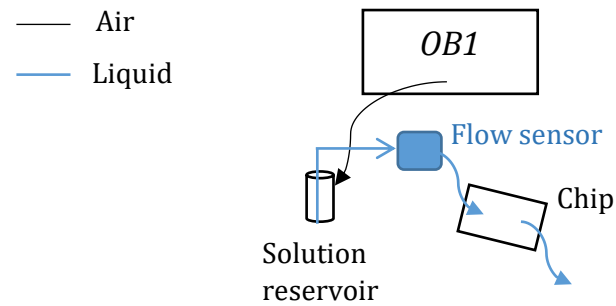


Figure 14 – Top: Schematic drawing of setup. Bottom: Photo of the Luer fittings on the cross-channel chip, inlet furthest away, outlet closest. Two inlets are blocked with parafilm kept in place by Luer fittings.

The data was analyzed by averaging the flow rate observed from 2.5 seconds after the pressure was set until the pressure was changed. The results are tabulated in table 2, and the correlation between pressure and flow at different glycerol levels are visualized in Figure 15.

Table 2 – Results from viscosity experiments. Flow data is presented with one standard deviation.

Glycerol (v/v %)	p (mbar)	Flow ($\mu\text{l}/\text{min}$)	Glycerol (v/v %)	p (mbar)	Flow ($\mu\text{l}/\text{min}$)
0%	50	203 \pm 1	15%	50	125 \pm 1
0%	75	281 \pm 1	15%	75	174.6 \pm 0.8
0%	100	367 \pm 1	15%	100	221 \pm 1
0%	150	531 \pm 2	15%	150	324 \pm 1
0%	200	672 \pm 3	15%	200	425 \pm 1
1%	50	181 \pm 1	20%	50	95.3 \pm 0.8
1%	75	254 \pm 2	20%	75	140.5 \pm 0.7
1%	100	337 \pm 2	20%	100	182 \pm 1
1%	150	495 \pm 2	20%	150	261 \pm 1
1%	200	631 \pm 2	20%	200	342 \pm 2
2%	50	173 \pm 2	30%	50	69.5 \pm 0.6
2%	75	248 \pm 2	30%	75	102.8 \pm 0.6
2%	100	329 \pm 2	30%	100	133.5 \pm 0.6
2%	150	488 \pm 2	30%	150	187.2 \pm 0.6
2%	200	621 \pm 3	30%	200	236 \pm 1
5%	50	164 \pm 1	40%	50	44.4 \pm 0.4
5%	75	231 \pm 1	40%	75	61.7 \pm 0.5
5%	100	300 \pm 1	40%	100	81.8 \pm 0.7
5%	150	443 \pm 1	40%	150	122.9 \pm 0.5
5%	200	568 \pm 2	40%	200	154.7 \pm 0.9
10%	50	144 \pm 1	50%	50	27.9 \pm 0.5
10%	75	200 \pm 1	50%	75	38.3 \pm 0.3
10%	100	256 \pm 1	50%	100	49.0 \pm 0.4
10%	150	382 \pm 1	50%	150	70.8 \pm 0.5
10%	200	494 \pm 1	50%	200	94.4 \pm 0.5

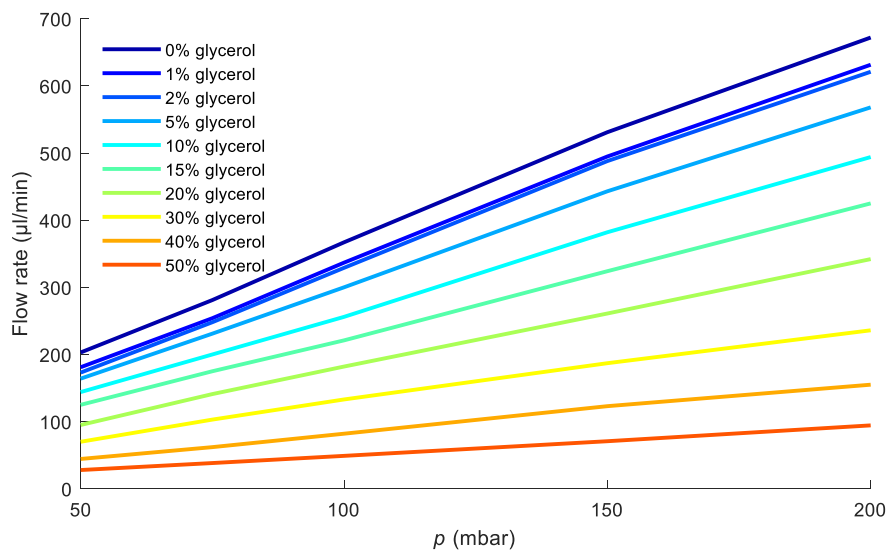


Figure 15 – Flow rate as a function of pressure applied to reservoir of solutions with various glycerol contents.

Another experiment using protein in solution was conducted. For this purpose, a 100 mg/ml Human Serum Albumin (HSA) solution in 8 mM octanoate was measured the same way as the glycerol solutions, although only about 15 seconds was allowed at each pressure before next pressure was set to save protein solution. The results are tabulated in Table 3 and the correlation between flow and pressure at different protein concentrations are plotted in Figure 16.

Table 3 – Results from protein experiments. Flow data is presented with one standard deviation.

Protein (mg/ml)	p (mbar)	Flow ($\mu\text{l}/\text{min}$)	Protein (mg/ml)	p (mbar)	Flow ($\mu\text{l}/\text{min}$)
0	50	204 \pm 1	10	50	191 \pm 3
0	75	282 \pm 2	10	75	264 \pm 3
0	100	370 \pm 2	10	100	351 \pm 4
0	150	531 \pm 2	10	150	514 \pm 4
0	200	679 \pm 2	10	200	654 \pm 7
1	50	198 \pm 2	20	50	193 \pm 2
1	75	275 \pm 3	20	75	262 \pm 3
1	100	358 \pm 4	20	100	341 \pm 4
1	150	524 \pm 3	20	150	496 \pm 5
1	200	668 \pm 7	20	200	610 \pm 18
5	50	192 \pm 2	50	50	172 \pm 2
5	75	266 \pm 3	50	75	232 \pm 2
5	100	348 \pm 3	50	100	269 \pm 5
5	150	504 \pm 4	50	150	439 \pm 4
5	200	637 \pm 7	50	200	559 \pm 4

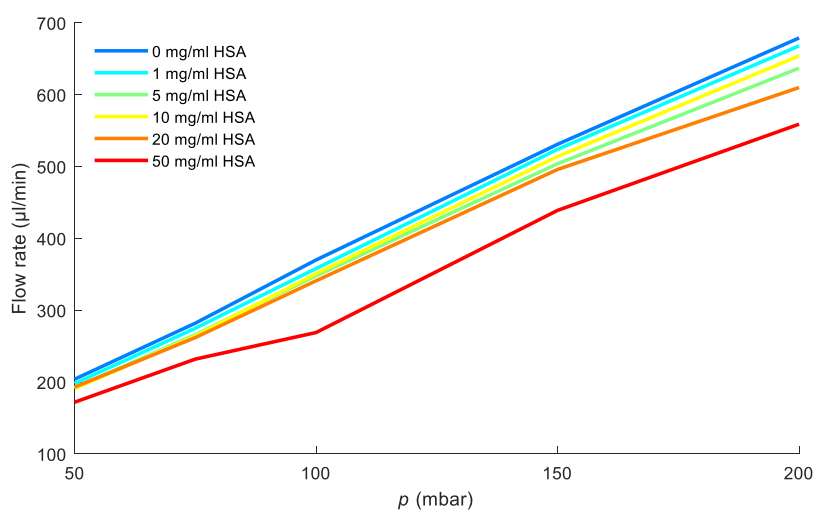


Figure 16 – Plot of flow rate ($\mu\text{l}/\text{min}$) vs pressure (mbar) at different concentrations (mg/ml) of HSA protein.

3.6 Discussion and Conclusions

A clear correlation between pressure and flow can be seen in all of the experiments with water and glycerol, which tells us that the setup is working and is reliable.

The highest flow rate with a protein solution in this setup was just below 700 $\mu\text{l}/\text{min}$. The radiation dose absorbed by a solution of 1 mM plastocyanin will require the sample to move at $\sim 100 \mu\text{m}/\text{ms}$ or at a flow rate of $\sim 250 \mu\text{l}/\text{min}$ having a channel area of $(100 \times 400) \mu\text{m}^2$. Therefore, the current setup is able to avoid radiation damage. As the required flow rate is proportional with the flux, attenuating the beam to a flux of 10^{12} photons/s will lower the required flow rate to 25 $\mu\text{l}/\text{min}$, easily achievable with any solution.

To save sample volume, it is possible to load only the volume required for a proper signal. With a flux of 10^{13} photons/s, a rough estimate for the Balder beamline would be that 10 s of measurement would be sufficient for a good signal to noise ratio, collecting full EXAFS. This would consume $\sim 4 \mu\text{l}$ of 1 mM sample. Combining this with measurements at room temperature, the setup should be considered a strong competitor to existing beamlines, as well as a great complement to X-ray diffraction experiments when analyzing the metal centers of metalloproteins.

4

XAS Investigations of Plastocyanin

This chapter describes the investigations of the Cu(II) center in plastocyanin (PC), a protein that has been well described in literature, with multiple ultra high resolution crystal structures published. Six samples of *Anabaena Variabilis* (A.v.) PC in solution with Cu(II) or Cu(I) at three different pH values were measured at the European Synchrotron Radiation Facility (ESRF), in October 2017. These data are compared to two previously collected datasets from MAXlab in October 2014 on crystalline PC and PC in solution, both with Cu(II).

Note that certain procedures used in the refinement of models for amyloid- β described in chapter 6 are not applied in the refinements presented in the current work on PC. This is simply a consequence of the work on PC being carried out much before the work on amyloid- β , which in return was carried out with more experience.

4.1 Background

PC is a small, type I blue copper protein playing an essential role in photosynthesis [39]. It is a mobile electron carrier that transports electrons from cytochrome *f*, which is a subunit of the membrane bound cytochrome *b₆f* complex, to the P700+ photoreaction center in photosystem I [40–42]. As a thorough understanding of the copper center is needed to describe the electron transport mechanism, it has been the main focus of many structural and spectroscopic studies [4,43–46].

The first structure of PC was from poplar and was published in 1983 [47]. In the oxidized state of PC (PC(II)), Cu(II) is bound strong by His37, Cys87, His87 while Met92 binds weakly at 2.8 Å to give a distorted tetrahedral coordination. In the reduced state (PC(I)), the coordination of Cu(I) is dependent on pH, as the protonation of His87 at low pH causes it to move away, leaving a distorted trigonal coordination. The small difference between the coordination of Cu(II) and Cu(I) is what gives PC its high redox potential thus enhancing its biological role [48].

Previous XAS studies of PC has demonstrated the effect of photoreduction on the copper center, showing a clear correlation between the X-ray dose and the redox state of the copper. One example is a series of measurements at room

temperature on beamline II-2 at the Stanford Synchrotron Radiation Laboratory (SSRL) in 1982 where no photoreduction was observed [49]. Later studies by the same group at wiggler beamlines VI-2 and VII-3 at SSRL showed photoreduction of PC(II) in solution even at 4 K, attributing it to the higher photon flux found at these beamlines compared to the bending magnet beamline, II-2 [50]. The study also showed that photoreduction increased if the crystal had been allowed to reach room temperatures in between measurements.

Another, more recent study investigated the change in copper coordination upon binding to physiological redox partners [51]. For reference, the study also investigated the binding in PC by itself. This data collection was carried out at the bending magnet beamline BM29 at the ESRF, at room temperature, and no photoreduction of the sample was observed. This could be explained by the fact that the beam was heavily attenuated (S. Diaz-Moreno, personal communication). The subsequent EXAFS analysis only included the first coordination sphere formed by the two nitrogen atoms of His37 and His87 along one sulfur atom of Cys84. The sulfur atom of Met92 was not included.

PC from several species have been studied over the years. In total 23 residues have been found to be identical across species, including His37, Cys87, His87 and Met92 (using poplar numeration) that constitute the coordination of the copper atom [43]. In table 4, ligand distances found in PC crystal structures with a resolution better than 1.1 Å, along with *A.v.* PC and from XAS experiments, have been listed.

Table 4 - Cu-ligand distances in Å (amino acid numbering follow poplar PC)

Organism	PDB ID	Conditions	T (K)	Res (Å)	N(His37)	N(His87)	S(Cys84)	S(Met92)
Crystal Structures								
Poplar	4DP7	Ox, pH 4 ¹	100	1.08	1.96	2.04	2.14	2.78
	4DP9	- pH 6 ¹	100	1.00	1.94	1.99	2.16	2.78
	4DPB	- pH 8 ¹	100	1.00	1.97	2.02	2.17	2.76
	4DP8	Red pH 4 ¹	100	1.05	1.88	3.24 (3.47*)	2.10	2.39
	4DPA	- pH 6 ¹	100	1.07	1.91	2.54 (3.22*)	2.15	2.62
	4DPC	- pH 8 ¹	100	1.06	1.98	2.10	2.18	2.71
<i>Anabaena Variabilis</i>	2GIM	Ox, pH 8.5 ²	100	1.6	2.07	2.13	2.10	2.77
					1.99	2.23	2.07	2.72
EXAFS								
Poplar		Ox cryst, pH 6.0 ³	298		2.01	2.01	2.09	2.75
Poplar		Ox sol, pH 6.0 ⁴	4		2.00	2.00	2.07	3.10
Poplar		Ox cryst, pH 6.0 ⁵	298		-	1.93(2)	2.13(2)	2.7(1)
-		Red, pH 4.8 ⁵	10		1.95(2)	-	2.16(1)	2.33(4)
-		Red, pH 7.2 ⁵	10		1.96(2)	2.01(4)	2.19(1)	2.9(1)
<i>Nostoc</i> sp. PCC 7119		Ox, pH 6.0 ⁶	298		1.96(2)	1.99(2)	2.12(2)	-
-		Red, pH 6.0 ⁶	298		2.08(4)	2.11(4)	2.20(3)	-

*The crystal structure contains histidine in flipped and non-flipped conformation. This distance is to the C ϵ instead of N in the flipped structure.

¹Ref [52] ²Ref [53] ³Ref [49] ⁴Ref [50] ⁵Ref [54] ⁶Ref [51]

Previous investigations of insulin have shown that the binding distances in crystal structures were different from those obtained by XAS [55]. Especially when Cu(II) was investigated, photoreduction appeared to have a major impact on the geometry around the metal ion.

With its d⁹ configuration, Cu(II) prefers a square planar or an elongated octahedral coordination [56]. However, in nature, Cu(II) is often found in tetrahedral, or slightly distorted tetrahedral, coordination, as seen in the blue copper proteins [44].

4.2 Experimental

All chemicals used were purchased from *Sigma Aldrich*.

4.2.1 Protein Purification

The purification was performed by C. Sørensen and H. E. M. Christensen.

The expression of *A.v.* PC was heterogeneously produced in *Escherichia coli* according to the previously described method [53] using a fed-batch cultivation yielding into a growth of OD₆₀₀ to 0.6. The recombinant *A.v.* plastocyanin was released from the cells by three successive freeze (-80 °C) / thaw (4 °C) cycles. The protein pellet was resuspended in 0.5 mM MgCl₂ and incubated on wet ice

for 25 min. with gentle, periodical agitation. Centrifugation was applied to the suspended protein mixture and supernatant was isolated. CuSO_4 was added to the supernatant to a final concentration of 0.5 mM and incubated on wet ice for 30 minutes. Hereafter, PC was purified initially on an *SP Fast Flow* column (Amersham Biosciences) equilibrated with 5 mM MES/NaOH pH 6.5 and washed with 5 mM MES/NaOH pH 6.5. Hereafter, the protein was eluted with 5 mM MES/NaOH pH 6.5, 60 mM NaCl. Finally, a buffer exchange was performed by ultrafiltration on an *Amicon* cell fitted with a 3 kDa *YM3* membrane.

Final purification was carried out on an *ÄKTA purifier 100* (Amersham Biosciences) HPLC system equipped with a *Source 30S* column. The cation exchange column was washed with one column volume of 5 mM MES/NaOH pH 6.5 and then one column volume of 75 mM NaCl in 5 mM MES/NaOH pH 6.5 and finally washed with of 5 mM MES/NaOH pH 6.5 again to gain stable conductivity level. Protein solution is before column loading adjusted to a conductivity of 280 $\mu\text{S}/\text{cm}$ by diluting with 5 mM MES/NaOH pH 6.5 and filtered through a 0.45 μm microfilter. Protein sample is then loaded onto the column with 5 mM MES/NaOH and eluted using a linear gradient of 0-75 mM NaCl in 5 mM MES/NaOH pH 6.5. Fractions were collected at the peak of absorbance A_{280}/A_{597} . Collected protein is ultrafiltered to a final concentration of 2 mM *A.v.* PC using a stirred *Amicon* cell with 3 kDa *YM3* membrane.

4.2.2 Crystal Preparation for MAX II

This sample preparation was done by C. Sørensen and C. G. Frankær.

Crystals of *A.v.* PC(II) were grown initially utilizing sitting-drop vapour diffusion method with 5 μl protein (11 mg/ml) + 5 μl reservoir solution (1.5 M trisodium citrate pH 8.5) against a 1 mL reservoirs, inspired by the already published crystallization conditions [53] to provide seeding crystals. Crystals were present after 5 days as large plate-shaped blue crystals.

200 μL (100 μl protein + 100 μl reservoir) drops were seeded with crystals from initial setup. Seeding was applied with crystal and mother liquor transferred by pipette. The crystallization was left for 15 days yielding multiple single crystals. The crystals were grown in a 9-well glass plate from *Hampton Research* in an encapsulated box containing the reservoir.

4.2.3 Solution Preparation for ESRF

Three 1 M (with respect to both phosphate and acetate) buffers were prepared by dissolving 15.6 g $\text{NaH}_2\text{PO}_4 \cdot 2 \text{H}_2\text{O}$ in water, adding 5.72 ml acetic acid, adjusting pH to 4, 6.5, or 8 using 10 M NaOH and finally filling to 100 ml in a volumetric flask. All solutions were filtered through 0.2 μm filter prior to storage.

Three 2.2 mM solutions of PC was prepared by replacing the purification buffer with the phosphate-acetate buffer pH 4, 6.5 or 8 through 1000x dilution on an ultracentrifugation filter. The concentration was determined by measuring the absorption at 597 nm on a *Nanodrop 2000* ($\epsilon_{597} = 4500 \text{ M}^{-1} \text{ cm}^{-1}$).

A.v. PC(I) samples were prepared by mixing 30 μl 2.2 mM PC with 6.6 μl 10 mM ascorbate, incubating at room temperature for 15 minutes. All ESRF samples were mixed with glycerol as cryoprotectant, to a final glycerol content of 20%.

4.2.4 Data Collection, MAX II

This data collection was done by C. Sørensen and C. G. Frankær.

Crystalline samples were isolated by initial centrifugation of the Eppendorf tubes containing the prepared sample solution for 3 min. at 3000 rpm and gently transferred to the sample holder [57] using a spatula. The sample holder was finally sealed with Kapton foil. 12 μl PC(II) under purification conditions was transferred to the same type of sample holder with a syringe.

The PC(II) crystalline (PC(II)_c) as well as the solution (PC(II)_s) samples were measured at I811 beamline [58] at MAX II (Lund, Sweden). The Cu K-edge was scanned using a Si(111) double-crystal monochromator detuned to 60% at 9829 eV. The beam spot was 1x1 mm and the flux was approximately 10^{11} photons/s. The sample was cooled to 22 K in a helium cryostat. The data was collected in fluorescence mode using a *PIPS PD-500* detector (*Canberra*) with 27 points in the pre edge region from 8830 eV to 8960 eV, 101 points over the edge from 8960 to 9000 eV, 50 points in the early EXAFS region from 20 to 120 eV, and finally 34 points in the EXAFS region from 120 to 800 eV. Each data point was collected in 1 second giving a total time of approximately 30 minutes for a full spectrum, corresponding to a dose of about 3 MGy. The crystalline sample was measured up to three times at three different positions. Two solution samples were measured four times, each at different spots.

4.2.5 Data Collection, ESRF

XAS data on the six samples was collected at the BM30B FAME beamline at ESRF. Approximately 20 μl of sample was injected with 26D 0.5 mm needles into sample holders with 50 μl cavities, sealed with Kapton foil. The sample holders were immediately frozen in liquid nitrogen and kept there until data collection.

The Cu *K*-edge was scanned using a nitrogen cooled Si(220) double-crystal monochromator. The beam spot on the sample was approximately $300 \times 100 \mu\text{m}^2$ with a flux of $\sim 10^{13}$ photons/s. The sample holder was kept at 20 K in a helium cryostat. Because of the low Cu(II) concentration, spectra were recorded in fluorescence mode using a 30-element solid state Ge detector

(*Canberra*). All scans were measured from 8930 eV to 9719 eV, with 23 points in the pre-edge range 8930-8974, 128 points over the edge 8979-9038, and 201 points in the EXAFS region, $k = 3.95\text{-}14.00 \text{ \AA}^{-1}$. The first 151 points were measured for 3 seconds each, while the last 201 points were measured increasingly longer, from 3 up to 10 seconds each. Each sample was measured at least 9 times at different locations, and one spectrum required approximately 40 minutes of exposure, corresponding to a dose of about 9000 MGy. Following data collection, the contribution from each pixel was gone through, discarding those pixels that had diffraction spots or other anomalies in the spectrum.

4.2.6 Data Treatment

Baseline correction, normalization, averaging and extraction of the $\chi(k)$ signal was done using *Bessy* [59]. EXAFS fitting was done using *Excurve* [60]. The crystal structure from oxidized poplar PC measured at pH 6 (PDB ID: 4DP9) was chosen as input for the data refinement of oxidized *A.v.* PC(II) at pH 4 in solution. This crystal structure has a slightly higher resolution (1.00 Å) compared to the crystal structure at pH 4 (1.08 Å), and much higher than the *A.v.* PC structure (PDB ID: 2GIM) (1.6 Å). The subsequent data treatments of all oxidized PC data sets and the data from PC(I) pH 8.0 had this EXAFS refined structure used as input for refinements. The crystal structure of reduced poplar PC at pH 4 (PDB ID: 4DP8) was used as input to the PC(I) pH 4 data.

The closest 18 atoms were included in the refinement, and, as a special feature of *Excurve*, atoms belonging to the same amino acid were grouped so that only one parameter was refined for distance. These groups were kept entirely constrained, as the number of independent points did not allow for extra parameters to be introduced with restrained refinement as described by Binsted *et al.* [27].

Initial values of Debye-Waller factors were set according to the distance from the absorber, with increasing value further away. Moreover, Debye-Waller factors were forced to be higher than 0.001 \AA^2 and lower than 0.020 \AA^2 . As previous studies found the contribution from the methionine to be low to non-existing [49], the Debye-Waller factors for all atoms in this amino acid was set to higher values (0.018 \AA^2). Only the Debye-Waller factors from the nearest neighbors and the imidazole rings of the two histidines were refined, as including the rest did not seem to improve the final result. Two angle parameters were included for each histidine, a twist and a tilt angle. The twist angle is rotation around the normal vector to the histidine plane, and the tilt angle is rotation around the cross product of the unit vector and the normal vector. The unit vector is from the central atom to the pivotal (nearest) atom of

the unit. For all angle parameters, the coordinates of the pivotal atom were kept constant.

All data was cut at 570 eV above the edge ($k = 12.2 \text{ \AA}^{-1}$), as data above this threshold was considered too noisy.

Linear combinations of both XANES and $\chi(k)$ spectra to fit experimental data were done using *Athena* from the *Demeter* Package [61].

4.2.7 EXAFS Refinements

Structural models were refined as to fit the EXAFS data using *Excurve*. Input models were designed from published crystal structures, and starting values of distances, Debye-Waller factors, angles and E_f were chosen iteratively. Up to 18 parameters were refined and the number of independent parameters was 20.

4.2.8 XANES Simulations

XANES was simulated using *FDMNES* [62]. *FDMNES* is a code based on the DFT method, which only computes ground states. As XAS is a spectroscopy of excited states, the code will have trouble calculating some features of the spectrum. Input structures were designed from the six popular crystal structures given in Table 4, and included full residues within 5 Å of Cu(II), and with added hydrogen atoms at ideal positions assuming all residues were neutral. Fitting was carried out partly by exact calculated spectra scanning selected parameters, and partly by using the interpolation scheme utilized in *FitIt* [63,64]. An extra electron was added in the lowest unoccupied state, i.e. the 4p orbital, by adding the keyword “screening” and the option “4. 1. 1.” in the input file for calculations, as this has shown to give better results [65].

4.3 Results

4.3.1 Experimental XANES

Six samples were measured at ESRF. As can be seen in Figure 17, PC(II) pH 6 data is representative of the PC(II) data at pH 4 and 8 and similar, yet not identical, to PC(I) pH 8.

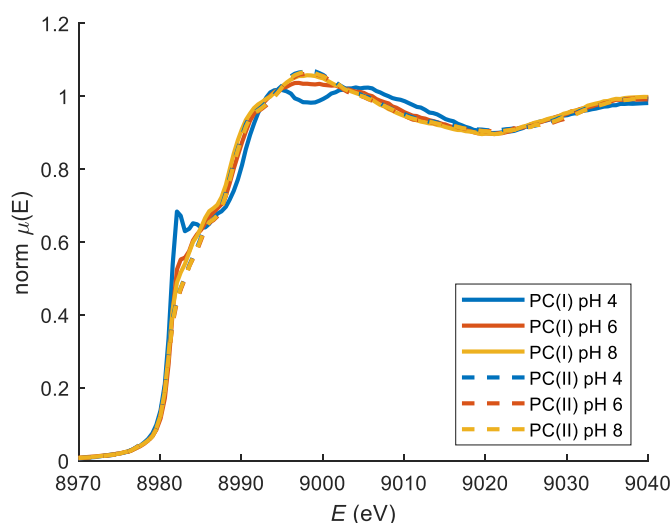


Figure 17 – XANES spectra of PC(I) and PC(II) samples measured at ESRF.

In Figure 18, the XANES region for the ESRF samples PC(II) pH 6 and PC(I) pH 4 can be seen along with the MAX II data PC(II)_c and PC(II)_s. The first derivative for all four datasets may also be seen in the inset.

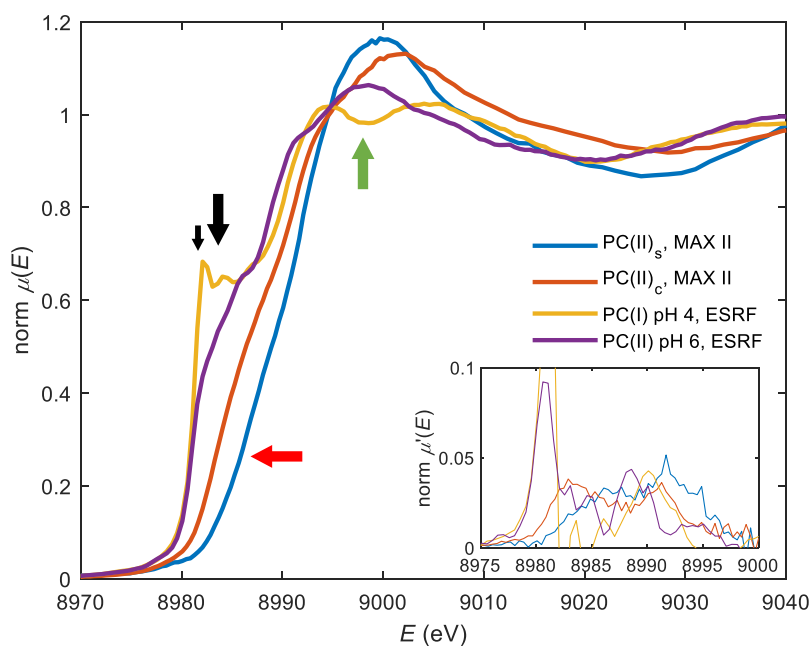


Figure 18 – Normalized XANES spectra for selected datasets. Spectra of PC(II) at pH 6 and PC(I) pH 4 measured at ESRF, and PC(II)_s and PC(II)_c measured at MAX II. Inset: First derivatives.

The two ESRF samples, PC(I) pH 4 and PC(II) pH 6 have the same position of the edge, (coinciding with the edge of all samples measured at ESRF, see Figure 17). It would be expected that all PC(II) samples have the same edge position at around 8992 eV, as is the case for the PC(II)_s, MAX II, highlighted in Figure 18 with a red arrow. This indicates that the PC(II) ESRF samples have been photoreduced. Moreover, the edge shoulder at 8984 eV (highlighted with a

large black arrow in Figure 18), which is seen in all Cu(I) spectra [15], is clearly visible. For the two samples measured at MAX II, the edge is clearly found at higher energies and no shoulder is seen.

The sharp edge feature in PC(I) pH 4 (marked with a small black arrow) indicates a geometry around copper, which is close to two-coordination [15], as also described in section 2.3. This has previously been described as a result of the combination of the weak bonding between Met92 and Cu(I), and His87 being protonated [66]. The protonation of His87 happens at lower pH as it has a pK_a of around 5 [67]. The PC(I) pH 6 is a mixture of the structures found at pH 4 and pH 8, and may be reproduced as a linear combination of those (Figure 19).

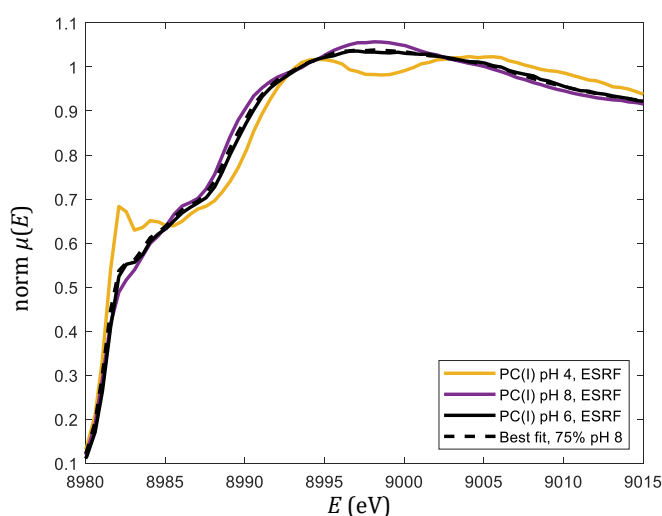


Figure 19 – XANES spectra of PC(I) pH 4, 8 and 6, ESRF, with the best combination of the former two to fit the latter

The main peak at 9000 eV (marked with a green arrow in Figure 18), has been described as a means to quantify the Cu(I) content, as the height decreases with increasing Cu(I) content [15]. The PC(II)_s sample has the lowest content of Cu(I), while the data obtained from the PC(II)_c sample has been slightly reduced. It has previously been described how it is possible to calculate the Cu(I) content of a specific sample if you have a fully oxidized sample, and a fully reduced sample [15]. It is assumed that the PC(II)_s sample is fully oxidized, and that the PC(I) pH 8, ESRF spectrum may be used as the fully reduced. Subtracting the fully oxidized dataset from the dataset in question, and then comparing the height of the peak at 8984 eV with the same of the fully reduced dataset (Figure 20, left) should give us the Cu(I) content (Figure 20, right). The three samples from ESRF has a Cu(I) content of about 90% while the PC(II)_c, MAX II sample has about 40%.

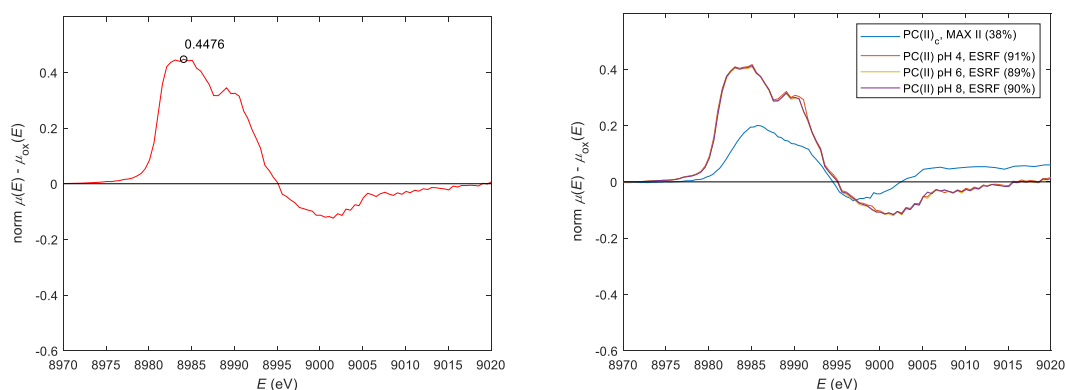


Figure 20 – Left: Normalized difference spectrum of PC(I) pH 8 measured at ESRF and PC(II)_s measured at MAX II. Right: Multiple normalized difference spectra of various datasets and PC(II)_s measured at MAX II (Cu(I) content in percentage).

4.3.2 EXAFS Refinements

k^3 -weighted $\chi(k)$ data for all samples may be seen in Figure 21.

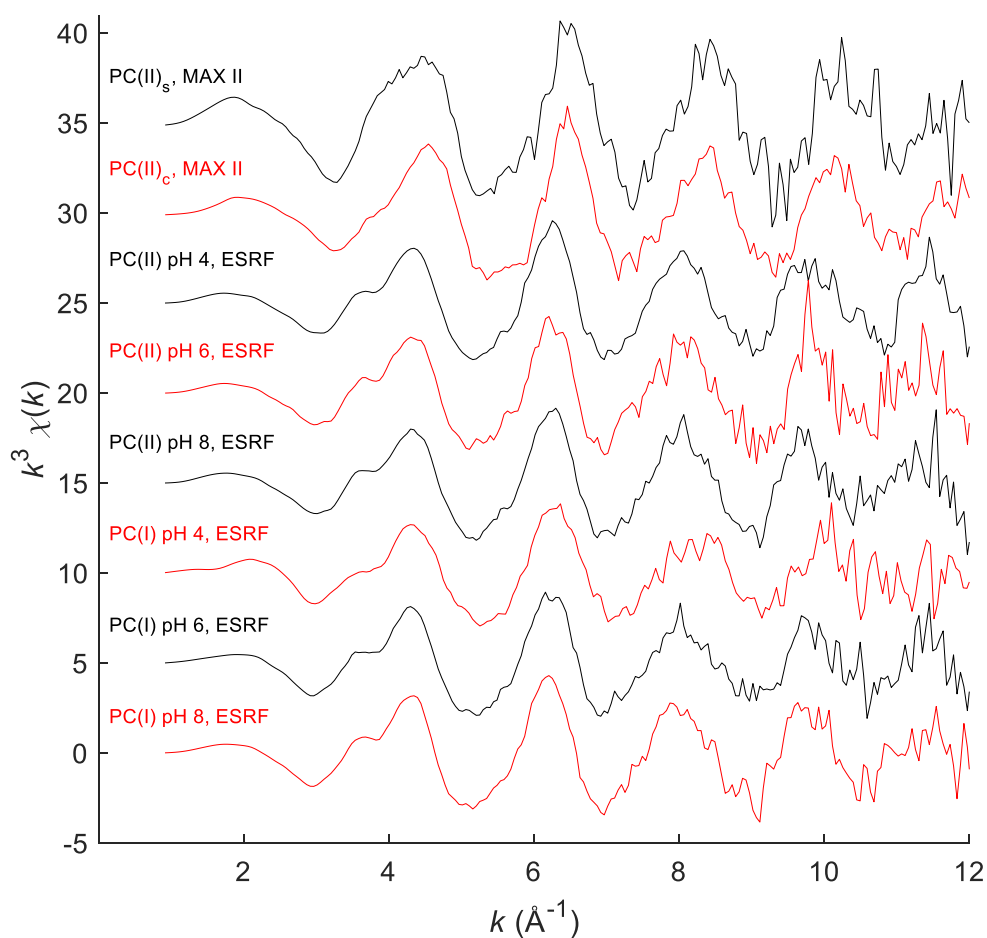


Figure 21 - k^3 -weighted EXAFS functions for all PC samples.

All the EXAFS spectra collected at ESRF are of the same good quality. The three photoreduced PC samples are very similar as shown in Figure 22 (top), where

also the EXAFS curve from PC(I) at pH 8 is shown. It may be seen that the differences between these curves are within the noise levels. In contrast to this, the spectra of the PC(I) samples show quite large difference between the signals at pH 4 and 8.0 (Figure 22 middle). The data measured at pH 6.0 seem to fall in between, as was visible in the XANES.

A comparison of the two EXAFS curves from MAX II data and PC(II) pH 8 measured at ESRF may be seen in Figure 22 (bottom). As expected from the XANES in Figure 18, the PC(II)_s, MAX II data appear different, especially at $k < 6 \text{ \AA}^{-1}$, while the PC(II)_c, MAX II data is similar to the photo-reduced PC(II) pH 8, ESRF data. However, the MAX II data is also more noisy at $k < 10 \text{ \AA}^{-1}$, compared to the ESRF data.

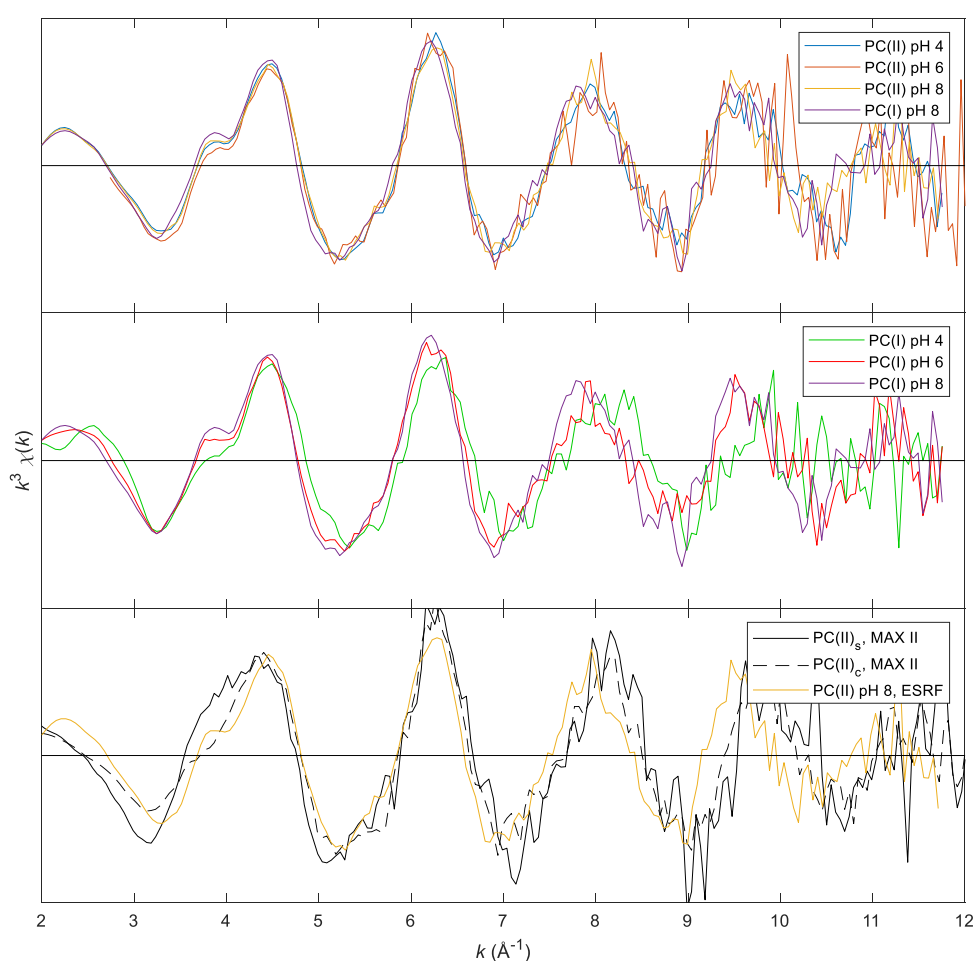


Figure 22 – k^3 -weighted $\chi(k)$ signals for top: PC(II) at pH 4, 6 and 8 and PC(I) at pH 8, middle: PC(I) at pH 4, 6 and 8, all measured at ESRF. Bottom: Photo-reduced PC(II) pH 8 and the two data sets from MAX II, PC(II)_s and PC(II)_c.

ESRF data

The EXAFS fits to the three PC(II), ESRF samples and the PC(I) pH 8, ESRF sample all give parameters similar to those of the crystal structures of poplar

PC at their respective pH and oxidation states. The fits are shown in Figure 23 and the resulting refined parameters in Table 5.

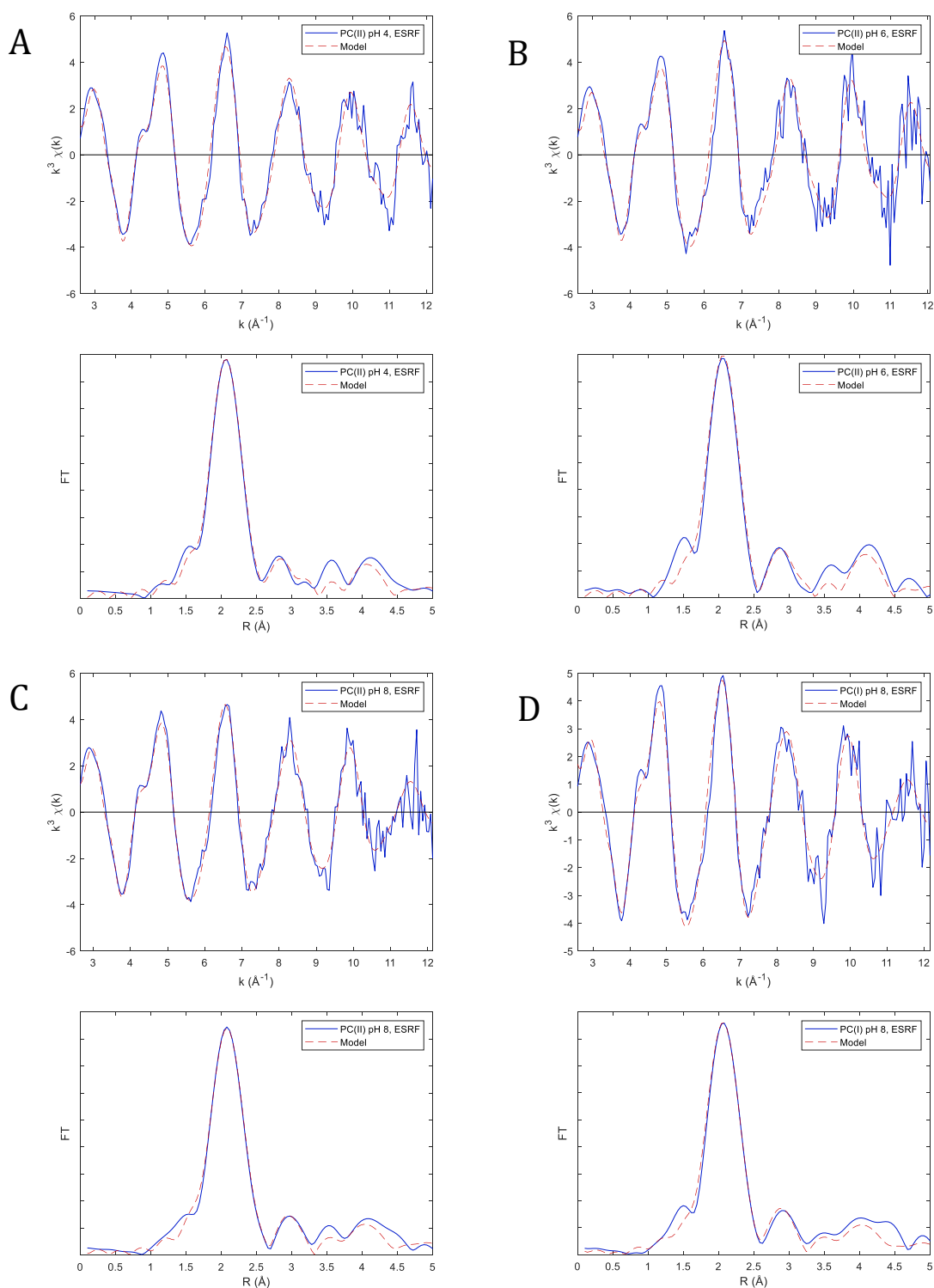


Figure 23 – EXAFS calculated (red dash) and experimental (blue solid) k^3 -weighted $\chi(k)$ and the Fourier transform hereof for photoreduced PC(II) at pH A) 4, B) 6, C) 8 and D) PC(I) pH 8.

Table 5 – Refined geometrical parameters for PC(II) at pH 4, 6, and 8, ESRF and PC(I) pH 8, ESRF. XRD indicates the corresponding parameters found in the crystal structures of poplar PC(II) and PC(I) with PDB ID 4DP7, 4DP9, 4DPB, and 4DPC, respectively.

ESRF						
	PC(II) pH 4			PC(II) pH 6		
	XRD (4DP7)	Constrained EXAFS		XRD (4DP9)	Constrained EXAFS	
	R (Å)	R (Å)	σ^2 (Å ²)	R (Å)	R (Å)	σ^2 (Å ²)
His37 (N _δ)	1.96	1.94(2)	0.006(2)	1.94	1.95(3)	0.004(3)
Cys84 (S)	2.14	2.17*	0.003(1)	2.16	2.17*	0.003(3)
His87 (N _δ)	2.04	2.08(2)	0.003(5)	1.99	2.11(4)	0.002(2)
Met92 (S)	2.78	2.71(5)	0.018*	2.78	2.8(1)	0.018*
	PC(II) pH 8			PC(I) pH 8		
	XRD (4DPB)	Constrained EXAFS		XRD (4DPC)	Constrained EXAFS	
	R (Å)	R (Å)	σ^2 (Å ²)	R (Å)	R (Å)	σ^2 (Å ²)
His37 (N _δ)	1.97	1.94(2)	0.004(3)	1.98	1.96(2)	0.002(4)
Cys84 (S)	2.17	2.18(2)	0.003(2)	2.18	2.19(2)	0.004(3)
His87 (N _δ)	2.02	2.10(3)	0.005(14)	2.10	2.10(3)	0.003(23)
Met92 (S)	2.76	2.70(6)	0.018*	2.71	2.82(9)	0.018*

*This parameter was not included in the refinement, and was thus constrained at the given value

Including angular parameters resulted in better fits to the experimental data.

The crystal structure of poplar PC(I) at pH 4 (PDB ID: 4DP8) was used as input for PC(I) pH 4. The fit can be seen in Figure 24 and the parameters in Table 6.

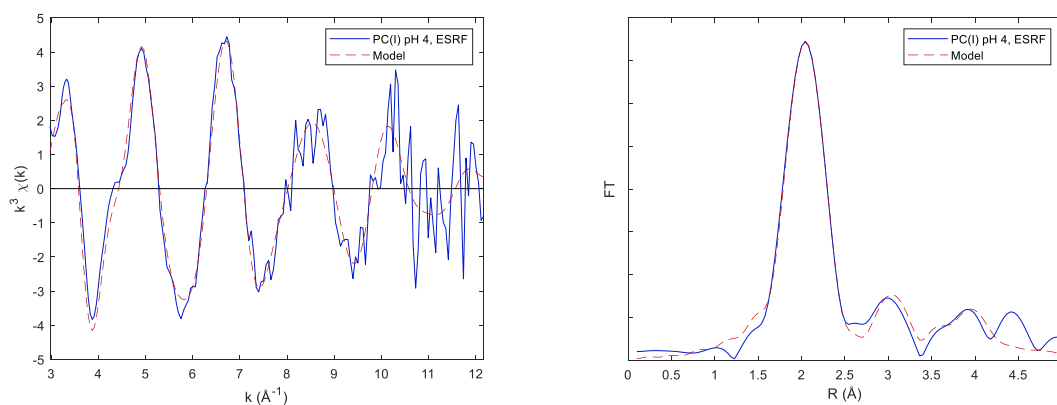


Figure 24 – EXAFS calculated (red dash) and experimental (blue solid) k^3 -weighed $\chi(k)$ (left) and its Fourier transform (right) for PC(I) pH 4, ESRF.

Table 6 – Refined geometrical parameters for PC(I) at pH 4, ESRF. XRD indicates the corresponding parameters found in the crystal structure with PDB ID 4DP8.

Plastocyanin Cu(I), ESRF			
	pH 4		
	XRD (4DP8)	Constrained EXAFS	
	R (Å)	R (Å)	σ^2 (Å ²)
His37 (N ₆)	1.88	1.97(4)	0.004(3)
Cys84 (S)	2.10	2.16(4)	0.008(4)
His87 (C ₆)	3.47	3.69(6)	0.002(6)
Met92 (S)	2.39	2.1(1)	0.018*

*This parameter was not included in the refinement, and was thus constrained at the given value

The crystal structure for poplar PC(I) pH 4 has His87 in two conformations, 75 % flipped and 25 % non-flipped. This could explain the difference in distances found when comparing our EXAFS fit to the XRD structure.

As the structure of PC(I) at pH 6 is expected to be a combination of the structure seen at pH 4 and pH 8 a Linear Combination fitting was used to fit the spectrum of PC(I) at pH 6, using the spectra at pH 4 and 8 as standards. The best fit ($R = 0.029$, seen in Figure 25) was found with a fraction of 0.32 of PC(I) pH 4 and a fraction of 0.68 of PC(I) pH 8. If we use these values to calculate a pK_a while assuming that at pH 4 we have 75 % acid form as according to the PDB-file (PDB ID: 4DP8), we get a value of 5.5, which is slightly higher than the ones determined by NMR [67–70].

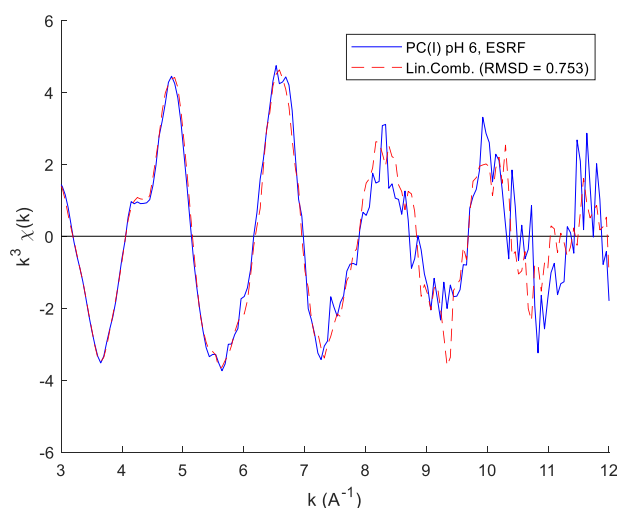


Figure 25 – Result of linear combination fit of experimental spectra from PC(I) at pH 4 and 8 to spectrum obtained at pH 6, compared with the experimental spectrum.

MAX II Data

The best fit for the PC(II)_s and PC(II)_c signals and their FT can be seen in Figure 26. The PC(II)_s data was noisier as seen in Figure 26B, giving parameters with higher uncertainties. The final parameters from both refinements can be found in Table 7.

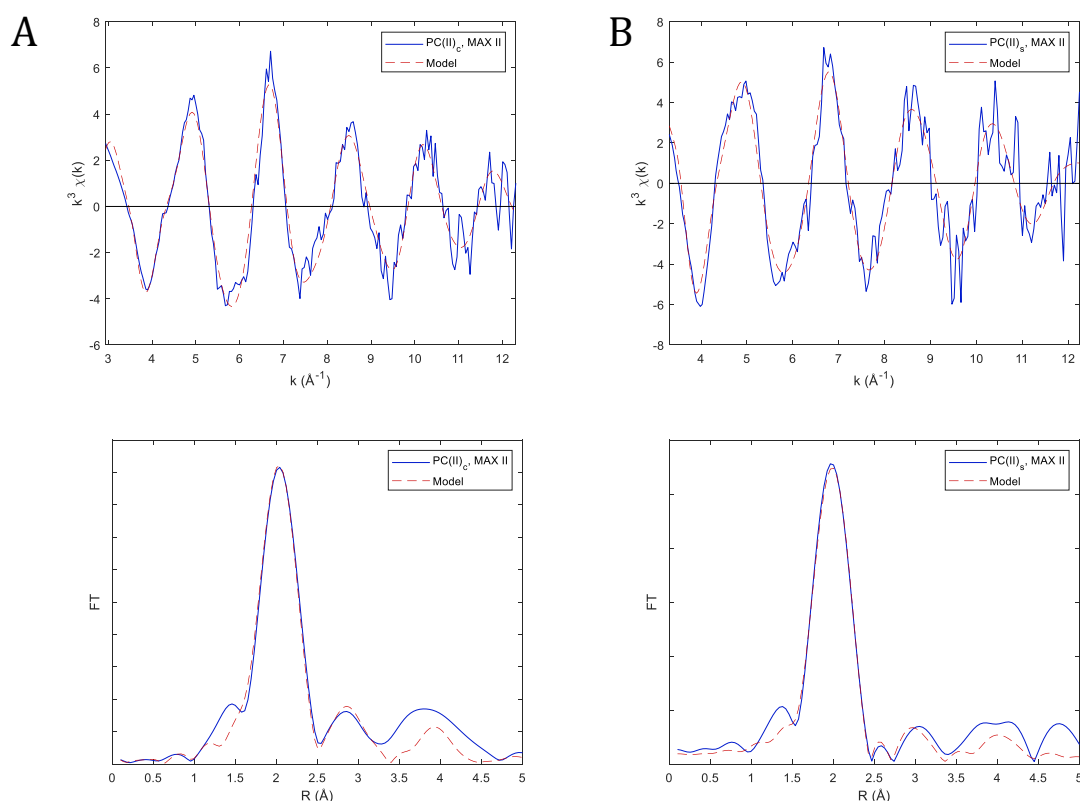


Figure 26 – EXAFS theoretical calculated k^3 -weighted $\chi(k)$ and the Fourier transform hereof for A) PC(II)_c, MAX II and B) PC(II)_s, MAX II.

Table 7 - Refined geometrical parameters for PC(II)_c. XRD indicates the corresponding parameters found in the crystal structure of poplar PC(II) (PDB ID: 4DPB) and of the Av crystal structure (PDB ID: 2GIM).

	Plastocyanin Cu(II), MAX II						
				pH 8.5, crystalline		pH 6.5, solution	
	XRD (4DPB) R (Å)	XRD (2GIM-A) R (Å)	XRD (2GIM-B) R (Å)	Constrained EXAFS		Constrained EXAFS	
			R (Å)	σ^2 (Å ²)	R (Å)	σ^2 (Å ²)	
His37 (N ₆)	1.97	2.07	1.99	1.91(2)	0.002(3)	1.90(9)	0.001(6)
Cys84 (S)	2.17	2.13	2.23	2.13(4)	0.002(2)	2.12(2)	0.003(6)
His87 (N ₆)	2.02	2.10	2.07	2.08(5)	0.003(20)	2.00(8)	0.003(30)
Met92 (S)	2.76	2.77	2.72	2.67(8)	0.012(10)	2.9(3)	0.02(9)

4.3.3 XANES Simulations

XANES spectra were calculated for all the crystal structures listed in Table 4. The spectra may be seen in Figure 27. The three poplar PC(II) structures, the PC(I) pH 8 structure, as well as the *A.v.* PC(II) structure are all similar, while the PC(I) pH 4 and 6 stand out.

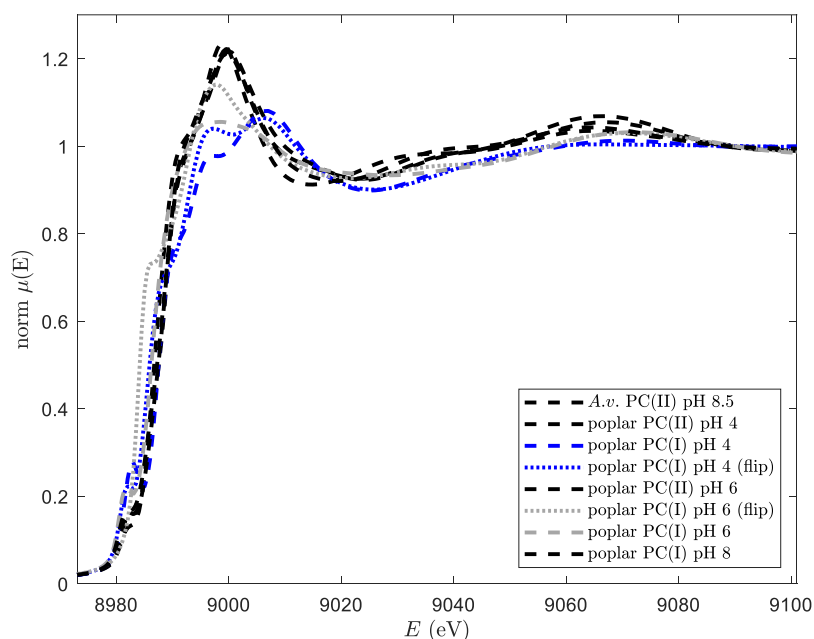


Figure 27 - Simulated XANES of the crystal structures listed in Table 4

A comparison of the experimental PC(II)_s, MAX II and PC(II) pH 6, ESRF data to the calculated XANES spectrum of PC(II) pH 6 (PDB ID: 4DP9) may be seen in Figure 28. It may be observed that the simulated spectrum for the PC(II) structure is most similar to the experimental spectrum of PC(II)_s, MAX II, although clear differences are still apparent.

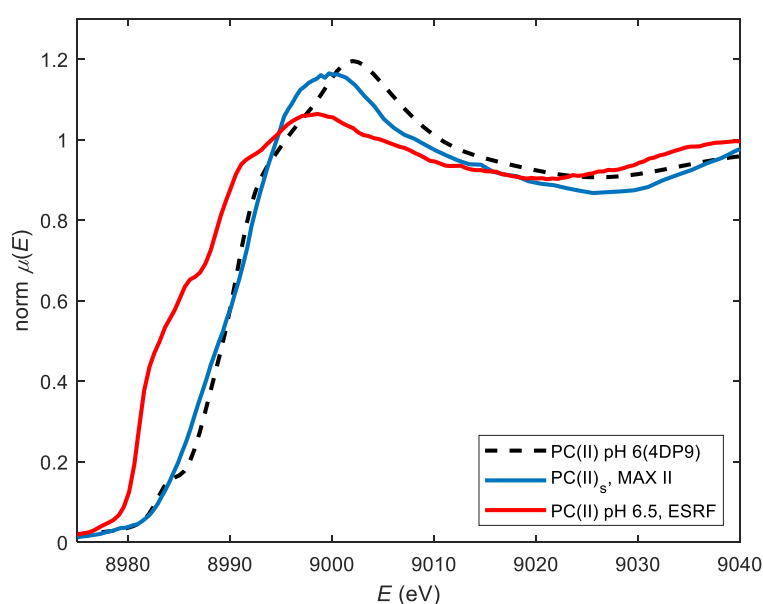


Figure 28 – Experimental (solid) and calculated (dashed) XANES spectra.

To investigate what structural features are causing the difference between the spectrum from MAX II and the spectrum from ESRF, the effect of the histidine distances were investigated by calculating 100 combinations of His37 and His87 distances to the copper. The result can be seen in Figure 29 and the parameters of the best fit to the MAX II data are listed in Table 8. A small effect was observed by moving the cysteine further away (data not shown).

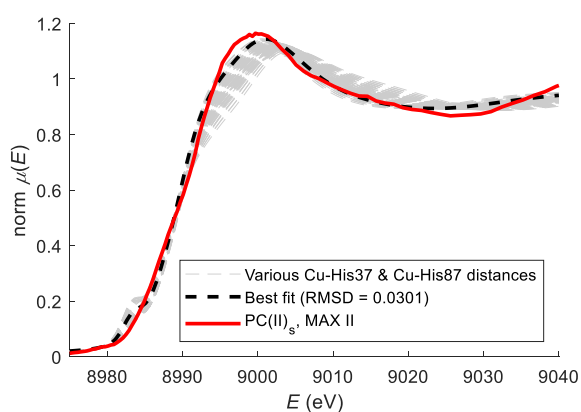


Figure 29 – Simulated XANES of one hundred combinations of His37 and His87 distances compared to the experimental spectrum of the PC(II)_s measured at MAX II.

Table 8 – XANES refined geometrical parameters for PC(II)_s. XRD indicates the corresponding parameters found in the crystal structure with PDB ID 4DP9.

PC(II) _s , MAX II		
	XRD (4DP9) R (Å)	XANES fit R (Å)
His37 (N _δ)	1.94	1.97
Cys84 (S)	2.16	2.16
His87 (C _δ /N _δ)	1.99	2.03
Met92 (S)	2.78	2.78
<i>R</i> _{XANES}		0.0342

Fitting of MAX II PC(II)_c as well as the photoreduced ESRF data was then attempted by adding a 4p electron to screen the core-hole, to simulate the effect of photoreduction (Y. Joly, personal communication). The best fits were achieved by having 20% and 22% of the spectrum with the 4p electron, as visible in Figure 30.

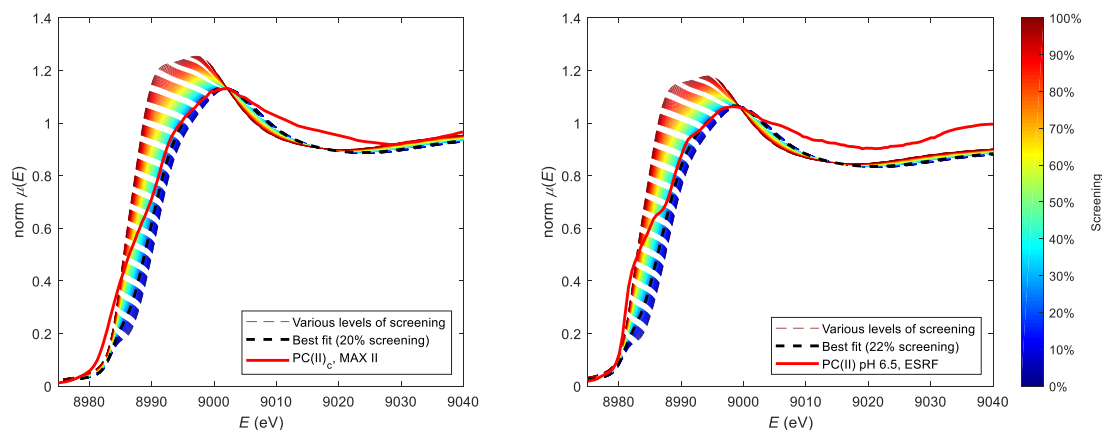


Figure 30 – Simulated XANES of the best fit to PC(II)_c, MAX II and PC(II) pH 6, ESRF with one 4p electron screening the core-hole in various amounts. Input model was the result of the fit to PC(II)_s, MAX II data.

PC(I) pH 4 data was compared to two models of the poplar PC(I) pH 4 crystal structure (PDB ID: 4DP8) as this has His87 in two conformations; flipped and non-flipped (Figure 31).

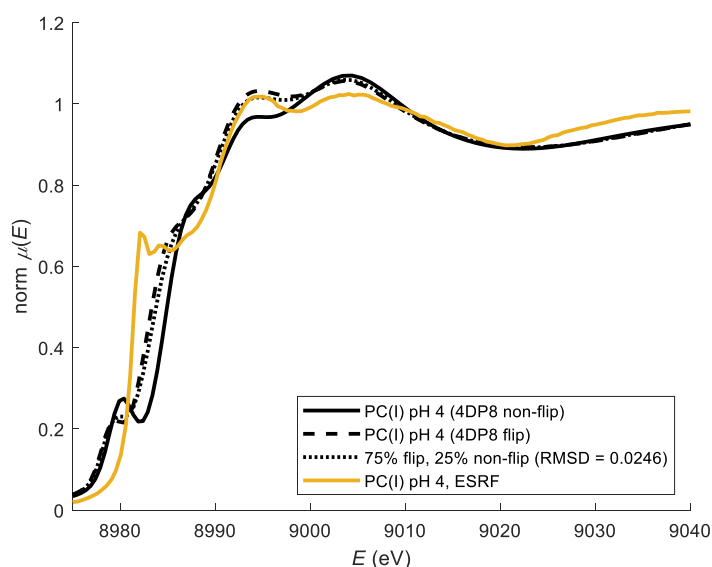


Figure 31 – Experimental (yellow) and simulated (black) XANES spectra.

As expected from the occupancy of this conformation in the crystal structure (75%), it seems that the simulation of the structure with a flipped His87 resembles the data the best. The prepeak feature at ~ 8982 eV, which is higher for 2- and 3-coordinated Cu, is not very well reproduced in the simulation. It was attempted to fit this data by adjusting two parameters in the structure, the Cu-His37 and the Cu-Cys84 distances, as seen in Figure 32. While most of the datapoints are covered by a theoretical point, no single curve is able to reproduce the experimental. The pre-edge is the only part that is not covered at all, as the intensity of none of the theoretical spectra reach that of the experimental.

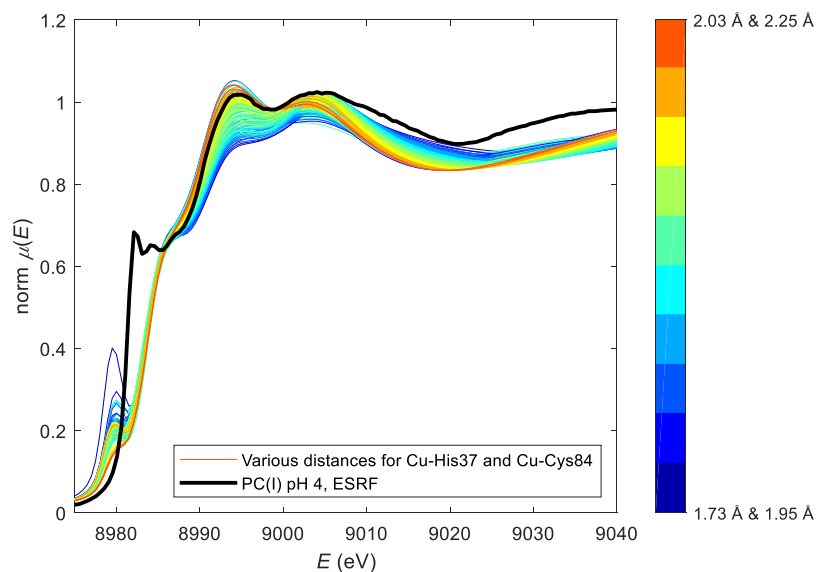


Figure 32 – Experimental data is black and dashed. A) Simulation of XANES of the PC(I) pH 4 crystal structure (4DP8) with varying Cu-His37 and Cu-Cys84 distance.

4.4 Discussion

Out of the six datasets measured at ESRF, only the PC(I) pH 4 data clearly stand out from the rest. While the edge position for the PC(II) samples is identical to that of the PC(I) samples, the shapes of the XANES for photoreduced PC(II) pH 4 and PC(I) pH 4 are not identical, as the latter has an edge feature normally associated with an almost linear Cu(I) coordination. Thus, photoreduced PC(II) pH 4 appear to retain part of the geometry known for Cu(II). This could indicate two things. One is that having the samples cooled to 4 K constrains the active site to a point where His87 cannot flip, or will not become protonated even though the copper ion gets reduced. Another explanation might be that the reduction as a function of radiation does not induce the same changes as chemical reduction. A similar observation has been made with myoglobin, where the photoreduced structure is different from normal deoxy Fe(II) myoglobin [71]. It has also previously been shown that photoreduction of iron clusters in ribonucleotide reductase result in minor changes at low temperatures [72].

The data measured at MAX II experienced less (30% Cu(I) in PC(II)_c, MAX II) or no photoreduction. A direct comparison of the PC(II)_s MAX II and the photoreduced PC(II) pH 6 dataset measured at ESRF shows a clear shift to the right in the Fourier transform (Figure 33), but also a broadening of the main peak. The height of the peak could be explained by the Debye Waller factors of the closest shells, which is indeed $\sigma^2 = 4 \cdot 10^{-3} \text{ \AA}^2$ for the ESRF data, and $1 \cdot 10^{-3} \text{ \AA}^2$ for the MAX II data. The broadening and shift of the main peak could indicate

that the shells are found at distances in a larger interval, closer to the copper atom. While the three closest shells of the ESRF model are in an interval of 1.95-2.17 Å, the same shells are in an interval of 1.90-2.10 Å for the MAX II data. Thus, the broadening is not entirely explained by the EXAFS results while the shift indeed is. In this regard, it should be noted that the occupancy of each shell was fixed, which may have affected both distances and Debye Waller factors.

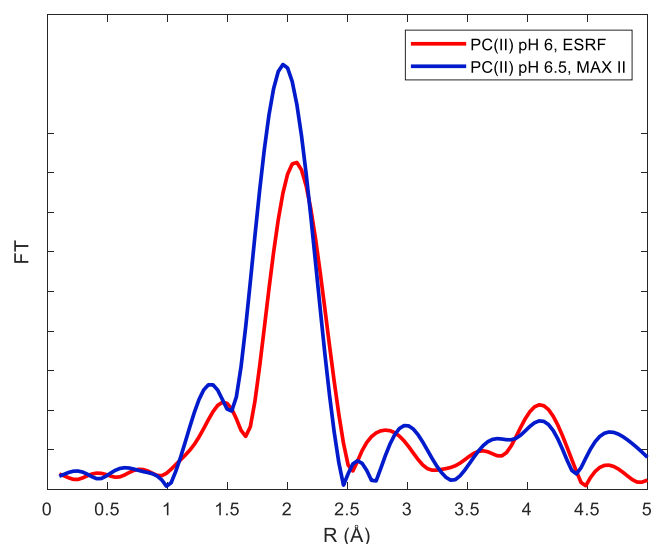


Figure 33 – Fourier transform of $\chi(k)$ data from PC(II) data from MAX II and ESRF.

While 3 of 7 of the EXAFS experiments referred to in Table 4 cannot distinguish the two histidine distances, the remaining three has a difference of less than 0.05 Å. In the current study, the differences in distance found from EXAFS refinements are at least 0.1 Å. This is because the current study finds the distant His at a distance of about 2.10 Å from the copper atom, while other studies find it around 2.0 Å. This could be due to the photoreduction of the samples, as His87 is the one that is far away in the reduced structure, and the least photoreduced sample PC(II)_s finds it at 2.00 Å.

The situation in which the PC(II) in solution at different pH values seem to fit the crystal structures, but at the same time are concluded to be photoreduced from the position of the edge, could lead to the conclusion that the ultrahigh resolution crystal structures also represent photoreduced geometries around the copper site. Although the authors behind the diffraction experiment report that no bleaching of the crystal was observed after exposure to the beam [52], and the oxidized and reduced structures at pH 4 are very different, it is likely that the metal ion was reduced by the photon beam during data collection. Thus, the PC(II)_s and PC(II)_c measured at MAX II, that exhibit less photoreduction at the edge, could be clues towards the actual geometry around Cu(II) in PC. However, possibly due to relative low quality of data, EXAFS

refinements were unable to point out which parameters should be changed and how much.

4.4.1 *Effect of cryoprotectants*

The samples measured at MAX II did not have glycerol added. This lowered the data quality due to diffraction from ice formation when the samples are cryocooled. The samples measured at ESRF all had glycerol added, which gave high data quality, but also high photoreduction of the copper center.

It has been shown that some cryoprotectants increase the damage caused by radiation [73], while another study has shown that embedding the protein in a saccharose matrix decrease it [74]. The increased damage is suggested to arise due to reactions between the cryoprotectant and the highly oxidative radicals also formed by radiation of water, resulting in even more reduction agents. The positive effect of a saccharose matrix is explained by a hindrance of the mobility of the reactive species.

4.4.2 *Angles*

Including twisting and tilting angular parameters resulted in significantly better fits. By including the angular parameters, only the Debye Waller factors were affected compared to the best fit without angular parameters. The sulfur atom of methionine had its Debye Waller factor halved, while C_δ and N_ϵ of both histidine rings had theirs more than halved. The final models for PC(II) pH 4, 6, and 8 and PC(I) pH 8, ESRF can be seen compared to the crystal structure of poplar PC(II) pH 6 in Figure 34. His87 is tilted out of the plane while His37 is rotated around the normal to the plane. Interestingly, one would expect the multiple scattering signal from the N_δ and N_ϵ atoms of the ring to be weakened when the ring is tilted out of the plane, and perhaps this can explain the decrease in Debye Waller factors for these atoms.

Including more parameters would possibly lead to a better fit, but would be expensive with respect to CPU time. The number of independent points were at least 20 [26], while no more than 18 parameters were fitted at any point, achieved by grouping related Debye-Waller factors and treating amino acids as rigid bodies. Including more parameters may then result in overfitting.

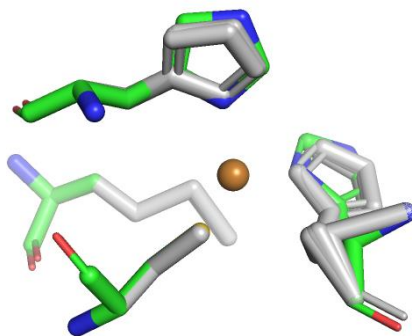


Figure 34 – Crystal structure of poplar PC(II) pH 6 (PDB ID: 4DP9) in green and EXAFS fitted models to PC(II) pH 4, 6 and 8 and PC(I) pH 8, ESRF in grey.

4.4.3 XANES Fit

Calculated XANES for the model structures were unable to reproduce the difference seen between experiments on the same sample with and without photoreduction. This indicates that the DFT method of *FDMNES* utilized in this study is inadequate to describe the effect. While it is possible to distinguish the difference in geometry of high and low pH PC(I), fitting of parameters was unsuccessful. It would be interesting to investigate whether other codes not based on DFT could achieve better fits, and thus be used quantitatively.

4.5 Conclusion

PC data from two beamlines with different flux has been compared, and both XANES and EXAFS signals are clearly different. While neither XANES nor EXAFS refinements were able to distinguish the datasets, the EXAFS refined models for the photoreduced data, are similar to the ultrahigh resolution crystal structures published to the PDB, suggesting that the crystal structures are also affected by radiation damage.

Photoreduction of biological samples is a problem that will increase as synchrotrons strive towards higher brilliance. For XRD structures, it is impossible to see if a metal ion has been reduced by the beam, which might influence the geometry, even when the sample is cooled to 4 K. In this work, it is demonstrated that XAS is able to monitor the photoreduction of Cu(II) in PC, but unable to resolve the geometrical effect. Improving the theory of XANES calculations as well as obtaining higher quality XAS data without radiation damage may assist in solving this challenge. To avoid photoreduction altogether, strong precautions should be implemented. Furthermore, the development of flow cells to replenish sample during measurements could help to overcome the issue.

5

Using Design of Experiment to Optimize EXAFS Refinements

5.1 Introduction

Resolving EXAFS spectra is challenging due to the combination of noise, mixture of species, and overfitting. Refining a structural model using *Excurve* may be challenging, due to the complex nature of how the parameters correlate.

Excurve refinement uses Harwell routine VA05A, using numerical estimates of the derivatives. An example using one parameter is shown in Figure 35. In step 1, the theoretical spectrum with the parameter set to its initial value is calculated and compared to the experimental, giving an initial value of R_{EXAFS} . Next, the parameter is increased according to the step size. Depending on the new value of R_{EXAFS} , the parameter is changed further in the same direction or changed in the opposite direction in step 3. This continues until the parameter reaches a local minimum, i.e. R_{EXAFS} increases in both directions.

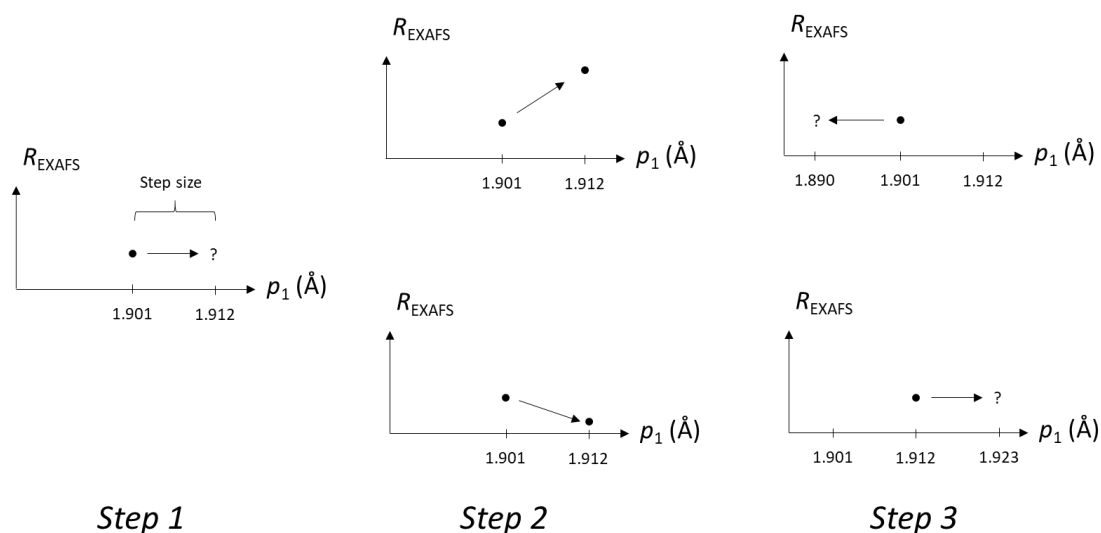


Figure 35 – Schematic of the refinement procedure in *Excurve*. In step 1, the spectrum corresponding to the model with parameter 1 (p_1) set to its initial value is calculated. In step 2, the parameter is changed according to the step size. Depending on the effect of this new value on the fit, in step 3, the parameter is changed in the other direction (top) or is changed further in the same direction (bottom).

Using this procedure, it is hard to find the global minimum, as the parameters cannot be changed beyond a local minimum. Thus, using the right initial parameters and a right step size is key in the search.

The work on plastocyanin described in chapter 4, was complicated in choosing which parameters needed to be changed in order to achieve a better fit. As each parameter affects the $\chi(k)$ differently, a statistical analysis might resolve what parameters led to a better fit, and perhaps train a model to predict parameter values that would result in a better fit than what the refinement procedure of *Excurve* could achieve.

5.2 Methods

In collaboration with Åsmund Rinnan (University of Copenhagen), a Design of Experiment (DoE) was developed, to investigate the contribution of a range of parameters on a crystal structure of plastocyanin, to fit the dataset mentioned as PC(II) pH 4, ESRF in chapter 4. The crystal structure used was the 1.0 Å resolution structure of poplar plastocyanin at pH 6 (PDB ID: 4DP9). The DoE consists of 1024 combinations of a number of parameters at either their maximum or their minimum value in a specified range. Part of the DoE is presented in Table 9.

Table 9 – Section of the DoE made for EXAFS refinements. All 1024 calculations used the same interval. Min indicates that the parameter was set to its minimum value in the interval, and Max that it was set to its maximum.

Parameter/ Calculation #	1	2	3	4	5	6	7	8	9	1024
p ₁	Max	Min								
p ₂	Max	Max	Min	Min	Max	Max	Min	Min	Max	Min
p ₃	Max	Max	Max	Max	Min	Min	Min	Min	Max	Min
p ₄	Max	Min	Min							
p ₅	Max	Min								
p ₆	Max	Min								

Out of 26 parameters possible for the structure, some were grouped, giving 18 parameters. Each parameter was given a chemical reasonable interval, and 50 sets of calculations using *Excurve* were executed (Run 1), each with a random, smaller interval chosen within the larger interval. One set consisted of 1025 calculations, with the 1024 following the DoE, taking maximum and minimum values in the smaller interval, and the 1025th calculation having all parameters as their mean value in the interval.

To optimize the fit, 50 new sets of calculations were done (Run 2), where the interval of each parameter was chosen depending on the effect of it in the previous set of calculations. The idea is explained for two parameters in Figure 36.

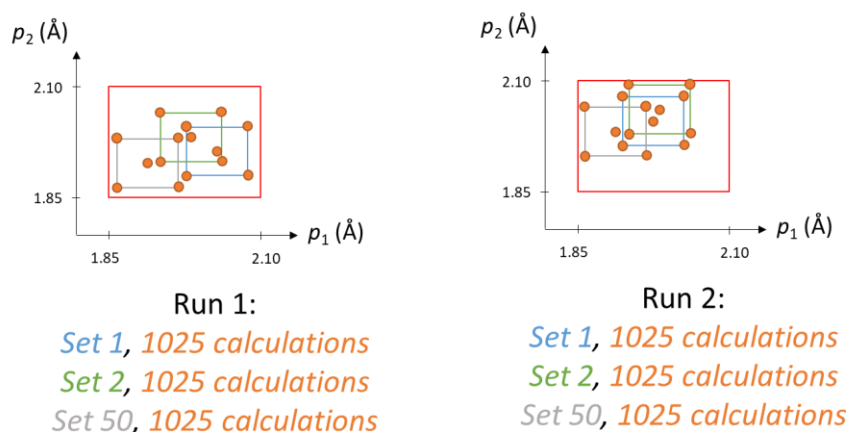


Figure 36 – Concept of procedure for finding a better fit using a DoE for 18 parameters over two runs of 50 sets of 1025 calculations. Here shown for only two parameters. The red box sets the limits for the overall interval for each parameter. As only minimum and maximum values are calculated, each calculation is on the corners of the smaller interval (blue, green and grey boxes).

5.3 Results and Discussion

The R_{EXAFS} for all $50 \cdot 1025$ calculations for both Run 1 and Run 2 can be seen in Figure 37. Two sets were not calculated (17 and 29), as some of the values suggested for the parameters were outside of the overall interval defined for those parameters.

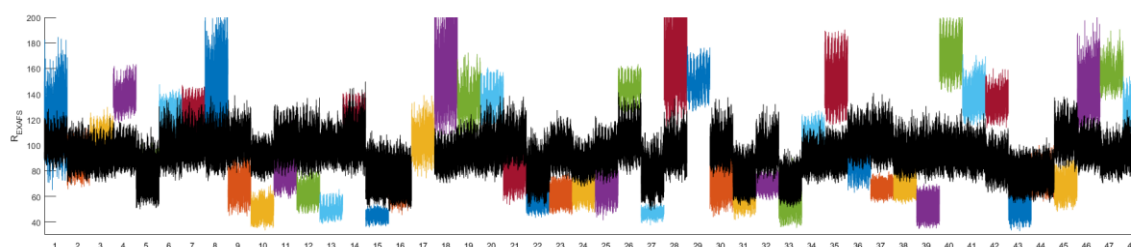


Figure 37 – R_{EXAFS} for the 1025 calculations for each of the 50 sets for Run 1 (colored) and Run 2 (black). X-axis shows the set number.

While the effect expected is that R_{EXAFS} goes down for each set from Run 1 to Run 2, this only happened for 22 of the 48 sets calculated. As can be seen, the initial random intervals achieved better fits than the optimized. Another point of interest is that the spread in R_{EXAFS} is much smaller for the second run, compared to the first run. It appears as if the procedure has caused all sets to converge towards parameters with semi-poor values. Perhaps some parameters achieve what could be described as good values (i.e. resulting in a good fit) in the first run, but changing the interval towards the good value, resulted in an interval with poorer values. However, as the values from the previous fit were kept at middle points and calculated as the last one in each set that one would stand out from the rest, which is not apparent. Possibly, the change in parameters (the step size) going from Run 1 to Run 2 was too large.

The best fit achieved in Run 1 with random values is a good fit ($R_{\text{EXAFS}} = 33.4$), seen in Figure 38.

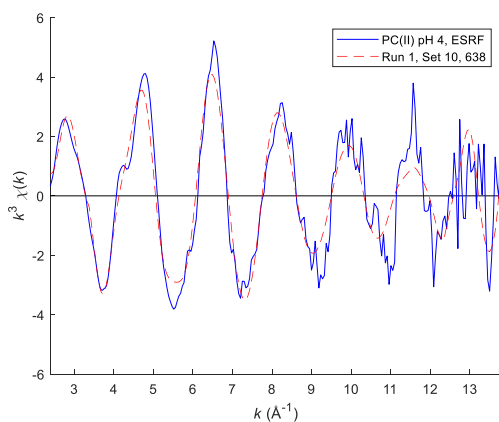


Figure 38 – The theoretical model with the lowest R_{EXAFS} compared to the experimental data of PC(II) pH 4, ESRF.

Further development to the procedure is required, but as the best fits achieved with random values were close to the experimental data, it is hard to imagine that adjustments to the procedure could not achieve a better fit.

6

The Coordination of Cu(II) and Zn(II) in Amyloid- β Fibrils

In this chapter, the focus is on amyloid- β ($A\beta$), a peptide related to Alzheimer's Disease (AD). With relation to this topic, I have conducted ThT fluorescence measurements, and collected XAS data on fibrils formed by two variants of the peptide and the wild type with Cu^{2+} and Zn^{2+} present at pH 7, 8 and 9. The samples will be denoted $(M-var)_{pH}$, where M is the metal and *var* is the variant of $A\beta$, either wild-type (WT), A2T or A2V.

6.1 Biological Background

AD is the most common form of dementia suffered by millions of people around the world. In Denmark, the Danish Dementia Research Centre estimates almost 90,000 people living with dementia [75], and with a growing elderly population [76], that number is expected to be above 100,000 in 2025.

AD is a complex illness that is clinically diagnosed by plaques of $A\beta$ outside the neurons and neurofibrillary tangles within. However, later findings that healthy patients also have plaque [77–79], and indications that $A\beta$ is essential to brain function [80], shows that this type of diagnosis is insufficient.

$A\beta$ is a peptide that is cleaved from the amyloid precursor protein (APP) by γ -secretase and β -secretase, see Figure 39. The plaque in infected brains consist of peptide with various lengths, of which 1-40 and 1-42 are the most common (hereafter denoted $A\beta(1-40)$ and $A\beta(1-42)$, respectively).

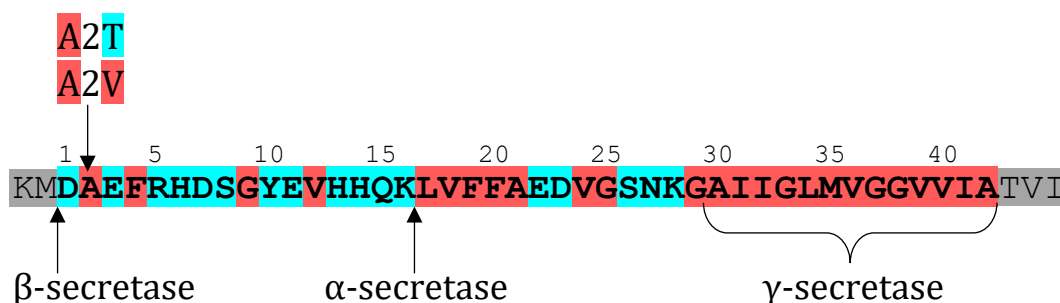


Figure 39 – The sequence of the amyloid- β ($A\beta$) part of the amyloid precursor protein (APP), colored according to hydrophobicity. The sites of α -, β - and γ -secretase cleavage are highlighted, as well as two disease related mutations that will be the focus of the current study. Greyed sections are part of the APP.

The amyloid hypothesis has been central in the research of AD, and has changed accordingly [81]. It describes the theory of how the formation of $A\beta$ oligomers

in a cascade of events leads to AD [82,83]. The production of A β and conversion into oligomeric species is visualized in Figure 40. The cause of the conversion from soluble A β to the toxic species causing AD is unknown.

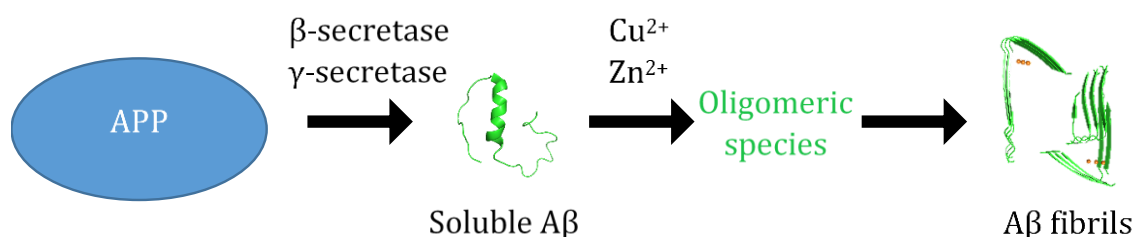


Figure 40 – Cleavage of APP to give soluble A β , and formation of oligomeric species with various unknown geometries, and further conversion into fibrils, possibly with metals coordinated (orange sphere).

6.1.1 The Structure of A β

Due to its high flexibility, the solution structure of A β has proven hard to determine. NMR studies have found different helical structures in HFIP/H₂O solution [84], sodium dodecyl sulfate (SDS) micelles [85,86] and trifluoroethanol/H₂O mixtures [87].

A β may aggregate, either in a myriad of oligomers or as structured fibrils with a high β -strand content [84]. While a consensus on the secondary structure of the fibrils seem to have established, the quaternary structure has been investigated and discussed [88–94]. The overall structure consists of two β -strands connected by a hairpin loop. The C-terminal β -strands interacts with each other to form a layer in the fibril. NMR studies disagree on whether the N-terminal is a highly structured β -strand [94] or a flexible loop [89], though most identify His13 and His14 as part of a β -strand. The structure of A β_{1-42} fibrils was recently solved at near atomic resolution using cryogenic electron microscopy (cryo-EM) [95]. A comparison between this, and one NMR structure can be seen in Figure 41. Notice that the NMR structure is of A $\beta(1-40)$ while the cryo-EM is of A $\beta(1-42)$, and the fibril structure may very well be affected by this. Nonetheless, the NMR structure indicate a flexible N-terminal, while the cryo-EM structure indicate a highly structured β -strand for the N-terminal. Furthermore, NMR finds the β -strand of residues 30-36 to constitute the dimer interface, while cryo-EM finds another, shorter β -strand in the C-terminal to accomplish this.

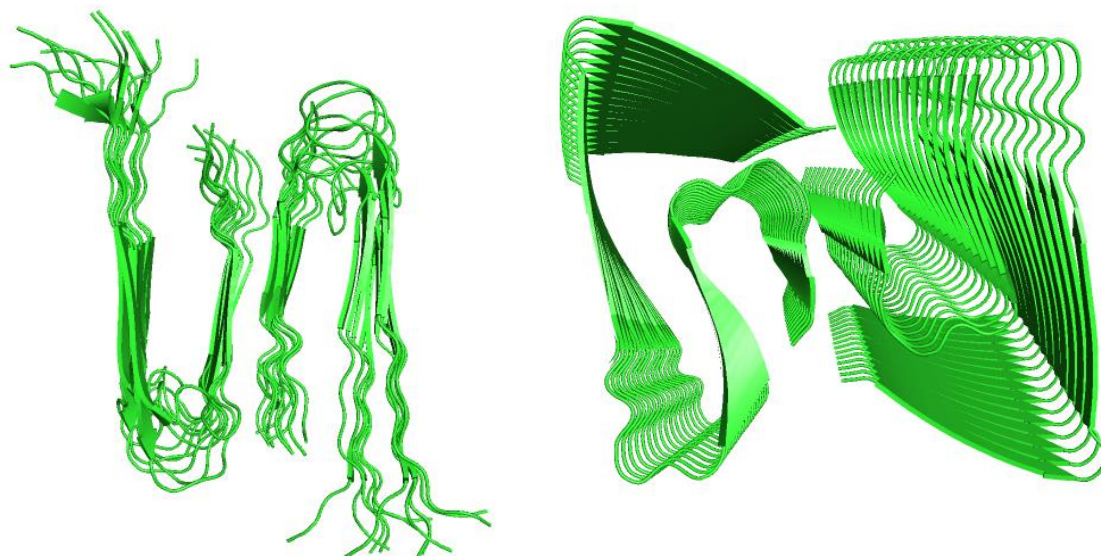


Figure 41 – Cartoon representation of A β fibrils along the fibril axis. Left: One conformer of the NMR structure (PDB ID: 2LMN) of A β (1-40) with a two-fold symmetry. Right: Cryo-EM structure of A β (1-42) (PDB ID: 5OQV).

6.1.2 The Role of Metals

Copper, zinc and iron has been found in high concentrations in the plaque [96], and it has been suggested that the combination of A β with some of these metals might be part of the cause to AD, as they affect aggregation [97,98]. Other roles of metals has been reviewed [99–101], and includes the formation of reactive oxygen species which could cause damage in the brain tissue.

Both Cu(II) and Zn(II) has been shown to inhibit fibril formation, but enhance nonfibrillar aggregation of A β [97,102]. The inhibitory effect is concentration dependent, and upon prolonged incubation, fibrils are formed [103]. While Cu(II) has been implicated in redox cycling of reactive oxygen species, the role of Zn(II) may be to inhibit this process, or to accelerate aggregation of neurotoxic oligomeric species into less toxic fibrils [104].

6.1.3 Variants

Two mutations on the same position have shown protective and pathogenic behavior, respectively. Replacing the alanine at position 2 with the polar and hydrophilic threonine, A2T, is associated with a lower risk of getting AD [105], while individuals with a homozygous A2V mutation, i.e. the more hydrophobic valine, has a higher risk [106], both highlighted in Figure 39. As they at the same time has proven to decrease and increase the formation of A β , they reinforce the amyloid hypothesis [107]. The aggregation kinetics of the two variants has been studied multiple times [105,107–112], and while a consensus seem to have established that A2T decrease β -secretase function and thereby A β production, contradicting conclusions has been drawn on the effect on aggregation kinetics. Early studies indicated that the lag times before

oligomerization (as indicated by an increase in ThT fluorescence signal) increased as $A2V < WT < A2T$ [107–109], except for one much earlier study that found instant aggregation of $A2T(1-40)$ [113]. A more recent study found that $A2V(1-42)$ had a significantly longer lag time, compared to both WT and A2T [110]. The difference compared to previous studies is explained by whether one is looking at secondary nucleation as the previous studies, or primary nucleation as the latter. They speculated that the early formed peptide dimer, which exists longer for A2V and has been suggested synaptotoxic, is part of the explanation as to why A2V is a causative mutation.

Another study looked at the effect on aggregation kinetics of adding sub stoichiometric amounts of Cu^{2+} to the three variants [111]. Without metal, they find the lag time increasing as $A2T < WT < A2V$, in contrast to the earlier studies on the matter. They also find that Cu^{2+} extends the lag time of all three variants, even at 0.05 equivalents Cu^{2+} added.

6.2 Coordination of Metals in $A\beta$

The coordination of copper and/or zinc has been studied multiple times using XAS with focus on the effect of peptide length [114], buffer [115,116], oxidation state [117–121], and mutagenesis [115,122], as well as in solid state [117]. However, no coordination studies have been performed on fibrillar $A\beta$ using XAS, only Raman spectroscopy [123] and EPR [124–127]. One exception may be an article on the coordination of Cu(II) and Cu(I) in $A\beta$ oligomers, but they only note an “onset of fibril formation” [128].

A list of experiments performed to investigate the coordination of copper and zinc in $A\beta$ can be seen in Table 10.

Table 10 – Previously performed structural determining experiments on copper and zinc with A β . 'f' indicates that fibrils were also studied.

Peptide length	Peptide conc	Metals investigated	Methods	Metal conc	Buffer	Ref
1-40	0.323 mM	Cu(II)	EPR	0.280 mM	PBS pH 7.4	[129]
1-28	?	Cu(II)	EPR	2:10, 3:10, ..., 10:10	PBS pH 6.9	[130]
1-42		Cu(II), Zn(II)	Raman			[123]
1-16	1.1 mM	Cu(II)	EPR	1 mM	–	[131]
1-28						
1-40	0.2 mM	Cu(II)	EPR	0.060 mM	Lyophilized at pH 7.4	[124]
1-28	0.05 mM	Cu(II)	EPR	0.01-0.25 mM	50 mM EM pH 5-10	[132]
1-16	0.1 mM	Cu(II)	EPR	0.09 mM	100 mM Tris, 150 mM NaCl, pH 7.4	[125]
1-28						
1-40+f						
1-42					50 mM NaPi, 75 mM NaCl, pH 7.2	
1-16	–	Cu(II)	EPR	0.25-2 equivalents	50 mM HEPES pH 7.4, 6, 9	[133]
1-28						
1-40	0.4 mM	Cu(II), Zn(II)	XAS	0.2, 0.4 and 0.8* mM	20-mM Tris/HCl buffer, pH=7	[134]
1-16	0.5-1 mM	Cu(II), Zn(II)	XAS	sub-stoichiometric	10 mM EM	[114]
1-28						
5-23						
17-40						
1-40						
1-16	2.2 mM	Cu(II)	XAS	1:1	PB (+NaCl) and PBS	[115]
1-42	0.85 mM					
6-14	Solid	Cu(I)	XAS	1:1	–	[117]
10-14						
1-16	–	Cu(I)/Cu(II)	XAS	–	Dried peptide into 50 mM NaPi, 75 mM NaCl, pH 7.2, with 50% glycerol (v/v)	[118]
1-40						
1-16	1.1 mM	Cu(II)	EPR	0.9 equiv	Milli-Q water	[135]
1-42	0.05 mM	Cu(II)	EPR	0.05 mM	10 mM phosphate, or 10 mM EM, or 10 mM HEPES, or Milli-Q. pH 5, 7.4, 9	[126]
1-16 and mut	1 mM	Cu(II)	EPR	1 mM	Milli-Q + NaOH / HCl pH 1.8-11.6	[136]

1-16	1.25 mM	Cu(II)	EPR	1.25 mM	100 mM EM pH 6.0 or 7.4	[137]
1-16 1-40f	0.1 mM	Cu(II)	EPR	0.1 mM	50 mM NaPi, 75 mM NaCl pH 7.2	[127]
3-16	2 mM	Cu(II)	XAS	2 mM	Milli-Q, pH adjusted by NaOH	[138]
11-28	1.2 mM	Zn(II)	XAS	0.5·[A β]	Milli-Q, pH adjusted by NaOH	[139]
1-16 and mods	1.0 mM	Zn(II)	XAS	0.9 mM	HEPES buffer 50 mM	[122]
1-7 1-28	1 mM	Cu(I)/Cu(II)	XAS	0.9 mM	10 mM dithionite in a HEPES buffer (0.1 M, pH 7.1) solution	[121]
1-42	1.0-2.0 mM	Cu(I)/Cu(II)	XAS	1:1	20 mM – 120 mM MOPS (+ 400 mM DTAB)	[116]

6.2.1 Coordination of Cu(II)

Despite the numerous studies of the coordination of copper in A β using XAS [114–121,134,138], EPR [124,125,136,137,126,127,129–133,135] and NMR [112,125,126,129,133,134], there is no clear consensus to be found. It has been highlighted that the coordination depends on whether amyloid- β is in a monomeric or oligomeric state and, depending on the solution conditions, which oligomeric state [116]. Even further, many different conformations seem to exist in the monomeric state [116].

6.2.1.1 XAS Studies

Previous studies using XAS has also reached different conclusions. First study was carried out on both Cu(II) and Zn(II), and studied both freshly prepared samples and samples incubated overnight that should favor aggregation [134]. However, they do not check for fibrils using ThT or other methods, and as copper has shown to inhibit fibrillization [97,102] it is likely that they are measuring oligomers that are different from fibrils. The copper coordination is identical across preparation procedure, and the best fit is achieved with a pentacoordinated model of three histidines, two at 1.94 Å and one at 1.85 Å, one tyrosine at 2.00 Å, and one oxygen ligand at 1.91 Å, as seen in Figure 42A. It was later pointed out that the short distance of 1.85 Å may have been due to photoreduction [116].

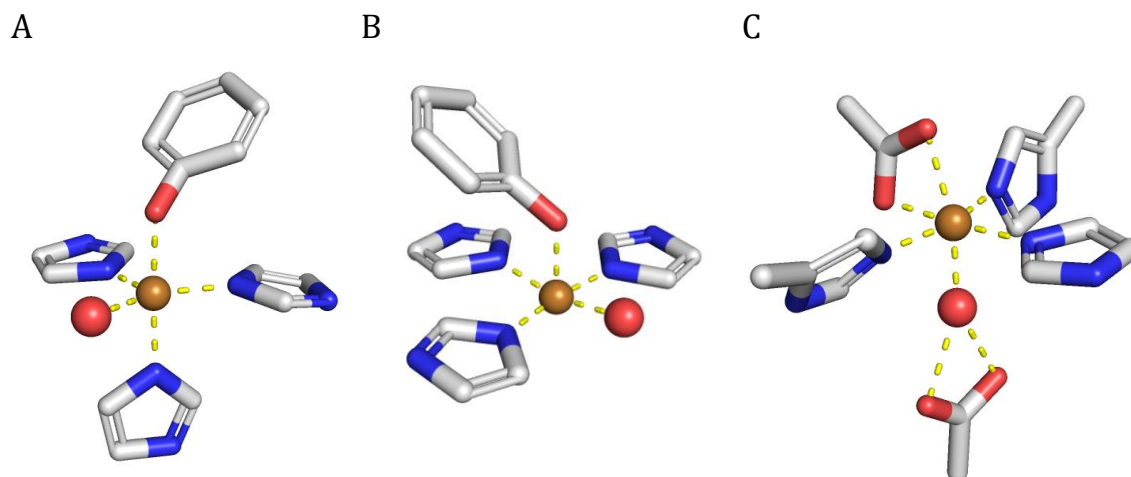


Figure 42 – Left: Pentacoordinated model suggested by Stellato *et al.* 2006 [134]. Middle: Square pyramidal coordination suggested by Minicozzi *et al.* 2008 [114]. Right: Octahedral coordination suggested by Streltsov *et al.* 2008 [115].

The next study, by the same group, focused on copper and zinc coordination to A β of various lengths, namely A β (1-16), A β (1-28), A β (5-23), and A β (17-40) [114]. A β (17-40) does not seem to bind Cu(II), in good agreement with the fact that all histidine groups are removed in this peptide. Comparing to the data from the previous publication, the EXAFS signal from A β (1-16) and A β (1-28) is identical to that of A β (1-40), while A β (5-23) is different. The best model to fit the data of the former three consists of three histidine groups at 1.95 Å, one tyrosine at 2.06 Å, and one oxygen at 1.95 Å, corresponding to a square pyramidal coordination, as seen in Figure 42B. It is noted that a model with an N-terminal nitrogen instead of the tyrosine only gives a marginally worse fit. The best model to fit the data of A β (5-23) consists of only two histidines, now at 1.99 Å, a tyrosine oxygen and an N-terminal nitrogen at the same distance, and an oxygen at 2.27 Å. Both of these studies were criticized for refining similar ligands at similar distances independently [116,118].

A study by Streltsov *et al.* 2008 measured EXAFS on A β (1-16) in various buffers, as well as A β (1-42)M35(O) in which Met35 is oxidized to methionine sulfoxide [115]. While they do not seem to find differences as an effect of the buffer, they do find a variation as a function of concentration of peptide. At high concentration ($[\text{Cu}^{2+}] = [\text{A}\beta] = 2.2 \text{ mM}$) they find three histidines coordinating at 1.91, 1.98 and 2.08 Å (an average of 1.99), two carboxylate oxygens from the same amino acid coordinating at 1.94 and 2.27 Å respectively, and an oxygen, allegedly from water, at 2.27 Å. The octahedral coordination is shown in Figure 42C. Having the distances as well as the angles of the three histidines refined independently gives a number of variables, N_{var} , of 16. Although the number of independent data points is calculated to be 111, my estimate is closer to 30 using optimistic values of $\Delta k = 12$ and $\Delta r = 4$ [26]. At lower concentration ($[\text{Cu}^{2+}] = [\text{A}\beta] = 1 \text{ mM}$), they find the three histidines at 1.94, 1.99 and 2.06 Å

respectively (an average of 2.00), while the other atoms in the model are found at the same distances within standard deviations.

The five- and six-coordinate models proposed by Stellato *et al.* and Streltsov *et al.* were both dismissed as ‘most likely incorrect’ in a paper by Shearer *et al.* 2008 with reference to a bond valence sum analysis [142,143] giving unrealistic values compared to a four-coordinate square planar model presented by themselves [118]. Their model suggests two histidines and another nitrogen or oxygen ligand at 1.94 Å as well as a nitrogen or oxygen ligand at 2.07 Å, see Figure 43A. A later study by the same authors and others investigated the coordination of Cu(II) and Cu(I) in A β (1-42) oligomers at pH 7.2 [128]. As noted previously, an onset of fibril formation was observed. The best model to fit the EXAFS for Cu(II) was a four-coordinate square-planar, now with three histidines and one nitrogen or oxygen ligand (Figure 43B). Two histidines were found at 1.96 Å and a third at 2.03 Å. The nitrogen or oxygen ligand was found at 1.94 Å. Attempting to fit only two histidines and two nitrogen or oxygen ligands led to a worse fit, and was ruled out as a possible solution.

A five-coordinate model was resurrected by Hureau *et al.* 2009 when they collected XAS on A β (1-16) at pH 6.6 and 8.7 [120]. At low pH, they find three nitrogen ligands at 1.98 Å, one oxygen ligand at 1.96 Å, and one oxygen ligand at 2.46 Å, corresponding to a square planar pyramidal geometry, where the oxygen at 2.46 Å is the axial ligand, and the remaining four ligands make up the equatorial square (Figure 43C). As this study does not include multiple scattering effect, no information except from NMR and CD is given on the number of histidines participating.

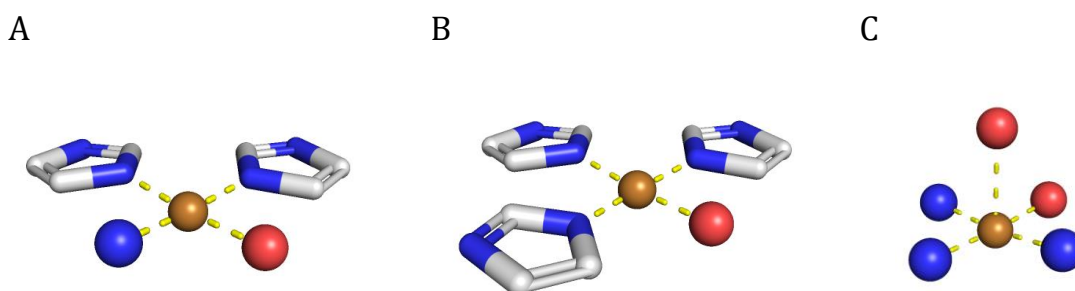


Figure 43 – Left: Square planar coordination suggested by Shearer *et al.* 2008 [118]. Middle: Square planar coordination with three histidines, suggested by Shearer *et al.* 2010 [128]. Right: Square planar pyramidal coordination suggested by Hureau *et al.* 2009 [120].

The latest study on Cu(II)A β was published earlier this year (2019) [116]. After having measured the effect of photoreduction and concluded that photoreduced CuA β is neither representative of Cu(II)A β nor Cu(I)A β , they collect XAS including high energy resolution fluorescence detected XAS on Cu(II)A β (1-42) at pH 6.1, 7.4, and 9.0. Their best fit to the EXAFS is achieved

with one histidine and three nitrogen or oxygen ligands at pH 6.1, two histidines and two nitrogen or oxygen ligands at pH 7.4, and finally, two histidines and three nitrogen or oxygen ligands at pH 9.0. All three models are depicted in Figure 44. At pH 6.1, all four ligands are grouped at the same distance of 1.981 Å. At pH 7.4, the histidines are found at 1.981 Å as well, while the other ligands are found at 2.000 Å. Lastly, at pH 9.0, all five ligands are found at the same distance of 1.967 Å. The authors note that the number of histidines is subject to some uncertainty, and a single histidine at pH 9.0 cannot be ruled out.

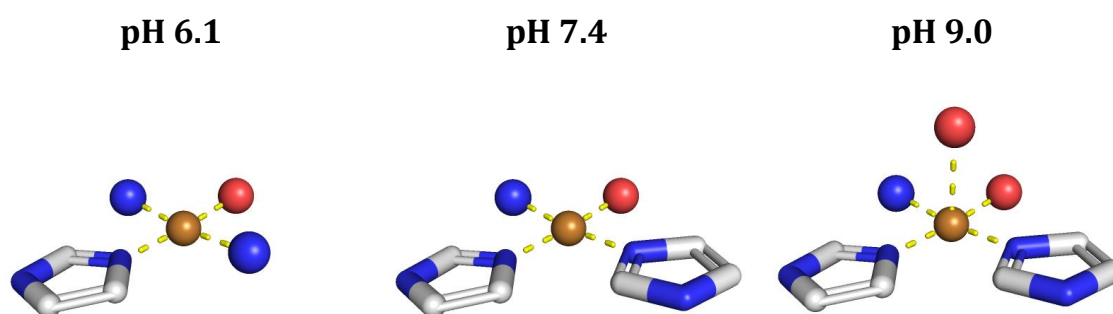


Figure 44 - Models of the average Cu(II) coordination in A β (1-42) at pH 6.1, 7.4, and 9.0 suggested by Summers et al. 2019 [116]. Note that the nature of the all red and blue spheres can be either nitrogen or oxygen.

6.2.1.2 Fibrillar Studies

The highest resolution structure of A β fibrils released is the previously mentioned cryo-EM structure [95], which could give a hint towards a possible coordination environment for Cu(II). However, the β -sheet layers are about 5 Å apart, which would cause the Cu(II) atoms to also be about 5 Å apart, which again would give rise to peak broadening in EPR [144] that is not observed.

As no change in the NMR signal for the β -strand is observed with presence of Cu(II) [145], His13 and His14 appear unable to coordinate to Cu(II) simultaneously. This is in contrast to the previous solution studies that suggested all three histidines participated in the liganding [115,128,147-149,130-134,140,141,146] unless the coordinations in solution and fibrils are not the same.

Some of the studies mentioned in Table 10 have looked specifically at the coordination in fibrils. An overview of their suggested geometries can be seen in Table 11.

Table 11 – Studies of Cu(II) binding in A β fibrils.

Methods	Peptide conc	Metal conc	Buffer	Suggested Geometry	Ref	Year
Raman	-	-	Isolated from senile plaque	Histidine ligand, no tyrosine ligand, no amide ligand	[123]	2003
EPR	0.2 mM	0.06 mM	Lyophilized at pH 7.4	3 His 1 Tyr	[124]	2004
EPR	0.1 mM	0.09 mM	100 mM Tris, 150 mM NaCl, pH 7.4 or 50 mM NaPi, 75 mM NaCl, pH 7.2	3N10 and nearly identical to soluble A β 2 His, 1 amide-N, 1 carbonyl-O	[125]	2005
EPR	0.05 mM	0.05 mM	10 mM phosphate, or 10 mM EM, or 10 mM HEPES, or Milli-Q. pH 5, 7.4, 9	Low pH: 2N2O or 3N10 High pH: 3N10 or 4N	[126]	2009
EPR	0.1 mM	0.1 mM	50 mM NaPi, 75 mM NaCl pH 7.2	Two histidines	[127]	2012

Raman spectroscopy has shown signals characteristic of histidine binding, that tyrosine is not the source of the oxygen ligand, and that an amide is not coordinating either [123]. EPR measurements have shown that Cu(II) is not reduced to Cu(I) in fibrils, that water is not in its coordination sphere, and confirmed that tyrosine does not coordinate Cu²⁺ in fibrils [125]. A 3N10 coordination is suggested, and it appears as if the coordination in fibrils and solution are the same. A later EPR study found the same result [127]. However, both due to the Jahn-Teller effect and the fact that they are binding through orbitals orthogonal to the one that contain the unpaired electron that EPR is scanning, axial ligands are extremely difficult to resolve, and it may not be possible to distinguish between 0, 1 and 2 axial ligands using EPR.

Sarrel *et al.* 2009 also makes this a point, and suggests that one histidine as well as another oxygen are the axial ligands in an octahedral coordination, as seen in Figure 45 [126].

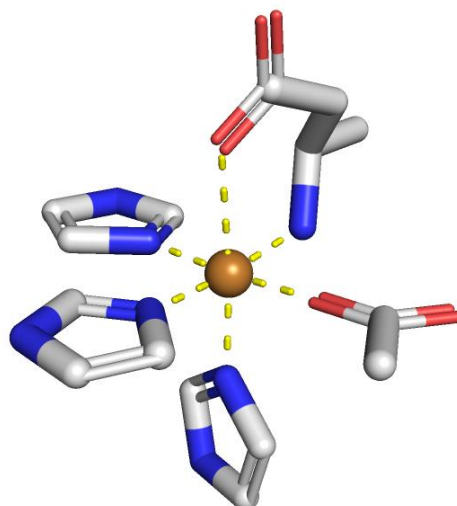


Figure 45 – Octahedral coordination suggested by Sarell et al. 2009 [126].

6.2.2 Coordination of Zn(II)

While Zn²⁺ has been found to coordinate in a tetrahedral, square-planar pyramidal and octahedral geometry in biological systems, the tetrahedral is the most common and lowest-energy ground-state coordination [150].

Unlike Cu(II), Zn(II) has no unpaired electrons, and is thus EPR-silent. Its coordination has therefore been studied mainly by Raman spectroscopy [146], NMR [104,122,130,139,151–153], and XAS [114,122,134,139]. NMR spectroscopy has been used either to compare spectra of WT and variants with certain single residue mutations, or to do titration of Zn²⁺.

¹H-NMR titration data gives information on what residues in A β are affected by the addition of Zn²⁺, which would then be interpreted, depending on how much each residue is affected, as being involved in Zn²⁺ coordination. His6, His13 and His14 has been found to be strongly affected, while Asp7, Ser8, Tyr10 and Val12 are also affected [104]. Others have found Glu11 to be part of the tetrahedral coordination involving the three histidines [151]. ¹H-¹³C HSQC experiments have concluded that Tyr10 is close to the binding site, but not directly involved, which instead the N-terminal of Asp1 is [152]. A more recent study suggest multiple sites in equilibrium, with a maximum of two histidines coordinating simultaneously, Glu11 always participating, and Asp1, Glu3 and Asp7 competing as the fourth ligand, still in a tetrahedral coordination [122]. Such a coordination is also found in the crystal structures of *Deinococcus radiodurans* Dps protein (DR2263) [154] (PDB ID: 2C2U) and cockroach allergen *Bla g 2* [155] (PDB ID: 1YG9), the latter presented in Figure 46. Notice how a tyrosine is stabilizing one histidine through a π -interaction, which could also be the case in A β , as tyrosine (as mentioned above) has been shown to be indirectly involved in the coordination.

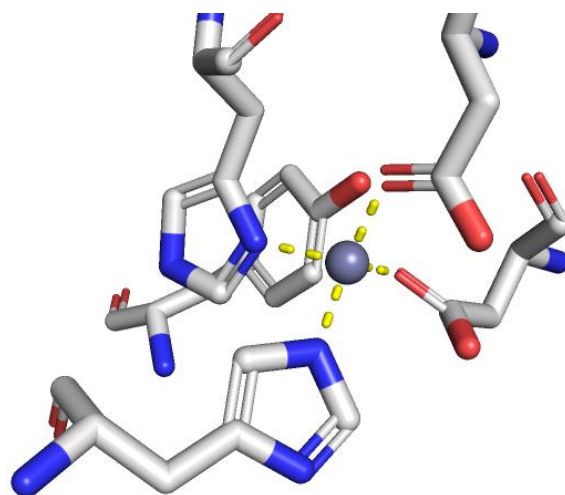


Figure 46 – Coordination of Zn^{2+} in the crystal structure of cockroach allergen *Bla g 2* (PDB ID: 1YG9).

XAS studies of the Zn^{2+} coordination has also given various answers, with some trying to fit multiple shells of atoms, finding four histidines and one oxygen ligand, but these data may have been affected by the buffer [114]. Others have restrained to only fitting the first shell [122] or only doing qualitative analysis of the XANES region [139], giving little information on the residues coordinating.

6.3 Experimental

Three peptides were used in this study, all being the 1-40 peptide. WT (DAEFRHDSGYEVHHQKLVFFAEDVGSNKGAIIGLMVGGVV), A2T (DTEFRHDSGYEVHHQKLVFFAEDVGSNKGAIIGLMVGGVV), and A2V (DVEFRHDSGYEVHHQKLVFFAEDVGSNKGAIIGLMVGGVV) were all purchased from *CASLO ApS*, and the purity was above 98% as checked by the company using HPLC.

6.3.1 Sample Preparation

Monomeric solutions were prepared as described by Somavarapu *et al.* [111] by weighing 1.6-1.9 mg of $A\beta$ -WT, $A\beta$ -A2T and $A\beta$ -A2V, adding 1.6 ml HFIP, leaving for 1 hour, evaporating with argon stream, adding 1.6 ml more, and evaporating under argon stream, creating a peptide film in the tube. 1.6 ml 10 mM NaOH was added, and the solutions were sonicated for 6 minutes in an icebath and centrifugated for 30 minutes at 4° C, 18000 G. Three times 450 μ l were taken from the mother liquor and 1.8 ml (2 ml for $ZnA\beta$ samples) 5 mM HEPES buffer at pH 7, 8 or 9 was added, and the solution was filtered through a 0.22 μ m filter. The pH was measured directly in the solutions, which were kept on ice to avoid premature aggregation, and adjusted with NaOH/HCl (pH was not adjusted for $ZnA\beta$ samples). 140 μ l 0.12 mM ThT solution in the same HEPES buffer was added, and 1360 μ l from the final solution was mixed with 5.98 μ l 5 mM $CuCl_2$ solution to give a total of 9 samples. For $ZnA\beta$ samples, 900

μl of the peptide in buffer solution was mixed with 100 μl ThT solution and 4 μl ZnCl_2 solution.

6.3.2 ThT Fluorescence

Corning 96 Well fluorescence plates were purchased from *Sigma-Aldrich* (CLS3881). 100 μl of $\text{Cu(II)A}\beta$ solution or $\text{Zn(II)A}\beta$ solution was added to each well, with 10 and 5 replicates, respectively. Each well was sealed immediately after being filled. The plate was loaded into an *OPTIMA FLUOstar* microplate reader from *BMG LABTECH*, and an experiment was setup at 37°C with 10 flashes per well with an excitation at 440 nm and emission at 490 nm, corresponding to the signal from Thioflavin T, and a gain of 1500. The plate was read every 5 minutes with 3 seconds of double orbital shaking before measuring. For $\text{Cu(II)A}\beta$, two experiments, #1 and #2, were conducted on two separate dates. Unused solution was stored at room temperature.

6.3.3 XAS Data Collection, $\text{Zn(II)A}\beta$

Shaken $\text{Zn(II)A}\beta$ samples were prepared by pooling the content from 5 wells into a tube and centrifuging for 30 minutes at 20° C 18,000x G, then pipetting off the supernatant. The tubes were then sealed and stored in liquid nitrogen. XAS samples were prepared by thawing the samples, adding glycerol to a content of 10-20%, and injecting into custom made samples holders sealed with ordinary office tape.

Non-shaken samples were stored at room temperature since preparation, and were spun down for 1-3 minutes at 13200 rpm on an *Eppendorf* Centrifuge 5415 R. The precipitate was mixed directly with glycerol to a content of 10-20%. Samples at pH 9 had no precipitate, and were prepared by adding the supernatant to a 3 kDa cut off spin filter and spinning for 90 min at RT.

XAS experiments were conducted at the SAMBA beamline at the SOLEIL Synchrotron Facility in St. Aubin, France. Data was collected on non-shaken samples of all three variants, at pH 7, 8 and 9, and shaken samples of all three variants at pH 7, 8, and 9, except $(\text{Zn-WT})_7$, which was lost.

Both XANES and EXAFS were collected in step scan mode. For XANES, 9550 eV to 9650 eV was collected every 5 eV, 9650 eV to 9652 eV collected every 1 eV, and 9652 eV to 9710 eV collected at the resolution maximum, every 0.4 eV. Beyond 9710 eV, data was collected with gradually increasing increments, from $k = 3$ to $k = 13$ ($k = 14$ for non-shaken pH 7 samples) to a total exposure of 30 minutes for each spectrum. Each sample had at least five spectra collected at different spots.

6.3.4 XAS Data Collection, Cu(II)A β

Shaken Cu(II)A β samples were prepared by pooling the content from 10 wells into a tube and centrifuging for 30 minutes at 20° C 18,000x G, then pipetting off the supernatant and injecting the remainder into custom made sample holders sealed by Kapton foil, and storing in liquid nitrogen until data collection.

Data was collected at the BM30B FAME beamline at ESRF. Eleven samples were measured: All three variants at pH 7, 8 and 9 from the ThT plate of Experiment #2, as well as freshly mixed WT at pH 6 and 10. (Cu-WT)₇ is from Experiment #1, and (Cu-A2V)₉ was sampled from the unused solution stored at room temperature, and was thus not a part of any of the ThT experiments.

All measurements were carried out in a liquid helium cryostat at 4 K to avoid photoreduction. Samples were measured 9 times at different points from 8930 eV to 9720 eV with various step sizes, with a total exposure of 30 minutes at each point.

6.3.5 EXAFS Refinements

Structural models were refined as to fit the EXAFS data using *Excurve*. Input models were built from scratch or with basis in the Cu²⁺ center of superoxide dismutase structure (PDB ID: 2SOD) [156] using *PyMOL* [157] and starting values of distances, Debye-Waller factors, angles and E_f were chosen iteratively. Multiple scattering signals were only considered inside each unit, i.e. no signal from more than one amino acid.

The Debye-Waller factor was limited as $0.001 \leq \sigma^2 \leq 0.020 \text{ \AA}^2$, which is a slightly broader range than argued realistic by others [116]. All multiple scattering paths including 3 or less different atoms, with a total path length of 10 Å or less were included. The default value of the amplitude reduction factor of 1.0 was used, as no model compound was available to calculate it accurately. The occupation number for each shell was kept constant at 1. Fourier transform plots are phase corrected by the first shell, which in all cases is N δ of the closest histidine in the input model.

Two angles, α and β , were considered in the refinements, as presented in Figure 47. The angle of the histidines has a big influence on the multiple scattering signal, and whether certain combination of angles might result in a negative interference pattern that gives the same signal as an amide (i.e. no ring) is not clear. The angles were included in some refinements, if they resulted in a substantial improvement of the fit.

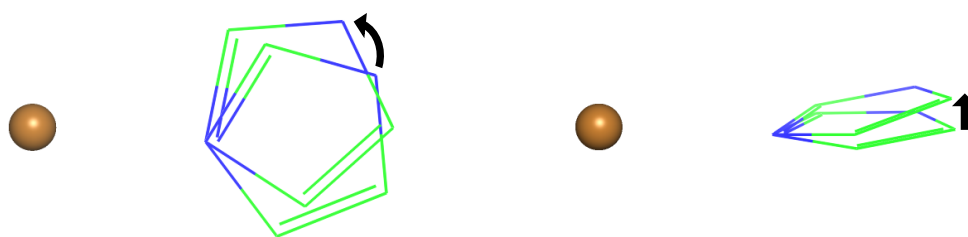


Figure 47 – Imidazole changing Left: 0° to 20° in the α angle, also known as the twist or φ angle. Right: 0° to 10° in the β -angle, also known as the tilt or θ angle.

6.4 Results and Discussion

6.4.1 ThT Fluorescence CuA β

All repetitions of all copper samples except (Cu-WT)₇, (Cu-A2T)₉ and (Cu-A2V)₉ achieved converged signals expected for fibrillar formation within 50 hours. The raw spectra can be found in Appendix A. Spectra were normalized to highest value of each spectrum, and averaged after outliers were removed, with at least five repetitions kept for all samples, except for (Cu-WT)₇ in experiment #1, which is based on four repetitions. Averages and standard deviations is presented in Figure 48. The averaged lag times for all samples can be seen in Table 12.

Table 12 – Lag times for the two ThT fluorescence experiments, conducted days apart. Uncertainty is reported as one standard deviation.

Experiment #1			Experiment #2		
Sample	Lag time	$\pm 1\sigma$	Sample	Lag time	$\pm 1\sigma$
(Cu-WT) ₇	31 h	± 7 h	(Cu-WT) ₇	13 h	± 6 h
(Cu-A2T) ₇	14 h	± 1 h	(Cu-A2T) ₇	10 h	± 1 h
(Cu-A2V) ₇	17 h	± 4 h	(Cu-A2V) ₇	19 h	± 4 h
(Cu-WT) ₈	18 h	± 3 h	(Cu-WT) ₈	17 h	± 4 h
(Cu-A2T) ₈	15 h	± 4 h	(Cu-A2T) ₈	10 h	± 2 h
(Cu-A2V) ₈	34 h	± 3 h	(Cu-A2V) ₈	25 h	± 5 h
(Cu-WT) ₉	18 h	± 2 h	(Cu-WT) ₉	14 h	± 2 h
(Cu-A2T) ₉	14 h	± 3 h	(Cu-A2T) ₉	13 h	± 2 h
(Cu-A2V) ₉	30 h	± 4 h	(Cu-A2V) ₉	26 h	± 4 h

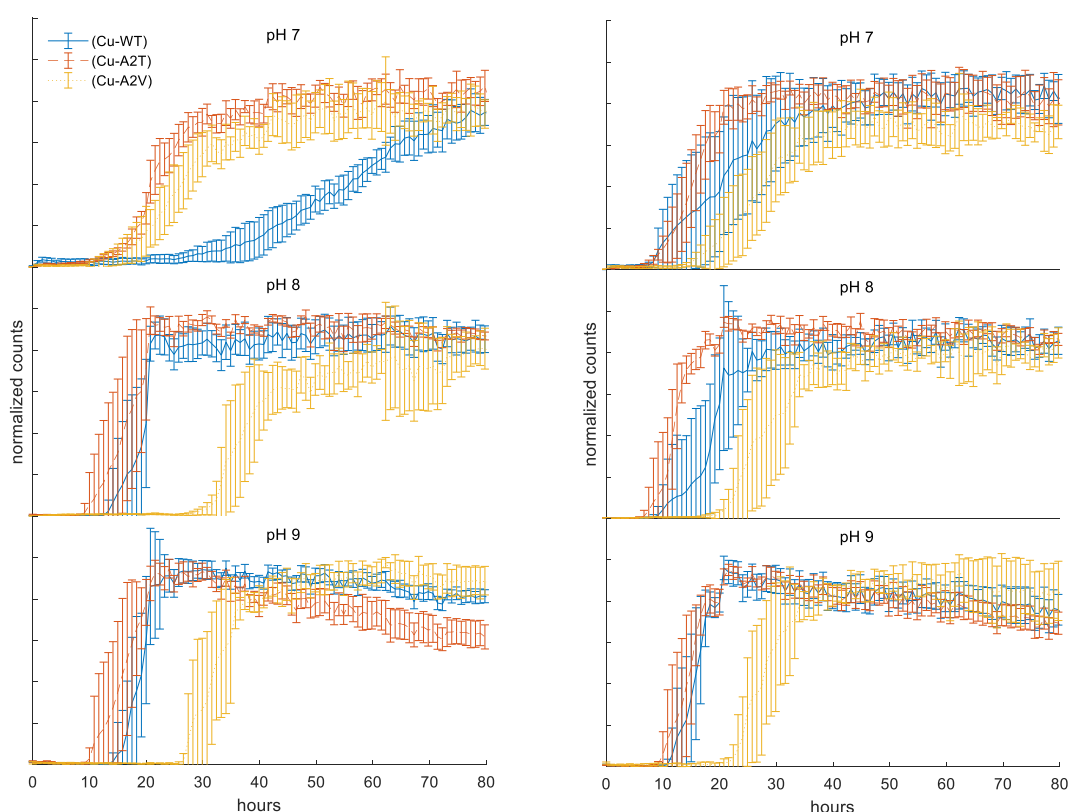


Figure 48 – Average of normalized ThT fluorescence signal counts as a function of time with error bars corresponding to 1σ .

Across all three pH values, the lag times increase as A2T < WT < A2V, agreeing with recent studies [110,111] while contradicting others [107–109]. A

tendency towards lag time increasing with pH can also be observed. (Cu-WT)₇ is an exception to both of these, perhaps because of a problem with the top row of the plates while being read.

6.4.2 ThT Fluorescence ZnA β

All raw spectra can be found in Appendix A. At pH 9, no sample aggregated within the 130 hours of the experiment. For the samples at pH 7 and 8, all samples had achieved converged signals within 60 hours. Spectra were normalized to highest value of each spectrum, and averaged after outliers were removed, with at least five repetitions kept for all samples. Averages and standard deviations is presented in Figure 49. The averaged lag times for the samples with converged signals can be seen in Table 13.

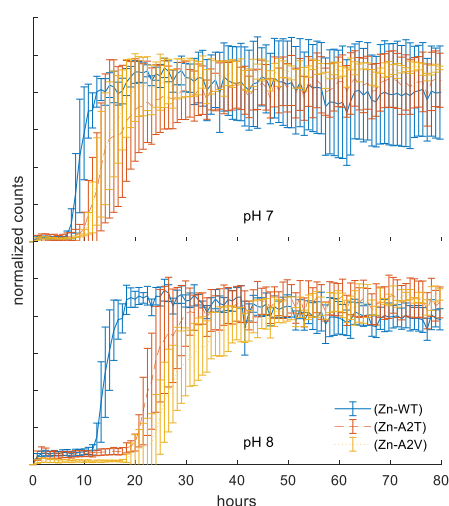


Figure 49 - Average of normalized ThT fluorescence signal counts as a function of time with error bars corresponding to 1σ .

Table 13 – Lag times for the ThT fluorescence experiment performed on ZnA β . Uncertainty is reported as one standard deviation.

Sample	Lag time	$\pm 1\sigma$
(Zn-WT) ₇	8 h	± 1 h
(Zn-A2T) ₇	12 h	± 3 h
(Zn-A2V) ₇	11 h	± 2 h
(Zn-WT) ₈	9 h	± 4 h
(Zn-A2T) ₈	10 h	± 6 h
(Zn-A2V) ₈	23 h	± 3 h

At pH 7, the lag times of ZnA β is in the order of WT < A2V \approx A2T, while at pH 8, they are in the order of WT < A2T < A2V. Previous ThT fluorescence studies of the effect of Zn²⁺ on the aggregation kinetics of A β has concluded unambiguously that Zn²⁺ prevents the formation of fibrils, and instead almost instant forms non-fibrillar aggregates [102,103,158–161]. These studies focus on the relative decrease in fluorescence intensity compared to metal free A β , and do not report lag times. As the current study did not measure metal free A β , it is not possible to see if a comparable relative decrease in fluorescence intensity is observed. One hypothesis for this discrepancy could be that the formation of ZnO, which is discussed later, prevented Zn²⁺ from inhibiting fibril formation. ZnO is not formed at higher pH, which is why no fibrillization is seen here.

6.4.3 Copper XAS

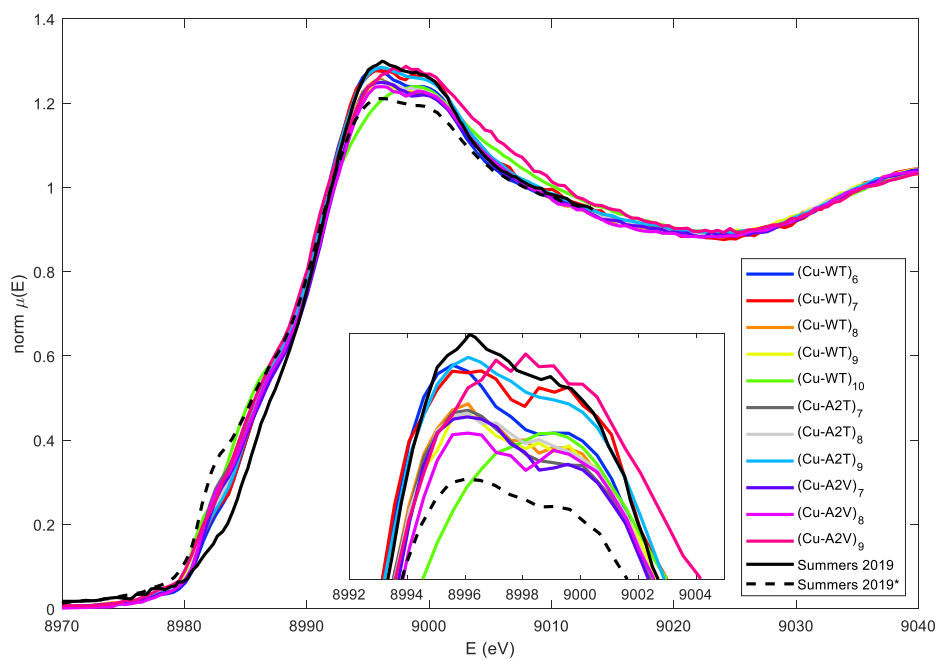
In Figure 50A, the XANES of all samples are plotted, alongside previously measured data [116] on Cu(II)A β and photoreduced CuA β . From Figure 50B it can be seen that the current data has a high degree of photoreduction, as the edge has an increase at around 8984 eV and decrease around 8997 eV corresponding to a shift in energy for the Cu(I) 1s \rightarrow 4p transition [15].

(Cu-WT)₆, (Cu-WT)₁₀ and (Cu-A2V)₉ appear different from the rest, the latter two with a single peak whiteline. While none of these are measured fibrils, the high pH samples may represent the copper site with a higher coordination number found by Summers *et al.* [116]. While A2T is supposed to have the lowest pK_a for this transition [111], (Cu-A2T)₉ appears only slightly different from (Cu-A2T)₈ and (Cu-A2T)₇. This could indicate that the change in coordination as a function of pH is different, or non-existing, for fibrillar CuA β . Meanwhile, (Cu-WT)₆ may represent a low pH structure.

An analysis of the EXAFS may give more detailed information on the coordination, the distances, and the nature of surrounding ligands. Figure 51 shows the k^3 -weighted $\chi(k)$ for all CuA β samples. The quality of the data is very different, and while some signals have low noise all the way to $k = 12 \text{ \AA}^{-1}$, some already become noisy at around $k = 10 \text{ \AA}^{-1}$. The first variation between the signals can be seen at around $k = 4.8 \text{ \AA}^{-1}$, where the peak appear lower for A2V pH 7 and WT pH 8. Another variation is the height of the shoulder peak at $k = 5.9 \text{ \AA}^{-1}$, which appear weak for the A2V samples, while more pronounced for the A2T and WT, especially at pH 8. Only seven samples were used for EXAFS refinements, as the rest were too noisy due to low concentration of the sample.

In Figure 52, the FT of the k^3 -weighted $\chi(k)$ signals can be seen and compared. Looking at the main peak at 2 \AA and the multiple scattering peaks at 3 \AA , it would appear as if (Cu-A2T)₉ is similar to both (Cu-A2V)_x samples, while (Cu-WT)₉ is similar to (Cu-A2T)₇, and (Cu-WT)₈ and (Cu-A2T)₈ are similar. Comparing the multiple scattering peaks at 4 \AA , one big peak can be seen for the two pH 7 samples, a small and a big peak for the three pH 8 samples, while at pH 9, (Cu-WT)₉ looks similar to (Cu-WT)₈ and (Cu-A2T)₉ looks similar to (Cu-A2T)₇.

A



B

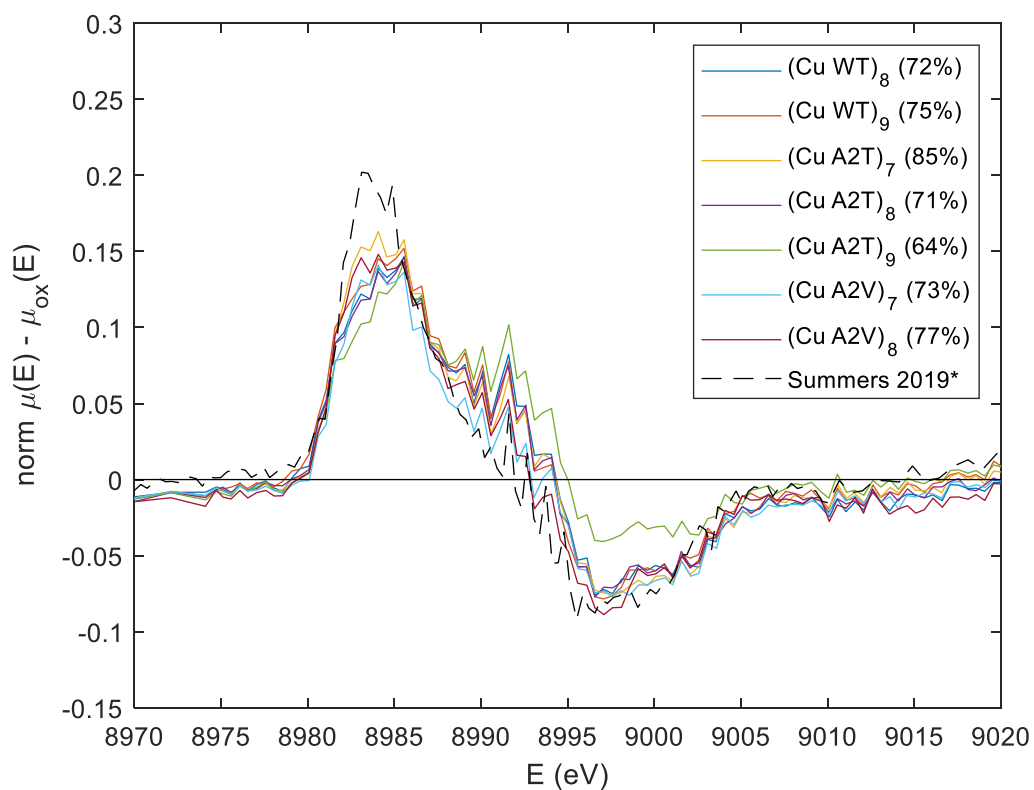


Figure 50 – Top: Copper XANES of WT, A2T and A2V A β at various pH compared with photoreduced CuA β (dashed black) and Cu(II)A β (solid black) from [116]. Inset: magnification of whiteline. Bottom: Calculation of Cu(I) content based on the difference spectrum between Cu(II)A β and photoreduced CuA β data from [116].

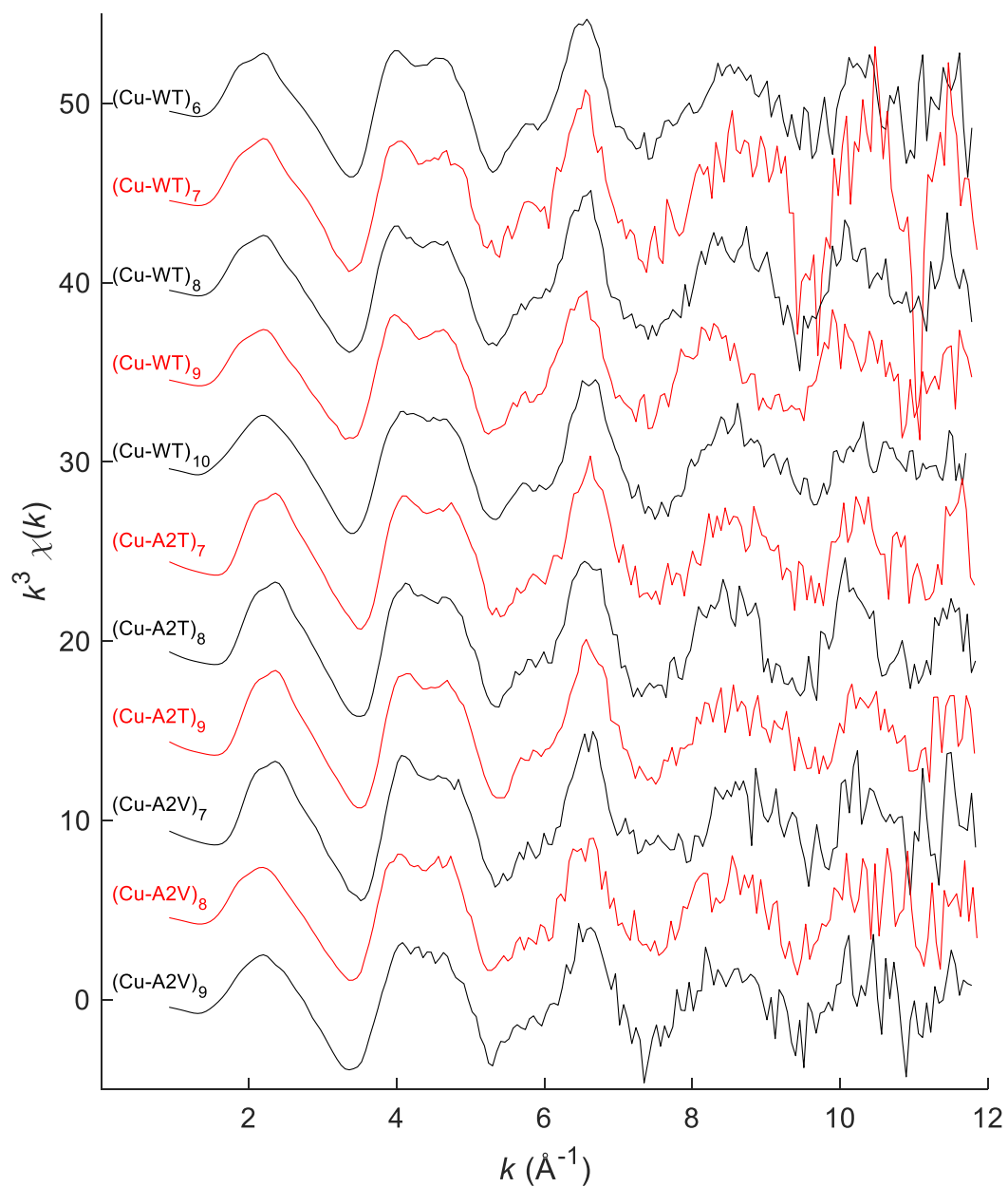


Figure 51 – k^3 -weighted EXAFS functions for all CuA β samples. Each spectrum is shifted 5 units in the vertical direction.

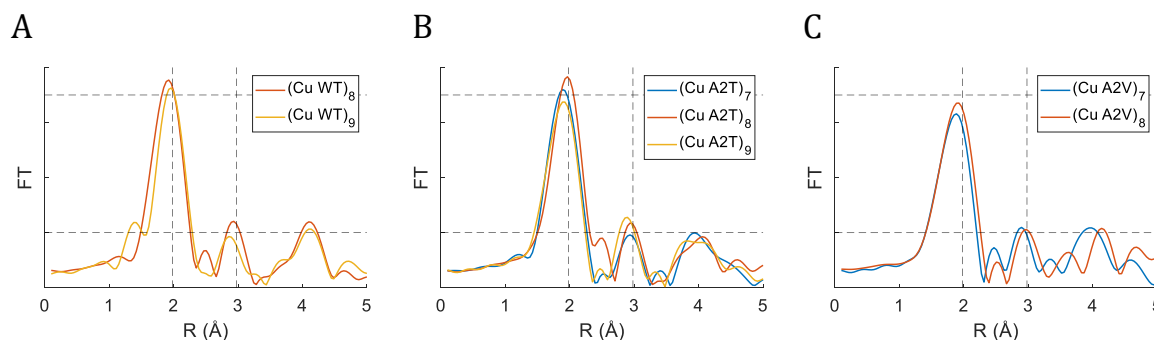


Figure 52 – FT of k^3 -weighted $\chi(k)$ (solid lines). Vertical dashed lines at put at 1.98 and 2.98 to assist in comparison, as are two horizontal dashed lines.

Multiple input structures were attempted refined against all datasets, inspired by the coordinations suggested by others, as seen in Table 10. The input models varies mainly on the number of histidines and the number of neighboring atoms to nitrogen or oxygen ligands. The models that gave the best fit to the data can be seen in Figure 53, and their parameters in Table 14. Notice that while it is commonly impossible to tell similar backscatters at distances less than 0.13 \AA apart for $k = 12 \text{ \AA}^{-1}$ data, histidines have such strong multiple scattering signals from the imidazole ring that enable them to be distinguished from other backscatters, even at similar distances [116].

Many models were found to give reasonable fits, so to decide on the best model was a difficult task. All model parameters and fits can be found in Appendix B. The best models were chosen based on which gave the best fit to both the $\chi(k)$ and the FT of it, while having the most chemically sensible parameters. In some cases, no model was found with all parameters being chemically reasonable, but the best one is still presented. The actual coordination may very well be a mixture of several of these.

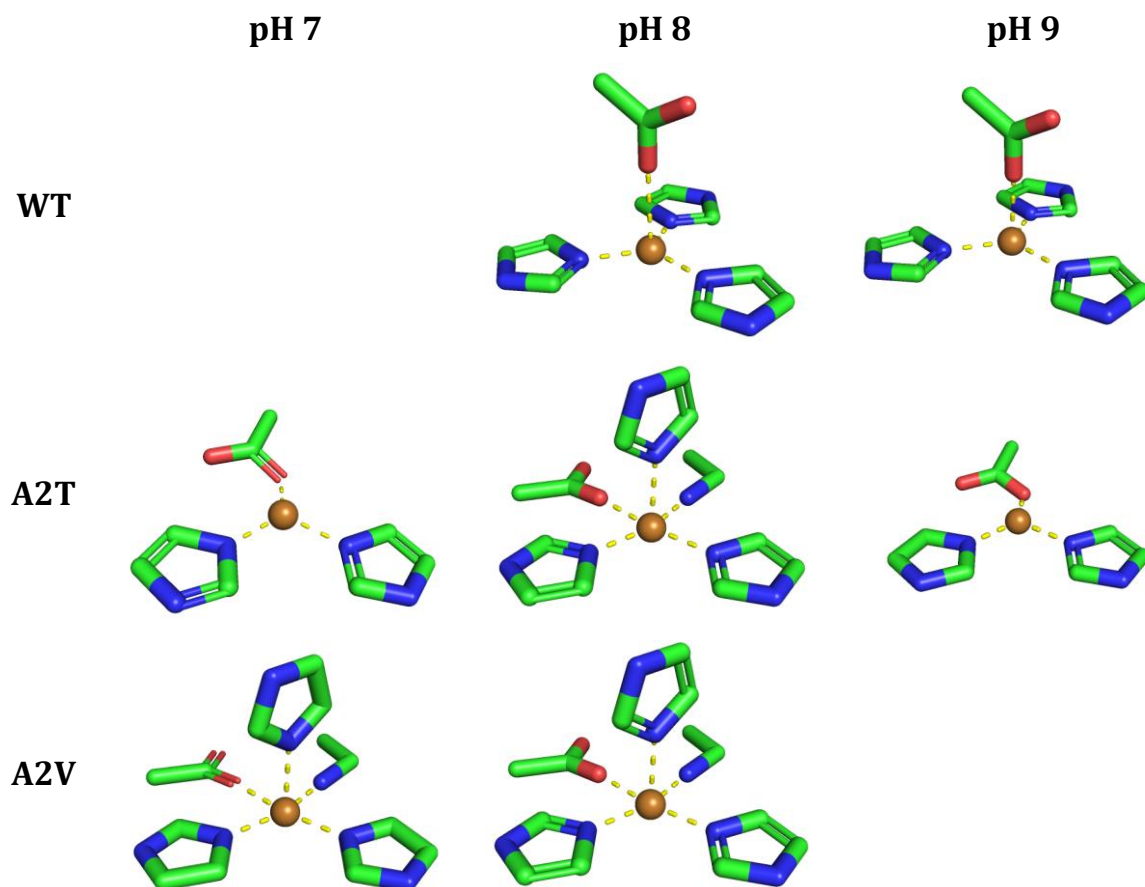


Figure 53 – Suggested models of coordination for all three $A\beta$ variants at three pH values. All shown atoms were included in the refinements.

Table 14 – Parameters for the best fits for CuA β . N is the shell occupation number, R is the shell distance, σ_{DW} is the Debye-Waller factor, E_f is the Fermi energy, R_{EXAFS} is the quality of fit. σ is a statistical standard deviation, calculated from the correlation coefficients.

Ligand	N	$R \pm 2\sigma$ (Å)	$\sigma_{DW}^2 \pm 2\sigma$ (Å ²)	ΔE_f (eV)	R_{EXAFS}
(Cu-WT) ₈					
His	3	1.975 \pm 0.007	0.005 \pm 0.001	-10.8	31%
O _{δ1} (Glu)	1	2.68 \pm 0.02	0.003 \pm 0.003		
(Cu-WT) ₉					
His	3	2.014 \pm 0.007	0.004 \pm 0.001	-11.7	29%
O	1	2.32 \pm 0.04	0.014 \pm 0.007		
(Cu-A2T) ₇					
His	2	1.98 \pm 0.02	0.007 \pm 0.003	-8.7	32%
O _{δ1} (Glu)	1	1.95 \pm 0.01	0.005 \pm 0.003		
(Cu-A2T) ₈					
His	2	1.993 \pm 0.008	0.008 \pm 0.001	-12.1	30%
N (Asp1)	1	1.993 \pm 0.008	0.008 \pm 0.001		
O _{δ1} (Glu)	1	1.993 \pm 0.008	0.008 \pm 0.001		
His	1	2.33 \pm 0.01	0.001 \pm 0.002		
(Cu-A2T) ₉					
His	2	1.94 \pm 0.02	0.004 \pm 0.003	-11.4	31%
O _{δ1} (Glu)	1	2.02 \pm 0.02	0.004 \pm 0.004		
(Cu-A2V) ₇					
His	2	1.97 \pm 0.01	0.007 \pm 0.001	-9	41%
N (Asp1)	1	1.97 \pm 0.01	0.007 \pm 0.001		
O _{δ1} (Glu)	1	1.97 \pm 0.01	0.007 \pm 0.001		
His	1	2.25 \pm 0.03	0.008 \pm 0.008		
(Cu-A2V) ₈					
His	2	1.97 \pm 0.01	0.008 \pm 0.001	-9	39%
N (Asp1)	1	1.97 \pm 0.01	0.008 \pm 0.001		
O _{δ1} (Glu)	1	1.97 \pm 0.01	0.008 \pm 0.001		
His	1	2.22 \pm 0.03	0.008 \pm 0.006		

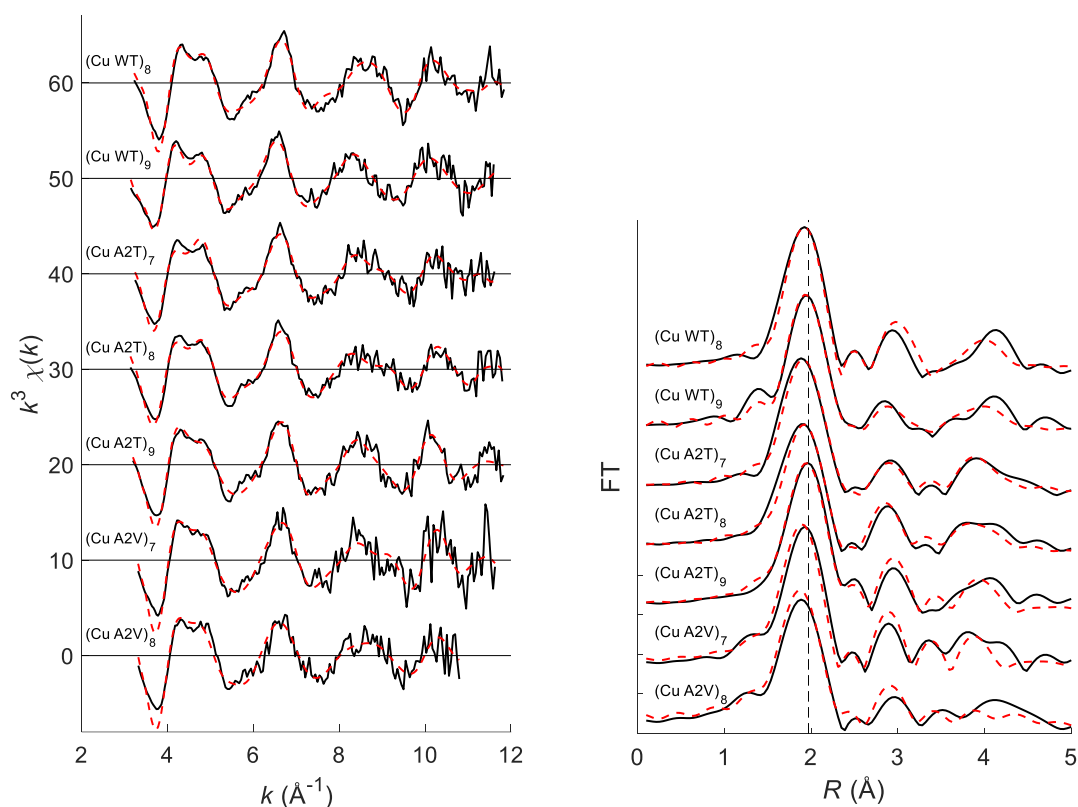


Figure 54 – Left: k^3 -weighted $\chi(k)$ data (solid) and fit (dashed). Each dataset is shifted 10 units in the vertical direction. Right: FT of the same, shifted 15 units in the vertical direction. Black vertical dashed line is at 1.97 \AA .

The first point is the coordination number. (Cu-A2T)₇ and (Cu-A2T)₉ were best fitted with a three-coordinate structure, (Cu-WT)₈ and (Cu-WT)₉ were found to have a four-coordinate structure, while (Cu-A2T)₈, (Cu-A2V)₈, and (Cu-A2V)₉ were found to be five-coordinated. While Cu(II) prefers a square planar coordination, perhaps a (bi-)pyramidal with one or two extra axial ligand further away due to Jahn-Teller distortion, Cu(I) prefers a linear coordination. However, perhaps due to the data collection happening at very low temperatures, photoreduced CuA β have previously shown a three-coordinate trigonal planar structure [116]. This may be the case for (Cu-WT)₈, (Cu-WT)₉, (Cu-A2T)₇ and (Cu-A2T)₉, which all have three ligands at 1.94-2.02, and a fourth at 2.3 \AA , 2.7 \AA or 3.2 \AA . However, although the Cu(I) content calculated in Figure 50B is about the same for all samples (at least, these are not lower than the rest), a square pyramidal geometry was found to be the best fit for (Cu-A2T)₈, (Cu-A2V)₈, and (Cu-A2V)₉. The four equatorial ligands were two histidines, an N-terminal nitrogen and a carboxylate oxygen, with the third histidine coordinating the axial position, see Figure 55. Such a model agrees with the EPR data that finds a 3N1O coordination in fibrillar A β [125–127], as the axial ligand is invisible to the technique. The model is the same as proposed by Sarell *et al.* 2009 [126], who also argues that due to the fact that Cu(II) affinity is the same in monomers and fibrils, the role of His13 and His14 should

be the same, and that this part may not be part of a β -strand, as also suggested by others [91,162].

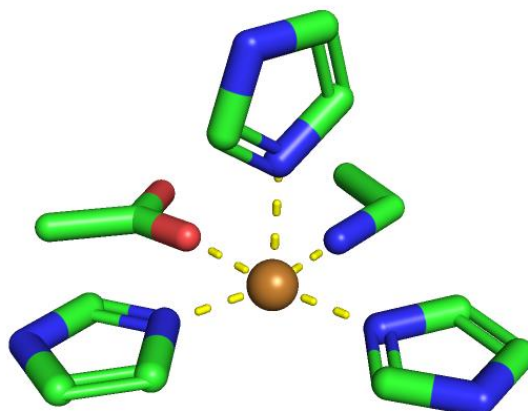


Figure 55 – Best fit model to the $(\text{Cu-A2T})_8$, $(\text{Cu-A2V})_8$, and $(\text{Cu-A2V})_9$ datasets. All atoms were included in the refinement.

Related to this discussion is the diversity of fibril structure. In the current study, only the ThT fluorescence signal gives information of the character of the fibrils. Only the $\text{A}\beta(1-40)$ has been studied here, which may have a different structure from the one of $\text{A}\beta(1-42)$ [163]. The A2T and A2V mutations may also affect the morphology of the fibrils [110]. Thus, His13 and His14 could both participate in binding in the fibrils measured here, while other conditions would prevent this.

In most fittings, both angles of the histidines were kept at 0° to avoid overfitting, but it has previously been shown that better fits can be achieved by refining the histidine angles as well [115,116,118,128]. Having a model of four histidines and an oxygen, and refining all distances and angles independently achieved the best fit overall, see Appendix B.3.6. However, for the fits to most of the datasets, two histidines were twisted an average of 30° . Also, having the four histidines at least 0.05 \AA apart may result in destructive interference that, as a result, achieves an artificial better fit to the data [116].

While other studies have found a tendency towards higher coordination numbers with higher pH [116], such a correlation is not found in the current data. It has been suggested that a higher pH leads to a deprotonation of the amide between Asp1 and Ala2, which makes this amide participate in the coordination [120]. A model with a backbone amide was also attempted (see Appendix B), but a good fit could not be achieved.

The refined values of ΔE_0 are relatively large (>10 in some cases), which could lead to erroneous ΔR values in the fitting [25]. While some XAS studies refine ΔE_0 initially against one parameter [118], it was allowed to adjust freely in all

refinements of the current study. The other procedure was applied to the data treatment of ZnA β .

6.4.4 Zinc XAS

While the coordination of Cu²⁺ to A β fibrils could be investigated, the ThT fluorescence treatment of A β with Zn²⁺ caused a zinc compound to precipitate. Possibly, the combination of heating and shaking during the ThT fluorescence caused ZnO to precipitate, as it has previously been shown to form with organic ligands present [164]. Thus, only samples that were not shaken by the plate reader gave XAS signals that were undisturbed by ZnO.

To calculate the amount of ZnO, the signal from the shaken sample of (Zn-A2V)₉ was used as a standard of pure ZnO, and the non-shaken sample of (Zn-WT)₈ was used as a standard of no ZnO. This decision was based on the FT for these two datasets, as can be seen in Figure 56 (left). The FT of (Zn-A2V)₉ has a shoulder at the same distance as the main peak seen for (Zn-WT)₈, which may indicate that some amount of Zn(II) is bound to A β . A linear combination using those two datasets was then performed to fit all other datasets. One example using (Zn-A2T)₉ is given in Figure 56 (right). The amount of ZnO calculated using this method is presented in Table 15. As a content of more than 10% is likely to disturb the EXAFS refinement, only the five samples with less than 10% ZnO content was used for model fitting. For future investigations, it may be possible to subtract the ZnO spectrum and use the remaining signal for refinements.

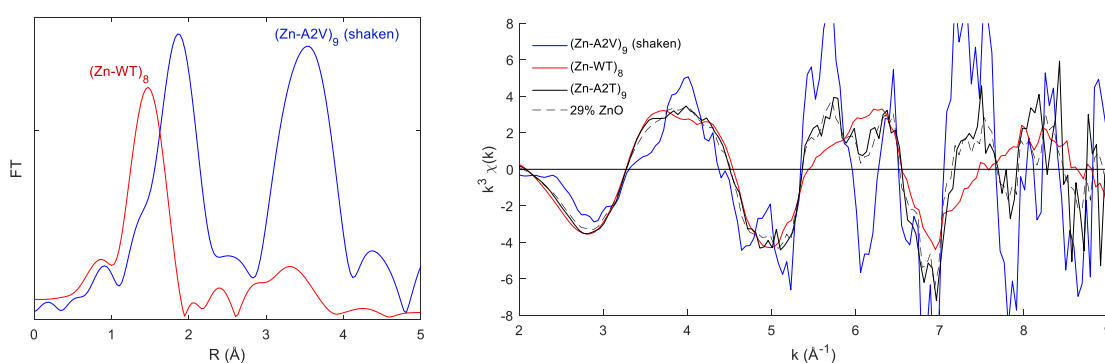


Figure 56 – Left: FT without phase correction of (Zn-WT)₈ and the shaken sample (Zn-A2V)₉. Right: k³-weighted $\chi(k)$ for (Zn-WT)₈, (Zn-A2T)₉, the shaken sample (Zn-A2V)₉, and a linear combination of the former two (dashed). Percentage ZnO is given assuming the shaken sample used as a standard is 100% ZnO.

Table 15 – ZnO content as calculated by a linear combination of (Zn-WT)₈ as a standard of 0% ZnO and the shaken (Zn-A2V)₉ as a standard of 100% ZnO.

Sample	Non-shaken	Shaken
	ZnO content	ZnO content
(Zn-WT) ₇	3%	-
(Zn-WT) ₈	0%*	18%
(Zn-WT) ₉	12%	-
(Zn-A2T) ₇	17%	69%
(Zn-A2T) ₈	4%	27%
(Zn-A2T) ₉	29%	67%
(Zn-A2V) ₇	8%	74%
(Zn-A2V) ₈	3%	32%
(Zn-A2V) ₉	19%	100%*

*This sample was used as a standard for the linear combination

Figure 57 shows the k^3 -weighted $\chi(k)$ for the five Zn(II)A β samples with less than 10% ZnO content. Apart from differences due to ZnO content, no difference is seen as a function of pH nor variant. The height of the shoulder at $k \approx 5.8 \text{ \AA}^{-1}$ as well as the depth of the dip at $k \approx 7.9 \text{ \AA}^{-1}$ are both signs of ZnO, as (Zn-A2V)₇ is the most extreme in both positions, while (Zn-WT)₈ has no sign of these features. As the datasets appear so similar, an average dataset of all five spectra was also attempted to be fit.

Five different models were attempted fitted against the six datasets (including the averaged). The models vary in number of histidines and carboxylate groups, but keep a coordination number of four. The best fit achieved for all models to all datasets can be found in Appendix C. A 2N2O model with two histidines, one carboxylate group and one oxygen or nitrogen atom gave the overall best fit to the data. It can be seen in Figure 58, and the corresponding parameters in Table 16. The experimental spectra are compared with the theoretical calculated spectra from the models in Figure 60.

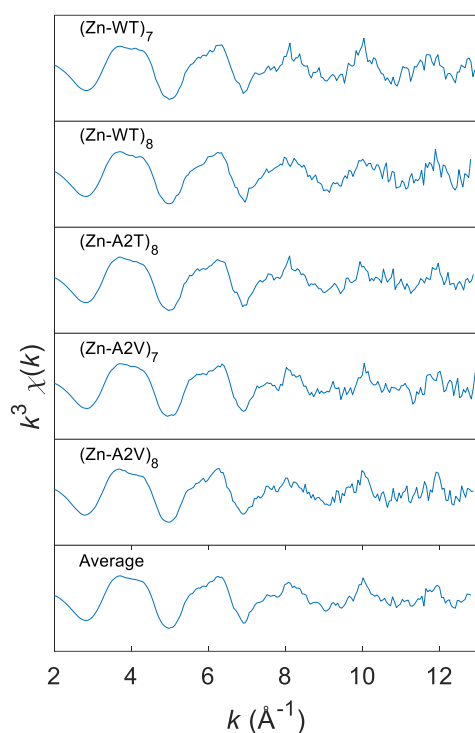


Figure 57 - k^3 -weighted EXAFS functions for $ZnA\beta$ samples without ZnO signal.

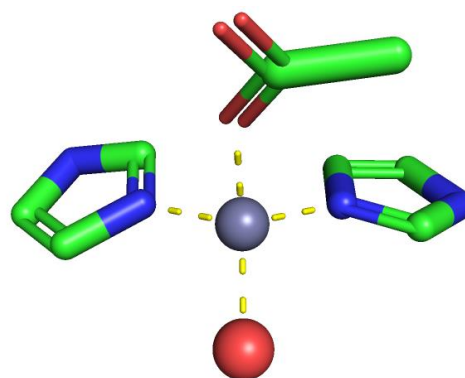


Figure 58 - Model of the best fit to the five $ZnA\beta$ datasets.

No significant differences were found across the five datasets as a function of pH or variant, as expected from the very similar spectra.

The model found to give the best fit is in good agreement with a recent study suggesting two histidines and two carboxylate ligands [122], although only one carboxylate group was fitted in the current study. Looking at the cryo-EM structure [95] mentioned in the introduction, His6, His13 and Glu11 all point towards the center of the fibril, and could easily constitute the binding site of Zn^{2+} . In an attempt to visualize this in Figure 59, the side chains of those residues were rotated to give a suggested geometry requiring very little movement compared to the metal free fibril.

Table 16 – Parameters for the best fits for Zn A β . N is the shell occupation number, R is the shell distance, σ_{DW} is the Debye-Waller factor, E_f is the Fermi energy, R_{EXAFS} is the quality of fit. σ is a statistical standard deviation, calculated from the correlation coefficients. α and β are the twist and tilt angles, respectively.

Ligand	N	$R \pm 2\sigma$ (Å)	α / β (°)	$\sigma_{DW}^2 \pm 2\sigma$ (Å ²)	ΔE_f (eV)	R_{EXAFS}
(Zn-WT) ₇						
His	1	1.94 ± 0.08	0 / 0	0.006 ± 0.004	-1	26%
His	1	2.03 ± 0.09	0 / 0	0.006 ± 0.004		
O _{δ_1} (Glu/Asp)	1	2.00 ± 0.04	28 / 15	0.006 ± 0.004		
O	1	1.98 ± 0.06		0.006 ± 0.004		
(Zn-WT) ₈						
His	1	2.0 ± 0.3	0 / 0	0.006 ± 0.004	0	25%
His	1	2.0 ± 0.3	0 / 0	0.006 ± 0.004		
O _{δ_1} (Glu/Asp)	1	2.02 ± 0.06	30 / 19	0.006 ± 0.004		
O	1	1.94 ± 0.06		0.006 ± 0.004		
(Zn-A2T) ₈						
His	1	1.95 ± 0.03	0 / 0	0.005 ± 0.002	0	26%
His	1	2.05 ± 0.03	0 / 0	0.005 ± 0.002		
O _{δ_1} (Glu/Asp)	1	2.03 ± 0.04	26 / 21	0.005 ± 0.002		
O	1	1.93 ± 0.04		0.005 ± 0.002		
(Zn-A2V) ₇						
His	1	1.93 ± 0.03	0 / 0	0.005 ± 0.002	-1	29%
His	1	2.08 ± 0.03	0 / 0	0.005 ± 0.002		
O _{δ_1} (Glu/Asp)	1	1.95 ± 0.04	24 / 15	0.005 ± 0.002		
O	1	2.01 ± 0.05		0.005 ± 0.002		
(Zn-A2V) ₈						
His	1	1.93 ± 0.01	0 / 0	0.005 ± 0.002	0	28%
His	1	2.05 ± 0.05	0 / 0	0.005 ± 0.002		
O _{δ_1} (Glu/Asp)	1	2.02 ± 0.07	24 / 21	0.005 ± 0.002		
O	1	1.97 ± 0.05		0.005 ± 0.002		
Average of all five datasets						
His	1	1.95 ± 0.02	0 / 0	0.006 ± 0.002	0	22%
His	1	2.05 ± 0.03	0 / 0	0.006 ± 0.002		
O _{δ_1} (Glu/Asp)	1	2.02 ± 0.04	26 / 19	0.006 ± 0.002		
O	1	1.95 ± 0.04		0.006 ± 0.002		

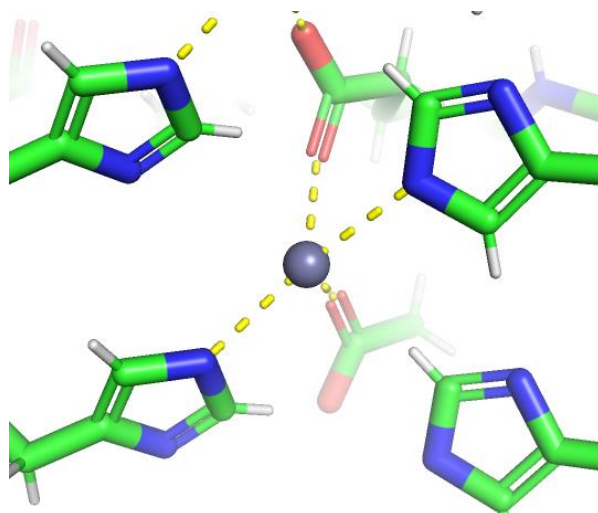


Figure 59 – Attempt at visualizing a coordination of Zn^{2+} in the cryo-EM model (PDB ID: 5OQV) [95] by rotation of sidechains. Zn^{2+} crosslinks two peptides through His6 and His13, while Glu11 binds two Zn^{2+} ions.

Both having two carboxylate groups or one histidine gave worse fits, as presented in Appendix C. However, with respect to having two carboxylate groups, a much better fit was achieved when having one carboxylate at both α and β angles at around 20° . Having the other carboxylate at the same angle did not result in a better fit, but refining the angles of them both independently did not improve the fit compared to having introduced two more parameters. One could imagine that the best orientation for the second carboxylate was simply not found by the refinement procedure of the software.

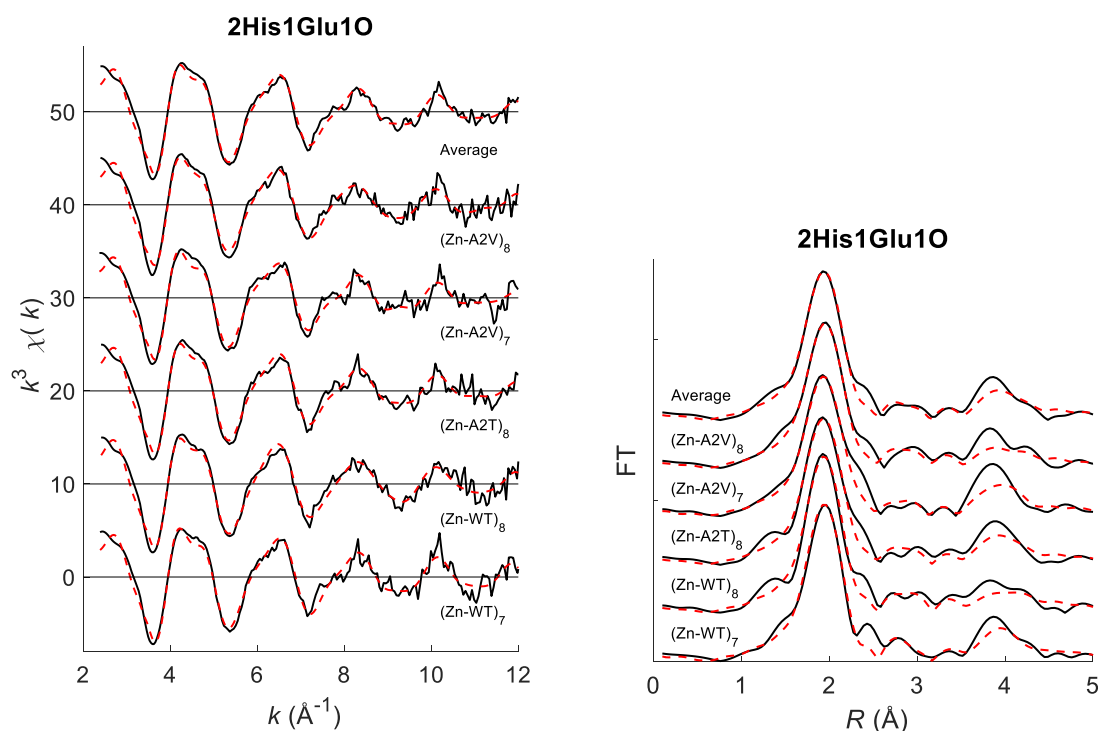


Figure 60 - Left: k^3 -weighted $\chi(k)$ data (solid) and fit (dashed). Each dataset is shifted 10 units in the vertical direction. Right: FT of the same, shifted 15 units in the vertical direction.

6.5 Conclusive Remarks

Several ThT fluorescence experiments were conducted. For CuA β , the lag times across all pH values were found to increase as A2T < WT < A2V, with a tendency towards lag time increasing with pH as well. For ZnA β , fibrillization was also observed at pH 7 and 8, in contrast to previous studies. At pH 8, the lag times increased as WT < A2T < A2V, while no fibrillization was observed at pH 9, possibly explained by the formation of ZnO at low pH preventing Zn²⁺ from inhibiting fibril formation.

Eleven CuA β datasets were collected and EXAFS refinement was carried out for seven of them. Six different models were attempted refined against them, and a best fit was found for each dataset. Data collected on a few high pH samples that were not subject to fibrillar-inducing treatment appeared different in the XANES, possibly having higher coordination numbers. The best fits were achieved using 2/3 histidines, a carboxylic sidechain and 0/1 N-terminal amide, and no clear difference was found across the variants.

XAS was also measured on sixteen samples of ZnA β . Despite the majority of spectra being largely affected by a signal from ZnO, five datasets could be used for EXAFS refinements. These were very similar, and were best fitted with a model of two histidines, one carboxylate and one oxygen or nitrogen ligand in a tetrahedral coordination, in good agreement with previous studies.

For both CuA β and ZnA β , a better fit was achieved with the inclusion of α and β angles as refinement parameters, but the destructive interference effect of multiple scattering may cause this to be an artifact.

7

Conclusion and Perspectives

This chapter seeks to repeat the overall conclusions learned across the multiple projects conducted in the current thesis. Perspectives for BioXAS in general and the individual projects are considered.

During the course of the work related to this thesis, I gained an increase experience with XAS data treatment. The reader will find that certain points highlighted in Chapter 6 are not applied in Chapter 4, which would have required starting from scratch on the data treated in the latter.

7.1 Microfluidics Flow Cell for BioXAS

The original aim of this PhD project was to improve the possibilities for BioXAS experiments by working with the instrumentation and data analysis at the new beamline Balder at MAX IV. Although this aim had to be adjusted due to a delay in the construction of the facilities, a microfluidics flow cell was successfully tested to be able to achieve flow rates sufficient to avoid radiation damage. The device could open up for BioXAS measurements at room temperature, with very little sample consumption, ideal for protein studies.

The flow cell could have been useful for the measurements at ESRF, where photoreduction yet again was proven to be a major issue when collecting XAS data on redox active Cu(II) species. Simply changing position on the sample between each scan including cooling to 4 K proved insufficient to avoid radiation damage. For both PC and A β , the photoreduced coordination is identical to neither the oxidized nor the reduced geometry, similar to what has been seen in metalloproteins with iron [71,72]. Data with little or no photoreduction could be useful for PC(II) at several pH values, as well as for fibrillar Cu(II)A β .

7.2 XAS Investigations of Metals in Biological Systems

While waiting for the better BioXAS beamline, two biological systems were studied using data from three different synchrotrons. At ESRF, data was collected on PC, which is a well-described protein with several ultrahigh resolution crystal structures. Secondly, Cu and Zn K-edge data was collected on A β samples at ESRF and SOLEIL, respectively. Copper and zinc are known to

bind in A β , but in contrast to PC, the coordination in A β is much less understood.

For PC, data was collected on six samples at different pH and oxidation state, and compared to oxidized data measured at MAX II. The EXAFS derived models for the six samples had parameters similar to those of the crystal structures. As our samples suffered from photoreduction, this probably also applies to the crystal structures.

XANES was used for quantitative fitting of models, but did not assist in getting a better fit to the EXAFS or vice versa. Many codes exist that can calculate the theoretical XANES spectrum for specific species. However, as they either use large simplifications, such as the muffin tin approximation, or deal with ground state configurations, as any DFT code, they are not yet able to describe all features found in experimental XANES spectra. With increasing computational power, some of these approximations may be skipped, and allow for more accurate calculations of spectra. A program that considers both the XANES and EXAFS while refining parameters would be very useful.

While many studies have examined the binding of copper and zinc in A β in solution, little attention has been brought to the binding in fibrillar A β .

For CuA β , the fibrillization lag times increase as A2T < WT < A2V, agreeing with recent studies [110,111], with a tendency towards longer lag times with higher pH also observable. A trigonal geometry similar to what has been found for photoreduced CuA β in solution [116] was the result of EXAFS refinements for (Cu-WT)₈, (Cu-WT)₉, (Cu-A2T)₇, and (Cu-A2T)₉. Uncorrelated to the degree of photoreduction, a square pyramidal geometry with three histidines, a carboxylate and an amide group was found to be the best fit for (Cu-A2T)₈, (Cu-A2V)₈, and (Cu-A2V)₉, agreeing with the EPR data on fibrillar A β [125–127].

For ZnA β , fibrillization was observed at pH 7 and 8, in contrast to previous studies. At pH 8, the lag times increased as WT < A2T < A2V, while no fibrillization was observed at pH 9. The majority of spectra from the agitated samples were largely affected by a signal from ZnO. However, five EXAFS datasets from non-agitated samples were collected with little ZnO contamination. While these samples had clear precipitate, they were not monitored by ThT fluorescence, and thus not proven to be fibrillar. Across the three variants, all five datasets were best fitted with a model of two histidines, one carboxylate and one oxygen or nitrogen ligand in a tetrahedral coordination, similar to what a recent NMR/EXAFS study concluded [122].

A time resolved experiment during the course of fibrillization would give an important insight to the nature of copper and zinc binding during fibrillization.

7.3 Statistical Analysis of EXAFS Parameters

The effect of the starting point for EXAFS refinements were evident in the analysis of $A\beta$ data, where several models achieved reasonable fits. While *Excurve* uses a procedure that gradually steps away from the input coordinates until a local minimum is achieved, this limits the refinement in the search for a global minimum.

A DoE was utilized in an attempt to do a more thorough analysis of the parameter space. While a few of the initial random $\sim 50,000$ calculations were close to a good fit, a clever selection of parameters for another or several following runs should be able to achieve one or multiple good fits to the data, and possibly give statistics on how different the fits are.

Bibliography

1. Penner-Hahn JE, Fronko RM, Pecoraro VL, Yocum CF, Betts SD, Bowlby NR. Structural Characterization of the Manganese Sites in the Photosynthetic Oxygen-Evolving Complex Using X-ray Absorption Spectroscopy. *Journal of the American Chemical Society* 1990; **112**: 2549–57.
2. Yachandra VK, Yano J, Kern J et al. Polarized XAS of photosystem II and relevant Mn model complexes. *Acta Crystallographica Section A Foundations of Crystallography* 2011; **67**: C101–C101.
3. Scott RA, Schwartz JR, Cramer SP. Effect of cyanide binding on the copper sites of cytochrome c oxidase: an x-ray absorption spectroscopic study. *Journal of Inorganic Biochemistry* 1985; **23**: 199–205.
4. Shadle SE, Hodgson KO, Solomon EI, Hedman B, Schugar HJ. X-ray Absorption Spectroscopic Studies of the Blue Copper Site: Metal and Ligand K-Edge Studies To Probe the Origin of the EPR Hyperfine Splitting in Plastocyanin. *Journal of the American Chemical Society* 1993; **115**: 767–76.
5. Hasnain SS, Alagna L, Blackburn NJ, Strange RW. EXAFS and XANES of Superoxide Dismutase : a Copper Protein. *Le Journal de Physique Colloques* 1986; **47**: C8-1129-C8-1136.
6. Ross I, Binstead N, Blackburn NJ et al. EXAFS studies of copper and zinc in metallothionein and bovine superoxide dismutase. *Inorganica Chimica Acta* 1983; **79**: 89–90.
7. Sarangi R. A biological perspective towards a standard for information exchange and reporting in XAS. *Journal of Synchrotron Radiation* 2018; **25**: 944–52.
8. Feiters MC, Mangani S. Changes in the perception of biological X-ray absorption spectroscopy between ICBIC 1 and ICBIC 10/BIOXAS 2001: How far have we travelled? *Journal of Synchrotron Radiation* 2002; **9**: 103–4.
9. Pascarelli S. Notes on X-ray Absorption Spectroscopy. 2016.
10. de Broglie M. Sur un nouveau procédé permettant d'obtenir la photographie des spectres de raies des rayons Röntgen. *Comptes rendus de l'Académie des Sciences* 1913; **157**: 924–6.
11. Fricke H. The K-characteristic absorption frequencies for the chemical elements magnesium to chromium. *Physical Review* 1920; **16**: 202–15.
12. Kronig R de L. Zur Theorie der Feinstruktur in den Röntgenabsorptionsspektren. *Zeitschrift für Physik* 1931; **70**: 317–23.
13. Sayers DE, Stern EA, Lytle FW. New Technique for Investigating Noncrystalline Structures: Fourier Analysis of the Extended X-Ray-Absorption Fine Structure. *Physical Review Letters* 1971; **27**: 1204–7.
14. Shulman RG, Eisenberger P, Blumberg WE, Stombaugh NA. Determination of the iron-sulfur distances in rubredoxin by x-ray absorption spectroscopy. *Proceedings of the National Academy of Sciences of the United States of America* 1975; **72**: 4003–7.

15. Kau L-S, Spira-Solomon DJ, Penner-Hahn JE, Hodgson KO, Solomon EI. X-ray Absorption Edge Determination of the Oxidation State and Coordination Number of Copper: Application to the Type 3 Site in *Rhus vernicifera* Laccase and Its Reaction with Oxygen. *Journal of the American Chemical Society* 1987; **109**: 6433–42.
16. Rudolph J, Jacob CR. Revisiting the Dependence of Cu K-Edge X-ray Absorption Spectra on Oxidation State and Coordination Environment. *Inorganic Chemistry* 2018; **57**: 10591–607.
17. Sorrell TN, Jameson DL. An explanation for the observed stoichiometry of carbon monoxide binding to hemocyanin. *Journal of the American Chemical Society* 1982; **104**: 2053–4.
18. Rehr JJJ, Ankudinov ALL. Progress in the theory and interpretation of XANES. *Coordination Chemistry Reviews* 2005; **249**: 131–40.
19. Rehr JJJ, Albers RCRC. Theoretical approaches to x-ray absorption fine structure. *Reviews of Modern Physics* 2000; **72**: 621–54.
20. Joly Y. X-ray absorption near-edge structure calculations beyond the muffin-tin approximation. *Physical Review B - Condensed Matter and Materials Physics* 2001; **63**: 125120.
21. Benfatto M, Della Longa S. Geometrical fitting of experimental XANES spectra by a full multiple-scattering procedure. *Journal of Synchrotron Radiation* 2001; **8**: 1087–94.
22. Jalilehvand F. *Structure of Hydrated Ions and Cyanide Complexes by X-Ray Absorption Spectroscopy*. Tekniska Högskolan i Stockholm, Institutionen för Kemi, 2000.
23. Lytle FW. The EXAFS family tree: a personal history of the development of extended X-ray absorption fine structure. *Journal of synchrotron radiation* 1999; **6**: 123–34.
24. Bès R, Ahopelto T, Honkanen AP et al. Laboratory-scale X-ray absorption spectroscopy approach for actinide research: Experiment at the uranium L3-edge. *Journal of Nuclear Materials* 2018; **507**: 50–3.
25. Kelly SD, Ravel B. EXAFS Energy Shift and Structural Parameters. *AIP Conference Proceedings*. Vol882. AIP, 2007: 132–4.
26. Stern EA. Number of relevant independent points in x-ray-absorption fine-structure spectra. *Physical Review B* 1993; **48**: 9825–7.
27. Binsted N, Strange RW, Samar SH. Constrained and Restrained Refinement in EXAFS Data Analysis with Curved Wave Theory. *Biochemistry* 1992; **31**: 12117–25.
28. Frank M, Carlson DB, Hunter MS et al. Femtosecond X-ray diffraction from two-dimensional protein crystals. *IUCrj* 2014; **1**: 95–100.
29. Barrett R, Faucon M, Lopez J et al. X-ray microfocussing combined with microfluidics for on-chip X-ray scattering measurements. *Lab on a Chip* 2006; **6**: 494–9.
30. Martel A, Burghammer M, Davies R et al. A microfluidic cell for studying the formation of regenerated silk by synchrotron radiation small- and wide-angle X-ray

scattering. *Biomicrofluidics* 2008; **2**.

31. Brenker J, Henzler K, Borca C, Cardarso V, Huthwelker T, Alan T. X-ray compatible microfluidics for in-situ biological and chemical studies at synchrotron light sources. *20th International Conference on Miniaturized Systems for Chemistry and Life Sciences, MicroTAS 2016*. 2016: 942–3.

32. Zeldin OB, Gerstel M, Garman EF. RADDSE-3D: Time- and space-resolved modelling of dose in macromolecular crystallography. *Journal of Applied Crystallography* 2013; **46**: 1225–30.

33. Hubbell JH, Seltzer SM. X-Ray Mass Attenuation Coefficients. *NIST Standard Reference Database 126*, 2004. <https://www.nist.gov/pml/x-ray-mass-attenuation-coefficients> (accessed December 1, 2018).

34. Brooks-Bartlett JC, Batters RA, Bury CS et al. Development of tools to automate quantitative analysis of radiation damage in SAXS experiments. *Journal of Synchrotron Radiation* 2017; **24**: 1–10.

35. Kuwamoto S, Akiyama S, Fujisawa T. Radiation damage to a protein solution, detected by synchrotron X-ray small-angle scattering: Dose-related considerations and suppression by cryoprotectants. *Journal of Synchrotron Radiation* 2004; **11**: 462–8.

36. Schwemmer F, Blanchet CE, Spilotros A et al. LabDisk for SAXS: a centrifugal microfluidic sample preparation platform for small-angle X-ray scattering. *Lab Chip* 2016; **16**: 1161–70.

37. Ghazal A, Gontsarik M, Kutter JP et al. Direct monitoring of calcium-triggered phase transitions in cubosomes using small-angle X-ray scattering combined with microfluidics. *Journal of Applied Crystallography* 2016; **49**: 2005–14.

38. Chan EM, Marcus MA, Fakra S, ElNaggar M, Mathies RA, Alivisatos AP. Millisecond kinetics of nanocrystal cation exchange using microfluidic X-ray absorption spectroscopy. *The journal of physical chemistry. A* 2007; **111**: 12210–5.

39. Malkin R, Malmström BG. The state and function of copper in biological systems. *Advances in enzymology and related areas of molecular biology* 1970; **33**: 177–244.

40. Davis DJ, Krogmann DW, Pietro AS. Electron donation to photosystem I. *Plant physiology* 1980; **65**: 697–702.

41. Redinbo MR, Yeates TO, Merchant S. Plastocyanin: structural and functional analysis. *Journal of bioenergetics and biomembranes* 1994; **26**: 49–66.

42. Hope AB. Electron transfers amongst cytochrome f, plastocyanin and photosystem I: kinetics and mechanisms. *Biochimica et biophysica acta* 2000; **1456**: 5–26.

43. Sykes AG. Plastocyanin and the Blue Copper Proteins. *Long-Range Electron Transfer in Biology* 1990: 175–233.

44. Solomon EI, Hadt RG. Recent advances in understanding blue copper proteins. *Coordination Chemistry Reviews* 2011; **255**: 774–89.

45. Chaboy J, Díaz-Moreno S, Díaz-Moreno I, De La Rosa MA, Díaz-Quintana A. How the local geometry of the cu-binding site determines the thermal stability of blue copper proteins. *Chemistry and Biology* 2011; **18**: 25–31.

46. Muñoz-López FJ, Beltrán EF, Díaz-Moreno S et al. Modulation of copper site properties by remote residues determines the stability of plastocyanins. *FEBS Letters* 2010; **584**: 2346–50.
47. Mitchell Guss J, Freeman HC. Structure of oxidized poplar plastocyanin at 1.6 Å resolution. *Journal of Molecular Biology* 1983; **169**: 521–63.
48. Monari A, Very T, Rivail JL, Assfeld X. A QM/MM study on the spinach plastocyanin: Redox properties and absorption spectra. *Computational and Theoretical Chemistry* 2012; **990**: 119–25.
49. Scott RA, Hahn JE, Hodgson KO, Doniach S, Freeman HC. Polarized X-ray Absorption Spectra of Oriented Plastocyanin Single Crystals. Investigation of Methionine-Copper Coordination. *Journal of the American Chemical Society* 1982; **104**: 5364–9.
50. Penner-Hahn JE, Murata M, Hodgson KO, Freeman HC. Low-temperature X-ray absorption spectroscopy of plastocyanin: Evidence for copper-site photoreduction at cryogenic temperatures. *Inorganic Chemistry* 1989; **28**: 1826–32.
51. Díaz-Moreno I, Díaz-Quintana A, Díaz-Moreno S, Subías G, De la Rosa MA. Transient binding of plastocyanin to its physiological redox partners modifies the copper site geometry. *FEBS Letters* 2006; **580**: 6187–94.
52. Kachalova GS, Shosheva AC, Bourenkov GP, Donchev AA, Dimitrov MI, Bartunik HD. Structural comparison of the poplar plastocyanin isoforms PCa and PCb sheds new light on the role of the copper site geometry in interactions with redox partners in oxygenic photosynthesis. *Journal of Inorganic Biochemistry* 2012; **115**: 174–81.
53. Schmidt L, Christensen HEM, Harris P et al. Structure of plastocyanin from the cyanobacterium *Anabaena variabilis*. *Acta Crystallographica Section D: Biological Crystallography* 2006; **62**: 1022–9.
54. Ellis PJ. *Structural Studies of Metalloproteins Using X-Ray Absorption Spectroscopy and x-Ray Diffraction*. University of Sydney, School of Chemistry, 1995.
55. Frankær CG, Knudsen MV, Norén K, Nazarenko E, Sthl K, Harris P. The structures of T6, T3R3 and R 6 bovine insulin: Combining X-ray diffraction and absorption spectroscopy. *Acta Crystallographica Section D: Biological Crystallography* 2012; **68**: 1259–71.
56. Geoff R-C, Overton T. *Descriptive Inorganic Chemistry*, Fourth Edi. New York: W.H. Freeman and Company, 2006.
57. Frankær CG, Harris P, Ståhl K. A sample holder for in-house X-ray powder diffraction studies of protein powders. *Journal of Applied Crystallography* 2011; **44**: 1288–90.
58. Carlson S, Clausén M, Gridneva L, Sommarin B, Svensson C. XAFS experiments at beamline I811, MAX-lab synchrotron source, Sweden. *Journal of Synchrotron Radiation* 2006; **13**: 359–64.
59. Dau H, Liebisch P, Haumann M. X-ray absorption spectroscopy to analyze nuclear geometry and electronic structure of biological metal centers-potential and questions examined with special focus on the tetra-nuclear manganese complex of oxygenic photosynthesis. *Analytical and Bioanalytical Chemistry* 2003; **376**: 562–83.

60. Binsted N. Excurve v. 9.330 CCLRC Daresbury Laboratory computer program.
61. Ravel B, Newville M, IUCr, C. AR, J. EM, Y. Y. ATHENA, ARTEMIS, HEPHAESTUS: data analysis for X-ray absorption spectroscopy using IFEFFIT. *Journal of Synchrotron Radiation* 2005; **12**: 537–41.
62. Bourke JD, Chantler CT, Joly Y. FDMX: Extended X-ray absorption fine structure calculations using the finite difference method. *Journal of Synchrotron Radiation* 2016; **23**: 551–9.
63. Smolentsev G, Soldatov A. Quantitative local structure refinement from XANES: multi-dimensional interpolation approach. *Journal of Synchrotron Radiation* 2006; **13**: 19–29.
64. Smolentsev G, Soldatov AV. FitIt: New software to extract structural information on the basis of XANES fitting. *Computational Materials Science* 2007; **39**: 569–74.
65. Joly Y, Phys J, Ser C. Related content Self-consistency , spin-orbit and other advances in the FDMNES code to simulate XANES and RXD experiments Self-consistency , spin-orbit and other advances in the FDMNES code to simulate XANES and RXD experiments. 2009; doi 10.1088/1742-6596/190/1/012007.
66. Solomon EI, Szilagyi RK, DeBeer George S, Basumallick L. Electronic Structures of Metal Sites in Proteins and Models: Contributions to Function in Blue Copper Proteins. *Chemical Reviews* 2004; **104**: 419–58.
67. Kojiro CL, Markley JL. Connectivity of proton and carbon spectra of the blue copper protein, plastocyanin, established by two-dimensional nuclear magnetic resonance. *FEBS Letters* 1983; **162**: 52–6.
68. Sykes AG. Tilden Lecture. Structure and electron-transfer reactivity of the blue copper protein plastocyanin. *Chemical Society Reviews* 1985; **14**: 283–315.
69. Markley JL, Ulrich EL, Berg SP, Krogmann DW. Nuclear magnetic resonance studies of the copper binding sites of blue copper proteins. Oxidized, reduced, and apo-plastocyanin. *Biochemistry* 1975; **14**.
70. Jackman MP, McGinnis J, Sykes AG, Collyer CA, Murata M, Freeman HC. Kinetic studies on 1 : 1 electron-transfer reactions involving blue copper proteins. Part 14. Reactions of poplar plastocyanin with inorganic complexes. *Journal of the Chemical Society, Dalton Transactions* 1987: 2573.
71. George GN, Pickering IJ, Jake Pushie M et al. X-ray-induced photo-chemistry and X-ray absorption spectroscopy of biological samples. *Journal of Synchrotron Radiation* 2012; **19**: 875–86.
72. Sigfridsson KG V, Chernev P, Leidel N, Popovic-Bijelic A, Gräslund A, Haumann M. Rapid X-ray photoreduction of dimetal-oxygen cofactors in ribonucleotide reductase. *The Journal of biological chemistry* 2013; **288**: 9648–61.
73. Nienaber KH, Pushie MJ, Cotelesage JJH, Pickering IJ, George GN. Cryoprotectants Severely Exacerbate X-ray-Induced Photoreduction. *Journal of Physical Chemistry Letters* 2018; **9**: 540–4.
74. Frankaer CG, Mossin S, Ståhl K, Harris P. Towards accurate structural characterization of metal centres in protein crystals: the structures of Ni and Cu T6 bovine insulin derivatives. *Acta Crystallographica Section D: Biological*

Crystallography 2014; **70**: 110–22.

75. Danish Dementia Research Centre. Forekomst af demens i Danmark. <http://www.videnscenterfordemens.dk/statistik/forekomst-af-demens-i-danmark/> (accessed September 23, 2019).

76. Danmarks Statistik. BEFOLKNINGS-FREMSKRIVNING. 2019. <https://www.dst.dk/da/Statistik/emner/befolkning-og-valg/befolkning-og-befolkningsfremskrivning/befolkningsfremskrivning> (accessed September 23, 2019).

77. Price JL, McKeel DW, Buckles VD et al. Neuropathology of nondemented aging: Presumptive evidence for preclinical Alzheimer disease. *Neurobiology of Aging* 2009; **30**: 1026–36.

78. Bouwman FH, Schoonenboom NSM, Verwey NA et al. CSF biomarker levels in early and late onset Alzheimer's disease. *Neurobiology of Aging* 2009; **30**: 1895–901.

79. Aizenstein HJ, Nebes RD, Saxton JA et al. Frequent Amyloid Deposition Without Significant Cognitive Impairment Among the Elderly. *Archives of Neurology* 2008; **65**: 1509.

80. Pearson HA, Peers C. Physiological roles for amyloid beta peptides. *The Journal of physiology* 2006; **575**: 5–10.

81. Kepp KP. Alzheimer's disease: How metal ions define β -amyloid function. *Coordination Chemistry Reviews* 2017; **351**: 127–59.

82. Hardy J, Selkoe DJ. The amyloid hypothesis of Alzheimer's disease: progress and problems on the road to therapeutics. 2002; **297**.

83. Karran E, Mercken M, De Strooper B. The amyloid cascade hypothesis for Alzheimer's disease: an appraisal for the development of therapeutics. *Nature reviews. Drug discovery* 2011; **10**: 698–712.

84. Tomaselli S, Esposito V, Vangone P et al. The α -to- β Conformational Transition of Alzheimer's A β -(1-42) Peptide in Aqueous Media is Reversible: A Step by Step Conformational Analysis Suggests the Location of β Conformation Seeding. *ChemBioChem* 2006; **7**: 257–67.

85. Shao H, Jao S, Ma K, Zagorski MG. Solution structures of micelle-bound amyloid β -(1-40) and β -(1-42) peptides of Alzheimer's disease 1 Edited by P. E. Wright. *Journal of Molecular Biology* 1999; **285**: 755–73.

86. Murray Coles §, Wendy Bicknell ||, Andrew A. Watson §, David P. Fairlie § and, David J. Craik* §. Solution Structure of Amyloid β -Peptide(1–40) in a Water–Micelle Environment. Is the Membrane-Spanning Domain Where We Think It Is?†,‡. 1998; doi 10.1021/BI972979F.

87. Sticht H, Bayer P, Willbold D et al. Structure of Amyloid A4-(1-40)-Peptide of Alzheimer's Disease. *European Journal of Biochemistry* 1995; **233**: 293–8.

88. Serpell LC. Alzheimer's amyloid fibrils: Structure and assembly. *Biochimica et Biophysica Acta - Molecular Basis of Disease*, 2000. <http://www.ncbi.nlm.nih.gov/pubmed/10899428> (accessed October 2, 2019).

89. Petkova AT, Ishii Y, Balbach JJ et al. A structural model for Alzheimer's β -amyloid

fibrils based on experimental constraints from solid state NMR. *Proceedings of the National Academy of Sciences of the United States of America* 2002; **99**: 16742–7.

90. Tycko R. Progress towards a molecular-level structural understanding of amyloid fibrils. *Current Opinion in Structural Biology*, 2004. <http://www.ncbi.nlm.nih.gov/pubmed/15102455> (accessed October 2, 2019).

91. Whittemore NA, Whittemore R, Kheterpal I, Williams AD, Wetzel R, Serpersu EH. Hydrogen–Deuterium (H/D) Exchange Mapping of A β 1-40 Amyloid Fibril Secondary Structure Using Nuclear Magnetic Resonance Spectroscopy. *Biochemistry* 2005; **44**: 4434–41.

92. Petkova AT, Yau WM, Tycko R. Experimental constraints on quaternary structure in Alzheimer's β -amyloid fibrils. *Biochemistry* 2006; **45**: 498–512.

93. Paravastu AK, Leapman RD, Yau WM, Tycko R. Molecular structural basis for polymorphism in Alzheimer's β -amyloid fibrils. *Proceedings of the National Academy of Sciences of the United States of America* 2008; **105**: 18349–54.

94. Bertini I, Gonnelli L, Luchinat C, Mao J, Nesi A. A new structural model of A β 40 fibrils. *Journal of the American Chemical Society* 2011; **133**: 16013–22.

95. Gremer L, Schölzel D, Schenk C et al. Fibril structure of amyloid- β (1-42) by cryo-electron microscopy. *Science (New York, N.Y.)* 2017; **358**: 116–9.

96. Lovell MA, Robertson JD, Teesdale WJ, Campbell JL, Markesbery WR. Copper, iron and zinc in Alzheimer's disease senile plaques. *Journal of the Neurological Sciences* 1998; **158**: 47–52.

97. Atwood CS, Moir RD, Huang X et al. Dramatic aggregation of Alzheimer abeta by Cu(II) is induced by conditions representing physiological acidosis. *The Journal of biological chemistry* 1998; **273**: 12817–26.

98. Bush A, Pettingell W, Multhaup G et al. Rapid induction of Alzheimer A beta amyloid formation by zinc. *Science* 1994; **265**: 1464–7.

99. Adlard PA, Bush AI. Metals and Alzheimer's disease. *Journal of Alzheimer's Disease* 2006; **10**: 145–63.

100. Barnham KJ, Bush AI. Metals in Alzheimer's and Parkinson's Diseases. *Current Opinion in Chemical Biology* 2008; **12**: 222–8.

101. Bagheri S, Squitti R, Haertlé T, Siotto M, Saboury AA. Role of Copper in the Onset of Alzheimer's Disease Compared to Other Metals. *Frontiers in aging neuroscience* 2017; **9**: 446.

102. Yoshiike Y, Tanemura K, Murayama O et al. New Insights on How Metals Disrupt Amyloid β -Aggregation and Their Effects on Amyloid- β Cytotoxicity. *Journal of Biological Chemistry* 2001; **276**: 32293–9.

103. Tōugu V, Karafin A, Zovo K et al. Zn(II)- and Cu(II)-induced non-fibrillar aggregates of amyloid- β (1-42) peptide are transformed to amyloid fibrils, both spontaneously and under the influence of metal chelators. *Journal of Neurochemistry* 2009; **110**: 1784–95.

104. Syme CD, Viles JH. Solution ^1H NMR investigation of Zn $^{2+}$ and Cd $^{2+}$ binding to amyloid-beta peptide (A β) of Alzheimer's disease. *Biochimica et Biophysica Acta* -

Proteins and Proteomics 2006; **1764**: 246–56.

105. Jonsson T, Atwal JK, Steinberg S et al. A mutation in APP protects against Alzheimer's disease and age-related cognitive decline. *Nature* 2012; **488**: 96–9.

106. Di Fede G, Catania M, Morbin M et al. A recessive mutation in the APP gene with dominant-negative effect on amyloidogenesis. *Science* 2009; **323**: 1473–7.

107. Benilova I, Gallardo R, Ungureanu AA et al. The Alzheimer disease protective mutation A2T modulates kinetic and thermodynamic properties of amyloid- β (A β) aggregation. *Journal of Biological Chemistry* 2014; **289**: 30977–89.

108. Messa M, Colombo L, Del Favero E et al. The peculiar role of the A2V mutation in amyloid- β (A β) 1-42 molecular assembly. *Journal of Biological Chemistry* 2014; **289**: 4143–24152.

109. Maloney JA, Bainbridge T, Gustafson A et al. Molecular mechanisms of Alzheimer disease protection by the A673T allele of amyloid precursor protein. *Journal of Biological Chemistry* 2014; **289**: 30990–1000.

110. Murray B, Sorci M, Rosenthal J et al. A2T and A2V A β peptides exhibit different aggregation kinetics, primary nucleation, morphology, structure, and LTP inhibition. *Proteins: Structure, Function and Bioinformatics* 2016; **84**: 488–500.

111. Somavarapu AK, Shen F, Teilum K et al. The Pathogenic A2V Mutant Exhibits Distinct Aggregation Kinetics, Metal Site Structure, and Metal Exchange of the Cu²⁺-A β Complex. *Chemistry - A European Journal* 2017; **23**: 13591–5.

112. Lin T, Chang C, Chang Y, Liao Y, Yu H, Chen R. Alzheimer's amyloid- β A2T variant and its N-terminal peptides inhibit amyloid- β fibrillization and rescue the induced cytotoxicity. 2017: 1–19.

113. Meinhardt J, Tartaglia GG, Pawar A et al. Similarities in the thermodynamics and kinetics of aggregation of disease-related A β (1-40) peptides. *Protein Science* 2007; **16**: 1214–22.

114. Minicozzi V, Stellato F, Comai M et al. Identifying the minimal copper- and zinc-binding site sequence in amyloid- β peptides. *Journal of Biological Chemistry* 2008; **283**: 10784–92.

115. Streltsov VA, Titmuss SJ, Epa VC, Barnham KJ, Masters CL, Varghese JN. The structure of the amyloid- β peptide high-affinity copper II binding site in Alzheimer disease. *Biophysical Journal* 2008; **95**: 3447–56.

116. Summers KL, Schilling KM, Roseman G et al. X-ray Absorption Spectroscopy Investigations of Copper(II) Coordination in the Human Amyloid β Peptide. *Inorganic Chemistry* 2019; **58**: 6294–311.

117. Himes RA, Park GY, Siluvai GS, Blackburn NJ, Karlin KD. Structural Studies of Copper (I) Complexes of Amyloid- b Peptide Fragments: Formation of Two-Coordinate Bis (histidine) Complexes **. 2008: 9084–7.

118. Shearer J, Szalai VA. The Amyloid-Peptide of Alzheimer's Disease Binds Cu I in a Linear Bis-His Coordination Environment: Insight into a Possible Neuroprotective Mechanism for the Amyloid-Peptide. *Journal of the American Chemical Society* 2008; **130**: 17826–35.

119. Hureau C, Balland V, Coppel Y, Solari PL, Fonda E, Faller P. Importance of dynamical processes in the coordination chemistry and redox conversion of copper amyloid- β complexes. *Journal of Biological Inorganic Chemistry* 2009; **14**: 995–1000.
120. Hureau C, Coppel Y, Dorlet P et al. Deprotonation of the Asp1-Ala2 peptide bond induces modification of the dynamic copper(II) environment in the amyloid- β peptide near physiological pH. *Angewandte Chemie - International Edition* 2009; **48**: 9522–5.
121. Cheignon C, Faller P, Testemale D, Hureau C, Collin F. Metal-catalyzed oxidation of A β and the resulting reorganization of Cu binding sites promote ROS production. *Metallomics* 2016; **8**: 1081–9.
122. Alies B, Conte-Daban A, Sayen S et al. Zinc(II) Binding Site to the Amyloid- β Peptide: Insights from Spectroscopic Studies with a Wide Series of Modified Peptides. *Inorganic Chemistry* 2016; **55**: 10499–509.
123. Dong J, Atwood CS, Anderson VE et al. Metal Binding and Oxidation of Amyloid- β within Isolated Senile Plaque Cores: Raman Microscopic Evidence. *Biochemistry* 2003; **42**: 2768–73.
124. Antzutkin ON. Amyloidosis of Alzheimer's A β peptides: solid-state nuclear magnetic resonance, electron paramagnetic resonance, transmission electron microscopy, scanning transmission electron microscopy and atomic force microscopy studies. *Magnetic Resonance in Chemistry* 2004; **42**: 231–46.
125. Karr JW, Akintoye H, Kaupp LJ, Szalai VA. N-Terminal Deletions Modify the Cu²⁺ Binding Site in Amyloid- β . *Biochemistry* 2005; **44**: 5478–87.
126. Sarell CJ, Syme CD, Rigby SEJ, Viles JH. Copper(II) Binding to Amyloid- β Fibrils of Alzheimer's Disease Reveals a Picomolar Affinity: Stoichiometry and Coordination Geometry Are Independent of A β Oligomeric Form. *Biochemistry* 2009; **48**: 4388–402.
127. Gunderson WA, Hernández-Guzmán J, Karr JW, Sun L, Szalai VA, Warncke K. Local Structure and Global Patterning of Cu²⁺ Binding in Fibrillar Amyloid- β [A β (1–40)] Protein. *Journal of the American Chemical Society* 2012; **134**: 18330–7.
128. Shearer J, Callan PE, Tran T, Szalai VA. Cu K-edge X-ray absorption spectroscopy reveals differential copper coordination within amyloid- β oligomers compared to amyloid- β monomers. *Chemical Communications* 2010; **46**: 9137–9.
129. Huang X, Cuajungco MP, Atwood CS et al. Cu(II) potentiation of alzheimer abeta neurotoxicity. Correlation with cell-free hydrogen peroxide production and metal reduction. *The Journal of biological chemistry* 1999; **274**: 37111–6.
130. Curtain CC, Ali F, Volitakis I et al. Alzheimer's Disease Amyloid- β Binds Copper and Zinc to Generate an Allosterically Ordered Membrane-penetrating Structure Containing Superoxide Dismutase-like Subunits. *Journal of Biological Chemistry* 2001; **276**: 20466–73.
131. Kowalik-Jankowska T, Ruta M, Wiśniewska K, Łankiewicz L. Coordination abilities of the 1–16 and 1–28 fragments of β -amyloid peptide towards copper(II) ions: a combined potentiometric and spectroscopic study. *Journal of Inorganic Biochemistry* 2003; **95**: 270–82.
132. Syme CD, Nadal RC, Rigby SEJ, Viles JH. Copper Binding to the Amyloid- β (A β) Peptide Associated with Alzheimer's Disease. *Journal of Biological Chemistry* 2004;

279: 18169–77.

133. Guilloreau L, Damian L, Coppel Y, Mazarguil H, Winterhalter M, Faller P. Structural and thermodynamical properties of CuII amyloid- β 16/28 complexes associated with Alzheimer's disease. *JBIC Journal of Biological Inorganic Chemistry* 2006; **11**: 1024–38.

134. Stellato F, Menestrina G, Serra MD et al. Metal binding in amyloid β -peptides shows intra- and inter-peptide coordination modes. *European Biophysics Journal* 2006; **35**: 340–51.

135. Dorlet P, Gambarelli S, Faller P, Hureau C. Pulse EPR Spectroscopy Reveals the Coordination Sphere of Copper(II) Ions in the 1-16 Amyloid- β Peptide: A Key Role of the First Two N-Terminus Residues. *Angewandte Chemie* 2009; **121**: 9437–40.

136. Alies B, Eury H, Bijani C, Rechinat L, Faller P, Hureau C. pH-Dependent Cu(II) Coordination to Amyloid- β Peptide: Impact of Sequence Alterations, Including the H6R and D7N Familial Mutations. *Inorganic Chemistry* 2011; **50**: 11192–201.

137. Shin B, Saxena S. Substantial Contribution of the Two Imidazole Rings of the His13–His14 Dyad to Cu(II) Binding in Amyloid- β (1–16) at Physiological pH and Its Significance. *The Journal of Physical Chemistry A* 2011; **115**: 9590–602.

138. Alies B, Bijani C, Sayen S, Guillon E, Faller P, Hureau C. Copper coordination to native N-terminally modified versus full-length amyloid- β : Second-sphere effects determine the species present at physiological pH. *Inorganic Chemistry* 2012; **51**: 12988–3000.

139. Alies B, Lapenna G, Sayen S, Guillon E, Hureau C, Faller P. Insights into the mechanisms of amyloid formation of ZnII-Ab11-28: PH-dependent zinc coordination and overall charge as key parameters for kinetics and the structure of ZnII-Ab11-28 aggregates. *Inorganic Chemistry* 2012; **51**: 7897–902.

140. Hou L, Zagorski MG. NMR reveals anomalous copper(II) binding to the amyloid A β peptide of Alzheimer's disease. *Journal of the American Chemical Society* 2006; **128**: 9260–1.

141. Ma QF, Hu J, Wu WH et al. Characterization of copper binding to the peptide amyloid- β (1-16) associated with Alzheimer's disease. *Biopolymers* 2006; **83**: 20–31.

142. Brown ID, Altermatt D, IUCr. Bond-valence parameters obtained from a systematic analysis of the Inorganic Crystal Structure Database. *Acta Crystallographica Section B Structural Science* 1985; **41**: 244–7.

143. Thorp HH. Bond valence sum analysis of metal-ligand bond lengths in metalloenzymes and model complexes. *Inorganic Chemistry* 1992; **31**: 1585–8.

144. Calvo R, Isern H, Mesa MA. EPR Study of Cu(L-ILE)₂, a copper-amino acid salt. *Chemical Physics* 1985; **100**: 89–99.

145. Parthasarathy S, Long F, Miller Y et al. Molecular-level examination of Cu²⁺ binding structure for amyloid fibrils of 40-residue alzheimer's β by solid-state NMR spectroscopy. *Journal of the American Chemical Society* 2011; **133**: 3390–400.

146. Miura T, Suzuki K, Kohata N, Takeuchi H. Metal binding modes of Alzheimer's amyloid β -peptide in insoluble aggregates and soluble complexes. *Biochemistry* 2000; **39**: 7024–31.

147. Shin B, Saxena S. Direct Evidence That All Three Histidine Residues Coordinate to Cu(II) in Amyloid- β 1–16. *Biochemistry* 2008; **47**: 9117–23.
148. Drew SC, Noble CJ, Masters CL, Hanson GR, Barnham KJ. Pleomorphic Copper Coordination by Alzheimer's Disease Amyloid- β Peptide. *Journal of the American Chemical Society* 2009; **131**: 1195–207.
149. Drew SC, Masters CL, Barnham KJ. Alanine-2 carbonyl is an oxygen ligand in Cu²⁺ coordination of Alzheimer's disease amyloid- β peptide - Relevance to N-terminally truncated forms. *Journal of the American Chemical Society* 2009; **131**: 8760–1.
150. Dudev T, Lim C. Tetrahedral vs octahedral zinc complexes with ligands of biological interest: A DFT/CDM study. *Journal of the American Chemical Society* 2000; **122**: 11146–53.
151. Zirah S, Kozin SA, Mazur AK et al. Structural changes of region 1-16 of the Alzheimer disease amyloid β -peptide upon zinc binding and in vitro aging. *Journal of Biological Chemistry* 2006; **281**: 2151–61.
152. Danielsson J, Pierattelli R, Banci L, Gräslund A. High-resolution NMR studies of the zinc-binding site of the Alzheimer's amyloid β -peptide. *FEBS Journal* 2007; **274**: 46–59.
153. Rezaei-Ghaleh N, Giller K, Becker S, Zweckstetter M. Effect of zinc binding on β -amyloid structure and dynamics: implications for A β aggregation. *Biophysical journal* 2011; **101**: 1202–11.
154. Romão C V., Mitchell EP, McSweeney S. The crystal structure of Deinococcus radiodurans Dps protein (DR2263) reveals the presence of a novel metal centre in the N terminus. *Journal of Biological Inorganic Chemistry* 2006; **11**: 891–902.
155. Gustchina A, Li M, Wünschmann S, Chapman MD, Pomés A, Wlodawer A. Crystal structure of cockroach allergen Bla g 2, an unusual zinc binding aspartic protease with a novel mode of self-inhibition. *Journal of Molecular Biology* 2005; **348**: 433–44.
156. Tainer JA, Getzoff ED, Beem KM, Richardson JS, Richardson DC. Determination and analysis of the 2 Å structure of copper, zinc superoxide dismutase. *Journal of Molecular Biology* 1982; **160**: 181–217.
157. Schrödinger, LLC. *The {PyMOL} Molecular Graphics System, Version~1.3r1.*, 2010.
158. Raman B, Ban T, Yamaguchi KI et al. Metal ion-dependent effects of clioquinol on the fibril growth of an amyloid β peptide. *Journal of Biological Chemistry* 2005; **280**: 16157–62.
159. Solomonov I, Korkotian E, Born B et al. Zn²⁺-A β 40 complexes form metastable quasi-spherical oligomers that are cytotoxic to cultured hippocampal neurons. *Journal of Biological Chemistry* 2012; **287**: 20555–64.
160. Sharma AK, Pavlova ST, Kim J, Kim J, Mirica LM. The effect of Cu²⁺ and Zn²⁺ on the A β 42 peptide aggregation and cellular toxicity. *Metallomics*. Vol5. 2013: 1529–36.
161. Zhang T, Pauly T, Nagel-Steger L. Stoichiometric Zn²⁺ interferes with the self-association of A β 42: Insights from size distribution analysis. *International Journal of Biological Macromolecules* 2018; **113**: 631–9.
162. Williams AD, Portelius E, Kheterpal I et al. Mapping A β amyloid fibril secondary

structure using scanning proline mutagenesis. *Journal of Molecular Biology* 2004; **335**: 833–42.

163. Olofsson A, Lindhagen-Persson M, Sauer-Eriksson AE, Ohman A. Amide solvent protection analysis demonstrates that amyloid-beta(1-40) and amyloid-beta(1-42) form different fibrillar structures under identical conditions. *The Biochemical journal* 2007; **404**: 63–70.

164. Trindade T, Pedrosa De Jesus JD, O'Brien P. Preparation of zinc oxide and zinc sulfide powders by controlled precipitation from aqueous solution. *Journal of Materials Chemistry* 1994; **4**: 1611–7.

Appendix A

A β ThT Fluorescence Diagrams

A.1 Introduction

In this appendix, raw ThT fluorescence diagrams are presented. *Corning 96* Well fluorescence plates were purchased from *Sigma-Aldrich (CLS3881)*. 100 μ l of Cu(II)A β solution or Zn(II)A β solution was added to each well, with 10 and 5 replicates, respectively. Each well was sealed immediately after being filled. The plate was loaded into an *OPTIMA FLUOstar* microplate reader from *BMG LABTECH*, and an experiment was setup at 37°C with 10 flashes per well with an excitation at 440 nm and emission at 490 nm, corresponding to the signal from Thioflavin T, and a gain of 1500. The plate was read every 5 minutes with 3 seconds of double orbital shaking before measuring. For Cu(II)A β , two experiments, #1 and #2, were conducted on two separate dates. Unused solution was stored at room temperature.

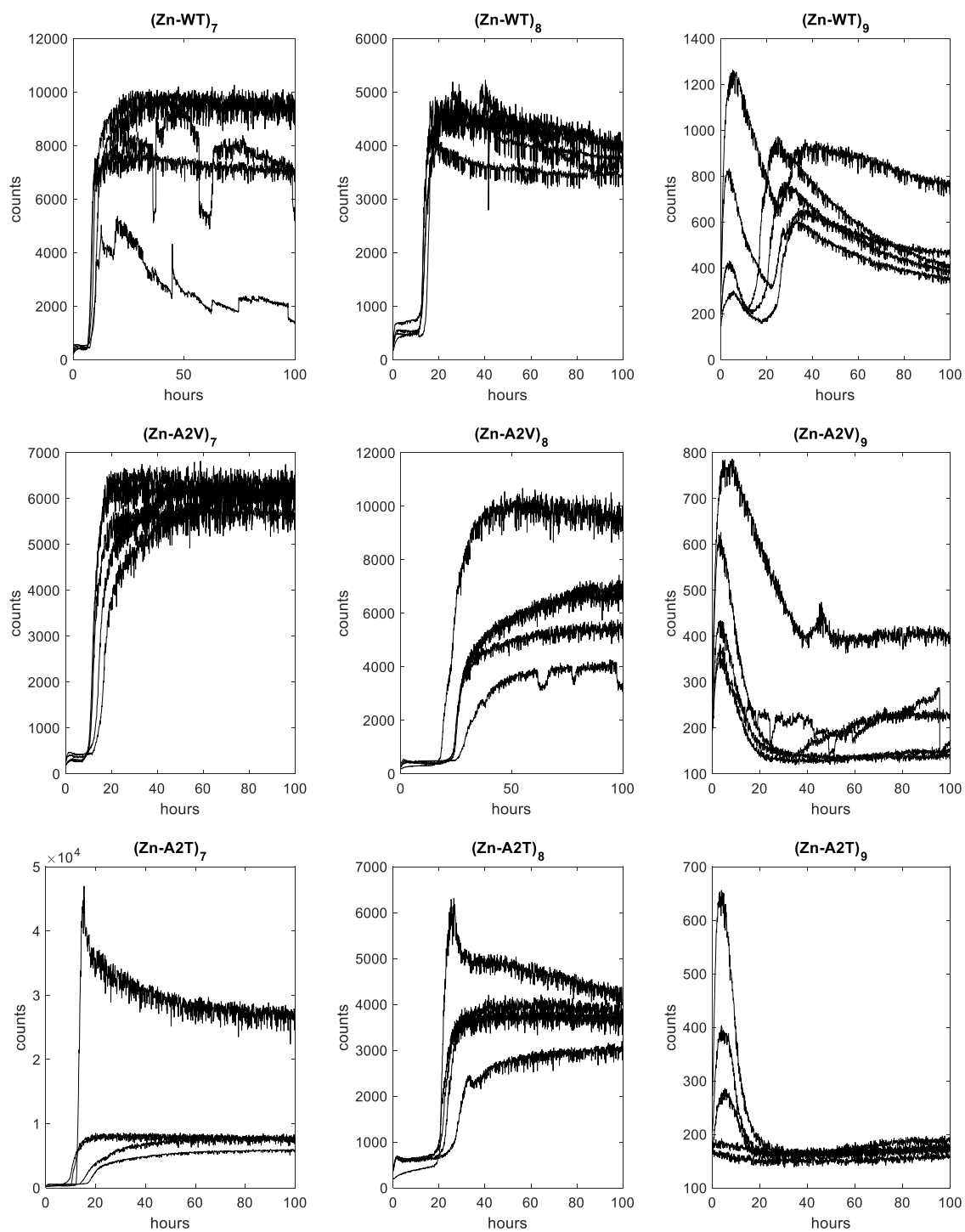
A.3 ZnA β 

Figure S1 – Raw ThT diagrams for 5 repetitions of all 9 samples from the ZnA β experiment.

A.4 CuA β - Experiment #1

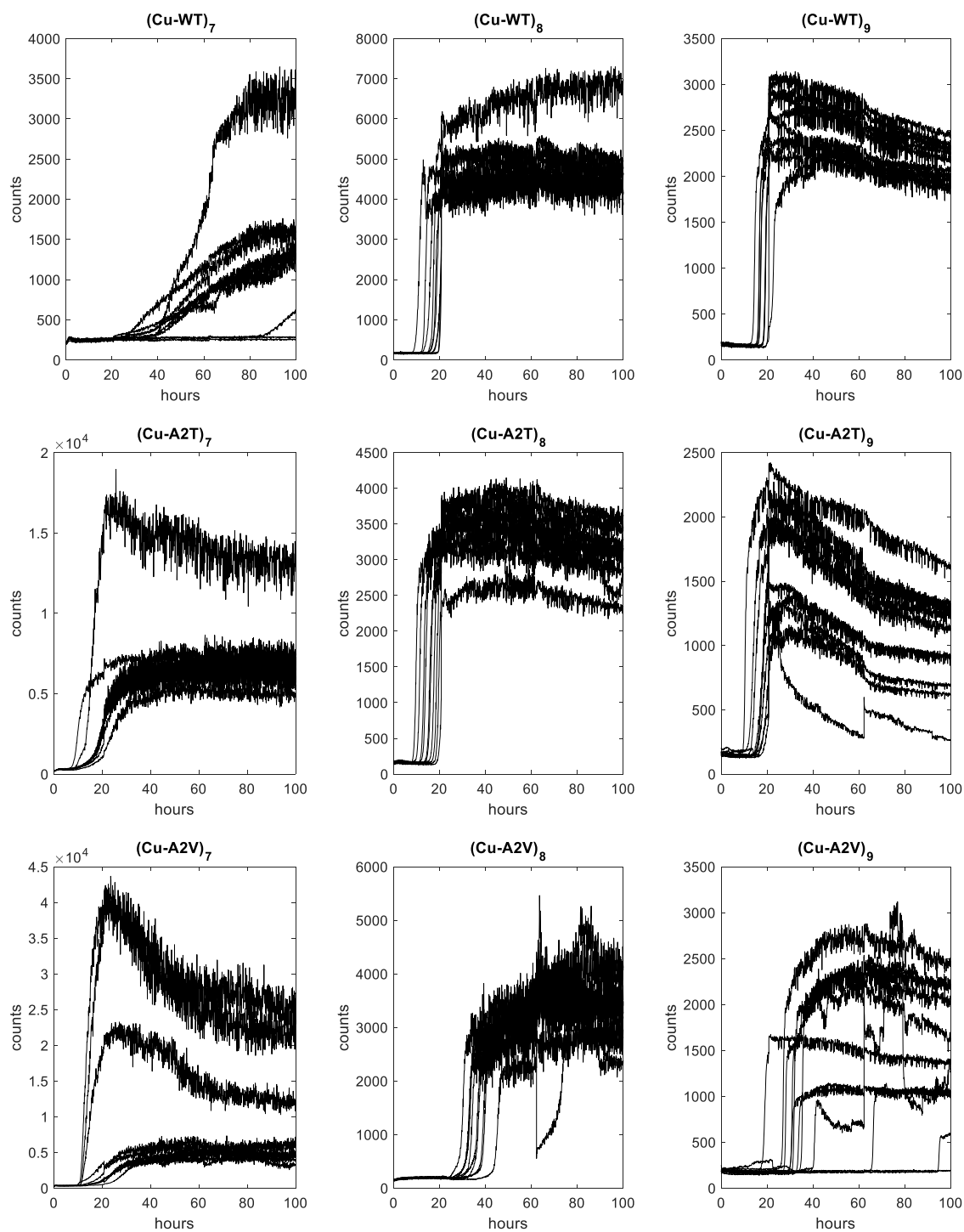


Figure S2 - Raw ThT diagrams for 10 repetitions of all 9 samples from the CuA β experiment #1.

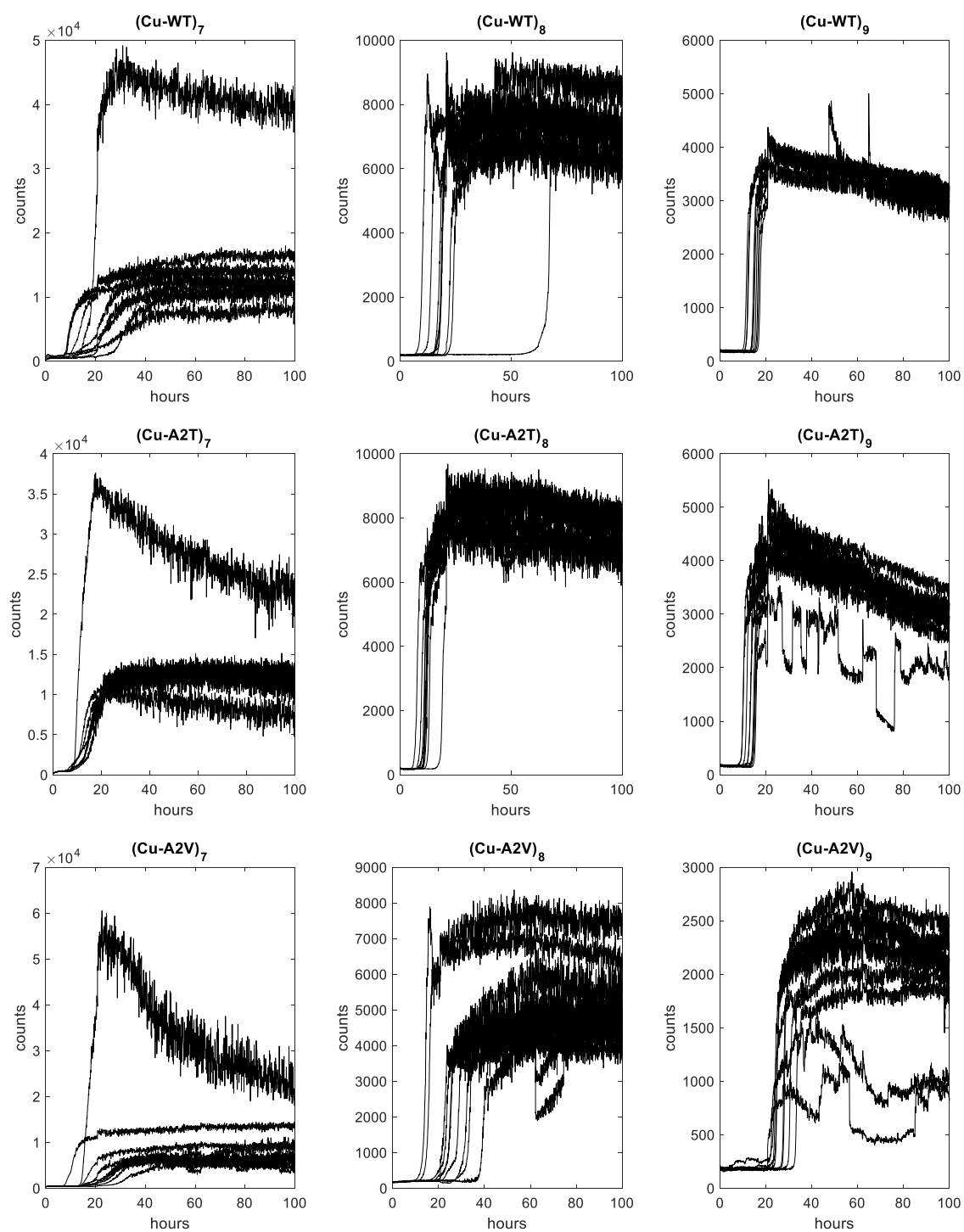
A.5 CuA β - Experiment #2

Figure S3 – Raw ThT diagrams for 10 repetitions of all 9 samples from CuA β experiment #2.

Appendix B

EXAFS Refinements of CuA β

B.1 Introduction

The data on Cu(II)A β collected at ESRF was analyzed using *Excurve*. Multiple models were used, differing in ligand types and numbers. Each model was varied in distances, Debye-Waller factors, and angles before refinement cycles in *Excurve*.

The models that did not achieve the best fit will have tried to compensate for this by adjusting parameters. The aspect of this is that while four different models had four different distances to the histidines, this may have been affected by the lack of something in the model. While the best fit of the 3His1N1O model to the (WT-A β)₈ found the histidines at 1.98 Å and the best fit of the 2His1Glu found them at 1.96 Å, the shorter distances might compensate for the lack of histidines in the model and vice versa.

In the following, each dataset is presented with the best fit achieved for each model that was used. The samples will be denoted (M-*var*)_{pH}, where M is the metal and *var* is the variant of A β , either wild-type (WT), A2T or A2V.

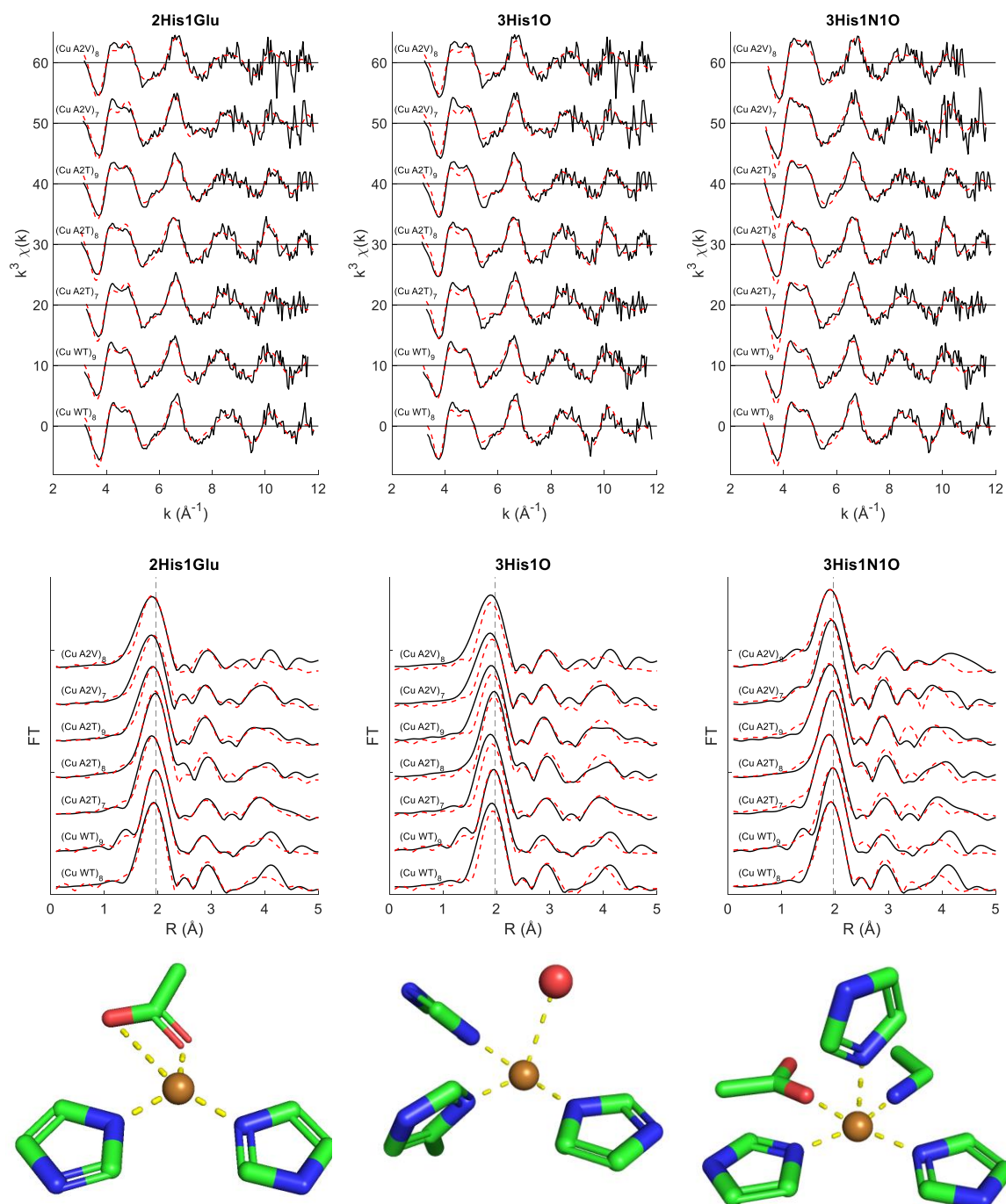
B.2 $\chi(k)$ and FT Fits

Figure S4 – Top: k^3 -weighted $\chi(k)$ spectra for the seven datasets (black) compared with the theoretical spectrum (dashed red) for the refined model shown in the bottom. Middle: FT of the spectra for the seven datasets (black) compared with the ditto for the theoretical spectra.

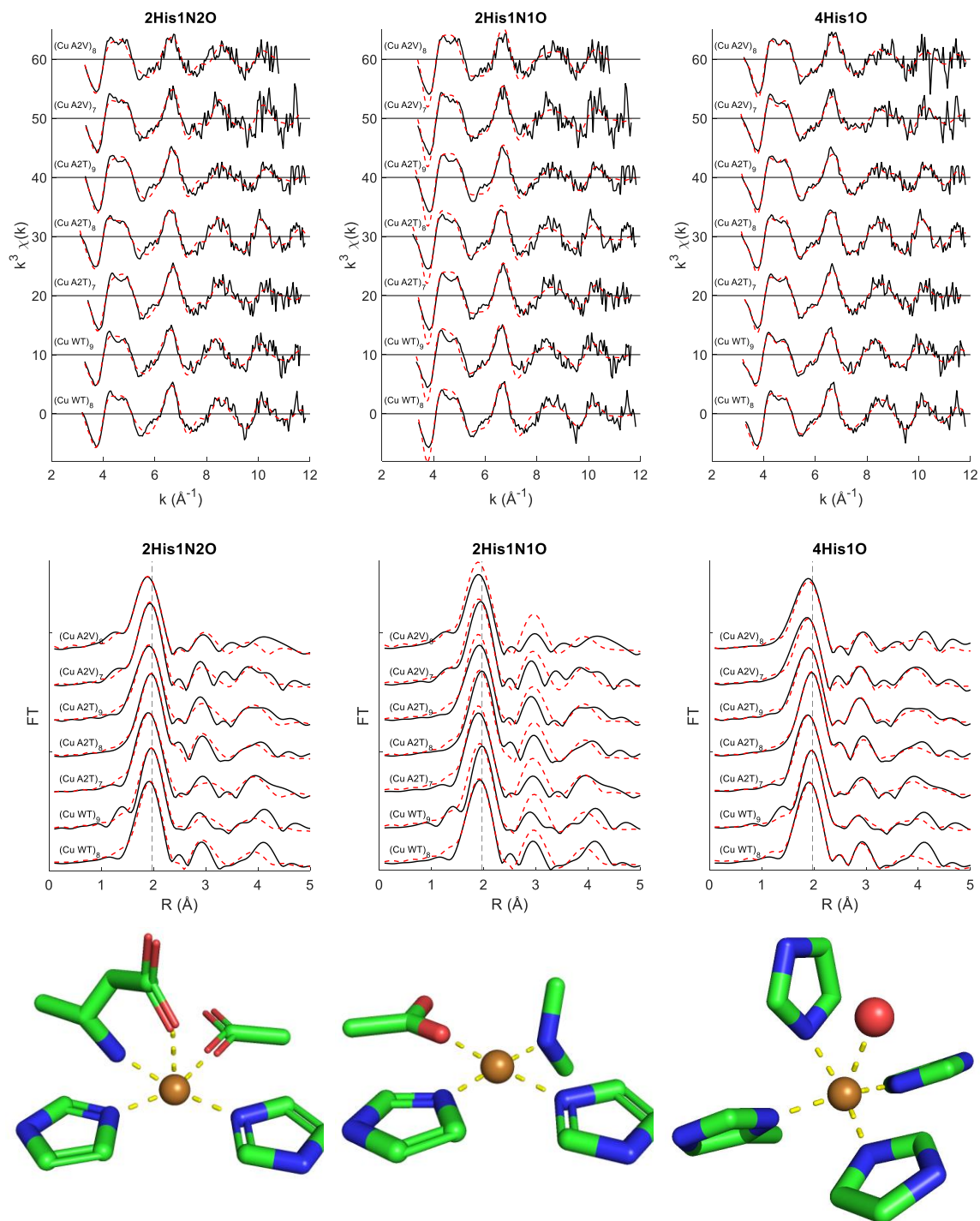


Figure S4 (cont.)

B.3 Fit Parameters

B.3.1 2His1Glu

Table S5 – Parameters for the best fits achieved with the 2His1Glu model for CuA β . N is the shell occupation number, R is the shell distance, σ_{DW} is the Debye-Waller factor, E_f is the Fermi energy, R_{EXAFS} is the quality of fit. σ is a statistical standard deviation, calculated from the correlation coefficients. N_{pars} is the number of parameters refined to achieve the fit, and E_{fit} is the energy range above the edge of the experimental data that was included.

Ligand	N	$R \pm 2\sigma$ (Å)	$\sigma_{DW}^2 \pm 2\sigma$ (Å ²)	ΔE_f (eV)	R_{EXAFS}
			(Cu-WT) ₈		
His	2	1.96 ± 0.01	0.004 ± 0.002	-10	31%
O _{δ1} (Glu)	1	2.00 ± 0.03	0.007 ± 0.003		
O _{δ2} (Glu)	1	2.78 ± 0.03	0.007 ± 0.003		
			(Cu-WT) ₉		
His	2	2.009 ± 0.009	0.003 ± 0.002	-10	31%
O _{δ1} (Glu)	1	1.97 ± 0.07	0.02 ± 0.01		
O _{δ2} (Glu)	1	3.31 ± 0.07	0.02 ± 0.01		
			(Cu-A2T) ₇		
His	2	1.98 ± 0.02	0.007 ± 0.003	-9	32%
O _{δ1} (Glu)	1	1.95 ± 0.01	0.005 ± 0.003		
O _{δ2} (Glu)	1	3.23 ± 0.01	0.005 ± 0.003		
			(Cu-A2T) ₈		
His	2	2.00 ± 0.01	0.006 ± 0.001	-13	33%
O _{δ1} (Glu)	1	1.97 ± 0.01	0.004 ± 0.003		
O _{δ2} (Glu)	1	3.16 ± 0.01	0.004 ± 0.003		
			(Cu-A2T) ₉		
His	2	1.94 ± 0.02	0.004 ± 0.003	-11	31%
O _{δ1} (Glu)	1	2.02 ± 0.02	0.004 ± 0.004		
O _{δ2} (Glu)	1	3.17 ± 0.02	0.004 ± 0.004		
			(Cu-A2V) ₇		
His	2	2.00 ± 0.02	0.008 ± 0.004	-11	41%
O _{δ1} (Glu)	1	1.92 ± 0.04	0.006 ± 0.003		
O _{δ2} (Glu)	1	3.34 ± 0.04	0.006 ± 0.003		
			(Cu-A2V) ₈		
His	2	1.97 ± 0.02	0.007 ± 0.004	-11	41%
O _{δ1} (Glu)	1	1.93 ± 0.03	0.007 ± 0.004		
O _{δ2} (Glu)	1	3.20 ± 0.03	0.007 ± 0.004		

B.3.2 3His10

Table S6 – Parameters for the best fits achieved with the 3His10 model for CuA β . N is the shell occupation number, R is the shell distance, σ_{DW} is the Debye-Waller factor, E_f is the Fermi energy, R_{EXAFS} is the quality of fit. σ is a statistical standard deviation, calculated from the correlation coefficients. N_{pars} is the number of parameters refined to achieve the fit, and E_{fit} is the energy range above the edge of the experimental data that was included.

Ligand	N	$R \pm 2\sigma$ (Å)	$\sigma_{DW}^2 \pm 2\sigma$ (Å ²)	ΔE_f (eV)	R_{EXAFS}
			(Cu-WT) ₈		
His	3	1.979 ± 0.007	0.005 ± 0.001	-8.7	31%
O	1	2.69 ± 0.03	0.005 ± 0.004		
			$N_{pars} = 7, E = 30-529$ eV		
			(Cu-WT) ₉		
His	3	2.014 ± 0.007	0.004 ± 0.001	-11.7	29%
O	1	2.32 ± 0.04	0.014 ± 0.007		
			$N_{pars} = 7, E = 30-513$ eV		
			(Cu-A2T) ₇		
His	3	1.977 ± 0.008	0.005 ± 0.001	-10.3	31%
O	1	2.19 ± 0.05	0.020 ± 0.001		
			$N_{pars} = 7, E = 30-513$ eV		
			(Cu-A2T) ₈		
His	3	1.991 ± 0.007	0.004 ± 0.001	-12.2	32%
O	1	2.69 ± 0.03	0.003 ± 0.003		
			$N_{pars} = 7, E = 30-534$ eV		
			(Cu-A2T) ₉		
His	3	1.976 ± 0.009	0.006 ± 0.001	-11.5	35%
O	1	2.7 ± 0.1	0.02 ± 0.02		
			$N_{pars} = 7, E = 30-532$ eV		
			(Cu-A2V) ₇		
His	3	1.96 ± 0.01	0.007 ± 0.001	-11	43%
O	1	2.65 ± 0.05	0.006 ± 0.006		
			$N_{pars} = 7, E = 30-534$ eV		
			(Cu-A2V) ₈		
His	3	1.96 ± 0.01	0.006 ± 0.001	-10	43%
O	1	2.68 ± 0.05	0.007 ± 0.008		
			$N_{pars} = 7, E = 30-533$ eV		

B.3.3 3His1N10

Table S7 – Parameters for the best fits achieved with the 3His1N10 model for CuA β . N is the shell occupation number, R is the shell distance, σ_{DW} is the Debye-Waller factor, E_f is the Fermi energy, R_{EXAFS} is the quality of fit. σ is a statistical standard deviation, calculated from the correlation coefficients. N_{pars} is the number of parameters refined to achieve the fit, and E_{fit} is the energy range above the edge of the experimental data that was included.

Ligand	N	$R \pm 2\sigma$ (Å)	$\sigma_{DW}^2 \pm 2\sigma$ (Å ²)	ΔE_f (eV)	R_{EXAFS}
(Cu-WT) ₈					
His	2	1.982 ± 0.008	0.008 ± 0.001	-11.4	30%
N (Asp1)	1	1.982 ± 0.008	0.008 ± 0.001		
O $_{\delta 1}$ (Glu)	1	1.982 ± 0.008	0.008 ± 0.001		
His	1	2.31 ± 0.01	0.002 ± 0.002		
$N_{pars} = 9, E = 30-534$ eV					
(Cu-WT) ₉					
His	2	1.999 ± 0.009	0.008 ± 0.001	-9	36%
N (Asp1)	1	1.999 ± 0.009	0.008 ± 0.001		
O $_{\delta 1}$ (Glu)	1	1.999 ± 0.009	0.008 ± 0.001		
His	1	2.34 ± 0.02	0.003 ± 0.002		
$N_{pars} = 9, E = 30-513$ eV					
(Cu-A2T) ₇					
His	2	1.967 ± 0.009	0.008 ± 0.002	-8.9	39%
N (Asp1)	1	1.967 ± 0.009	0.008 ± 0.002		
O $_{\delta 1}$ (Glu)	1	1.967 ± 0.009	0.008 ± 0.002		
His	1	2.215 ± 0.009	0.010 ± 0.007		
$N_{pars} = 9, E = 30-513$ eV					
(Cu-A2T) ₈					
His	2	1.993 ± 0.008	0.008 ± 0.001	-12.1	30%
N (Asp1)	1	1.993 ± 0.008	0.008 ± 0.001		
O $_{\delta 1}$ (Glu)	1	1.993 ± 0.008	0.008 ± 0.001		
His	1	2.33 ± 0.01	0.001 ± 0.002		
$N_{pars} = 9, E = 30-534$ eV					
(Cu-A2T) ₉					
His	2	1.963 ± 0.009	0.009 ± 0.001	-11	36%
N (Asp1)	1	1.963 ± 0.009	0.009 ± 0.001		
O $_{\delta 1}$ (Glu)	1	1.963 ± 0.009	0.009 ± 0.001		
His	1	2.22 ± 0.02	0.01 ± 0.02		
$N_{pars} = 9, E = 30-532$ eV					
(Cu-A2V) ₇					
His	2	1.97 ± 0.03	0.007 ± 0.001	-9	41%
N (Asp1)	1	1.97 ± 0.03	0.007 ± 0.001		
O $_{\delta 1}$ (Glu)	1	1.97 ± 0.03	0.007 ± 0.001		
His	1	2.25 ± 0.03	0.008 ± 0.008		
$N_{pars} = 9, E = 30-513$ eV					
(Cu-A2V) ₈					
His	2	1.97 ± 0.01	0.008 ± 0.001	-9	39%
N (Asp1)	1	1.97 ± 0.01	0.008 ± 0.001		
O $_{\delta 1}$ (Glu)	1	1.97 ± 0.01	0.008 ± 0.001		
His	1	2.22 ± 0.03	0.008 ± 0.006		
$N_{pars} = 9, E = 30-442$ eV					

B.3.4 2His1N2O

Table S8 – Parameters for the best fits achieved with the 2His1N2O model for CuA β . N is the shell occupation number, R is the shell distance, σ_{DW} is the Debye-Waller factor, E_f is the Fermi energy, R_{EXAFS} is the quality of fit. σ is a statistical standard deviation, calculated from the correlation coefficients. N_{pars} is the number of parameters refined to achieve the fit, and E_{fit} is the energy range above the edge of the experimental data that was included.

Ligand	N	$R \pm 2\sigma$ (Å)	$\sigma_{DW}^2 \pm 2\sigma$ (Å ²)	ΔE_f (eV)	R_{EXAFS}
(Cu-WT) ₈					
His	2	1.987 ± 0.009	0.008 ± 0.001	-12	35%
N (Asp1)	1	1.987 ± 0.009	0.008 ± 0.001		
O _{δ1} (Glu)	1	1.987 ± 0.009	0.008 ± 0.001		
O _{ϵ1} (Asp1)	1	2.31 ± 0.02	0.010 ± 0.006		
$N_{pars} = 8, E = 30-534$ eV					
(Cu-WT) ₉					
His	2	2.01 ± 0.01	0.008 ± 0.001	-10	36%
N (Asp1)	1	2.01 ± 0.01	0.008 ± 0.001		
O _{δ1} (Glu)	1	2.01 ± 0.01	0.008 ± 0.001		
O _{ϵ1} (Asp1)	1	2.34 ± 0.02	0.005 ± 0.003		
$N_{pars} = 8, E = 30-513$ eV					
(Cu-A2T) ₇					
His	2	1.96 ± 0.01	0.009 ± 0.001	-7	34%
N (Asp1)	1	1.96 ± 0.01	0.009 ± 0.001		
O _{δ1} (Glu)	1	1.96 ± 0.01	0.009 ± 0.001		
O _{ϵ1} (Asp1)	1	2.36 ± 0.03	0.011 ± 0.004		
$N_{pars} = 8, E = 30-513$ eV					
(Cu-A2T) ₈					
His	2	2.00 ± 0.02	0.008 ± 0.002	-14	31%
N (Asp1)	1	2.00 ± 0.02	0.008 ± 0.002		
O _{δ1} (Glu)	1	2.00 ± 0.02	0.008 ± 0.002		
O _{ϵ1} (Asp1)	1	2.32 ± 0.02	0.002 ± 0.003		
$N_{pars} = 8, E = 30-534$ eV					
(Cu-A2T) ₉					
His	2	1.97 ± 0.01	0.009 ± 0.001	-11	37%
N (Asp1)	1	1.97 ± 0.01	0.009 ± 0.001		
O _{δ1} (Glu)	1	1.97 ± 0.01	0.009 ± 0.001		
O _{ϵ1} (Asp1)	1	2.36 ± 0.05	0.02 ± 0.01		
$N_{pars} = 8, E = 30-532$ eV					
(Cu-A2V) ₇					
His	2	1.98 ± 0.01	0.008 ± 0.001	-9	42%
N (Asp1)	1	1.98 ± 0.01	0.008 ± 0.001		
O _{δ1} (Glu)	1	1.98 ± 0.01	0.008 ± 0.001		
O _{ϵ1} (Asp1)	1	2.32 ± 0.01	0.005 ± 0.004		
$N_{pars} = 8, E = 30-513$ eV					
(Cu-A2V) ₈					
His	2	1.98 ± 0.01	0.009 ± 0.001	-10	38%
N (Asp1)	1	1.98 ± 0.01	0.009 ± 0.001		
O _{δ1} (Glu)	1	1.98 ± 0.01	0.009 ± 0.001		
O _{ϵ1} (Asp1)	1	2.28 ± 0.03	0.008 ± 0.005		
$N_{pars} = 8, E = 30-442$ eV					

B.3.5 2His1N10

Table S9 – Parameters for the best fits achieved with the 2His1N10 model for CuA β . N is the shell occupation number, R is the shell distance, σ_{DW} is the Debye-Waller factor, E_f is the Fermi energy, R_{EXAFS} is the quality of fit. σ is a statistical standard deviation, calculated from the correlation coefficients. N_{pars} is the number of parameters refined to achieve the fit, and E_{fit} is the energy range above the edge of the experimental data that was included.

Ligand	N	$R \pm 2\sigma$ (Å)	$\sigma_{DW}^2 \pm 2\sigma$ (Å ²)	ΔE_f (eV)	R_{EXAFS}
(Cu-WT) ₈					
His	2	1.97 ± 0.01	0.008 ± 0.001	-8	39%
N (backbone)	1	1.97 ± 0.01	0.008 ± 0.001		
O _{δ1} (Glu)	1	1.97 ± 0.01	0.008 ± 0.001		
$N_{pars} = 6, E = 30-534$ eV					
(Cu-WT) ₉					
His	2	1.99 ± 0.01	0.008 ± 0.001	-8	44%
N (backbone)	1	1.99 ± 0.01	0.008 ± 0.001		
O _{δ1} (Glu)	1	1.99 ± 0.01	0.008 ± 0.001		
$N_{pars} = 6, E = 30-513$ eV					
(Cu-A2T) ₇					
His	2	1.96 ± 0.01	0.008 ± 0.001	-7	41%
N (backbone)	1	1.96 ± 0.01	0.008 ± 0.001		
O _{δ1} (Glu)	1	1.96 ± 0.01	0.008 ± 0.001		
$N_{pars} = 6, E = 30-513$ eV					
(Cu-A2T) ₈					
His	2	1.99 ± 0.01	0.008 ± 0.001	-11	44%
N (backbone)	1	1.99 ± 0.01	0.008 ± 0.001		
O _{δ1} (Glu)	1	1.99 ± 0.01	0.008 ± 0.001		
$N_{pars} = 6, E = 30-534$ eV					
(Cu-A2T) ₉					
His	2	1.96 ± 0.01	0.008 ± 0.001	-10	41%
N (backbone)	1	1.96 ± 0.01	0.008 ± 0.001		
O _{δ1} (Glu)	1	1.96 ± 0.01	0.008 ± 0.001		
$N_{pars} = 6, E = 30-532$ eV					
(Cu-A2V) ₇					
His	2	1.97 ± 0.01	0.008 ± 0.001	-7	47%
N (backbone)	1	1.97 ± 0.01	0.008 ± 0.001		
O _{δ1} (Glu)	1	1.97 ± 0.01	0.008 ± 0.001		
$N_{pars} = 6, E = 30-513$ eV					
(Cu-A2V) ₈					
His	2	1.96 ± 0.01	0.008 ± 0.001	-7	43%
N (backbone)	1	1.96 ± 0.01	0.008 ± 0.001		
O _{δ1} (Glu)	1	1.96 ± 0.01	0.008 ± 0.001		
$N_{pars} = 6, E = 30-442$ eV					

B.3.6 4His10

Table S10 – Parameters for the best fits achieved with the 4His10 model for CuA β . N is the shell occupation number, R is the shell distance, α and β are the twist and tilt angles for the histidines, σ_{DW} is the Debye-Waller factor, E_f is the Fermi energy, R_{EXAFS} is the quality of fit. σ is a statistical standard deviation, calculated from the correlation coefficients. N_{pars} is the number of parameters refined to achieve the fit, and E_{fit} is the energy range above the edge of the experimental data that was included.

Ligand	N	$R \pm 2\sigma$ (Å)	α / β (°)	$\sigma_{DW}^2 \pm 2\sigma$ (Å ²)	ΔE_f (eV)	R_{EXAFS}
(Cu-WT) ₈						
His	1	1.93 ± 0.01	-6 / -3	0.001 ± 0.002	-9	26%
His	1	1.93 ± 0.01	11 / -6	0.001 ± 0.002		
His	1	1.93 ± 0.01	13 / -44	0.001 ± 0.002		
His	1	2.07 ± 0.02	27 / -21	0.001 ± 0.002		
O	1	2.30 ± 0.01		0.002 ± 0.005		
$N_{pars} = 8, E = 30-529$ eV						
(Cu-WT) ₉						
His	1	1.99 ± 0.05	0 / -8	0.004 ± 0.002	-12	28%
His	1	2.01 ± 0.04	9 / -6	0.004 ± 0.002		
His	1	2.03 ± 0.07	34 / -1	0.004 ± 0.002		
His	1	2.20 ± 0.04	32 / -9	0.004 ± 0.002		
O	1	2.39 ± 0.03		0.002 ± 0.002		
$N_{pars} = 10, E = 30-529$ eV						
(Cu-A2T) ₇						
His	1	1.90 ± 0.03	0 / -8	0.001 ± 0.002	-9	30%
His	1	1.95 ± 0.02	9 / -7	0.001 ± 0.002		
His	1	2.04 ± 0.02	34 / -1	0.001 ± 0.002		
His	1	2.10 ± 0.03	32 / -9	0.001 ± 0.002		
O	1	2.31 ± 0.03		0.004 ± 0.003		
$N_{pars} = 10, E = 30-513$ eV						
(Cu-A2T) ₈						
His	1	1.91 ± 0.03	0 / -8	0.002 ± 0.003	-13	26%
His	1	1.97 ± 0.02	9 / -6	0.002 ± 0.003		
His	1	2.05 ± 0.03	33 / -1	0.002 ± 0.003		
His	1	2.08 ± 0.03	32 / -9	0.002 ± 0.003		
O	1	2.31 ± 0.02		0.001 ± 0.002		
$N_{pars} = 10, E = 30-534$ eV						
(Cu-A2T) ₉						
His	1	1.92 ± 0.03	4 / -8	0.002 ± 0.002	-13	28%
His	1	1.94 ± 0.02	5 / -7	0.002 ± 0.002		
His	1	2.06 ± 0.05	45 / -1	0.002 ± 0.002		
His	1	2.07 ± 0.02	20 / -9	0.002 ± 0.002		
O	1	2.28 ± 0.03		0.004 ± 0.004		
$N_{pars} = 10, E = 30-532$ eV						
(Cu-A2V) ₇						
His	1	1.88 ± 0.03	4 / -8	0.001 ± 0.001	-13	38%
His	1	1.96 ± 0.04	5 / -6	0.001 ± 0.001		
His	1	2.04 ± 0.07	45 / -1	0.001 ± 0.001		
His	1	2.10 ± 0.05	20 / -9	0.001 ± 0.001		
O	1	2.25 ± 0.03		0.002 ± 0.004		
$N_{pars} = 10, E = 30-534$ eV						
(Cu-A2V) ₈						
His	1	1.87 ± 0.03	4 / -8	0.001 ± 0.001	-11	39%
His	1	1.95 ± 0.04	5 / -6	0.001 ± 0.001		
His	1	2.01 ± 0.06	46 / -1	0.001 ± 0.001		
His	1	2.09 ± 0.04	20 / -9	0.001 ± 0.001		
O	1	2.29 ± 0.02		0.004 ± 0.005		
$N_{pars} = 10, E = 30-533$ eV						

Appendix C

EXAFS Refinements of ZnA β

C.1 Introduction

The ZnA β data collected at SOLEIL was analyzed thoroughly using EXCURVE. Using the experience earned from the refinements of CuA β , the E_f parameter was refined initially with only the first shell of atoms included in the model. Based on the refined E_f , the E_0 in the data treatment was changed, and used onward.

The models used vary in number of histidines and carboxylate groups, but keep a coordination number of four. The occupation number, N , for all shells was kept constant at 1. The samples will be denoted (M-*var*)_{pH}, where M is the metal and *var* is the variant of A β , either wild-type (WT), A2T or A2V.

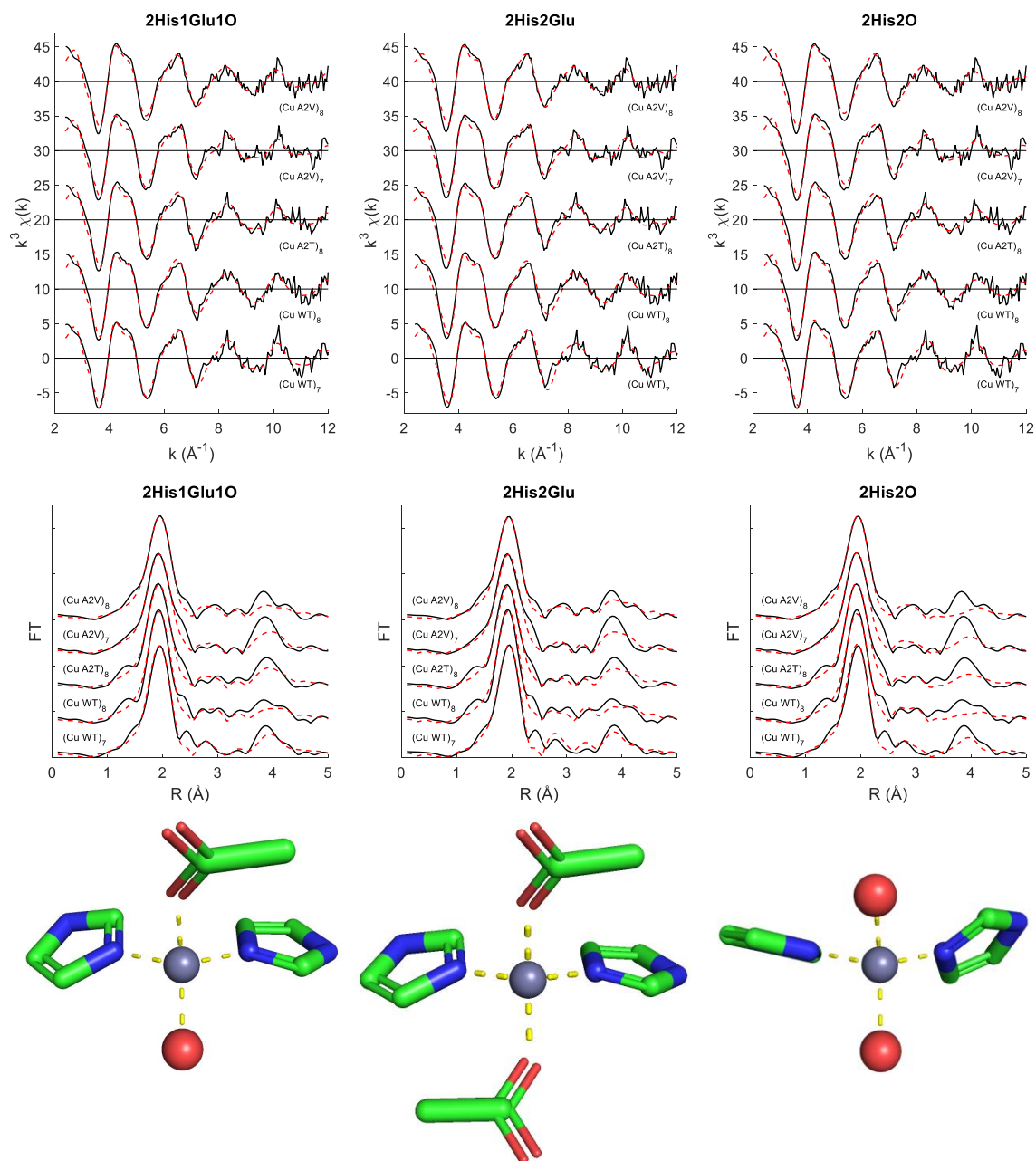
C.2 $\chi(k)$ and FT Fits

Figure S11 – Top: k^3 -weighted $\chi(k)$ spectra for the seven datasets (black) compared with the theoretical spectrum (dashed red) for the refined model shown in the bottom. Middle: FT of the spectra for the seven datasets (black) compared with the ditto for the theoretical spectra.

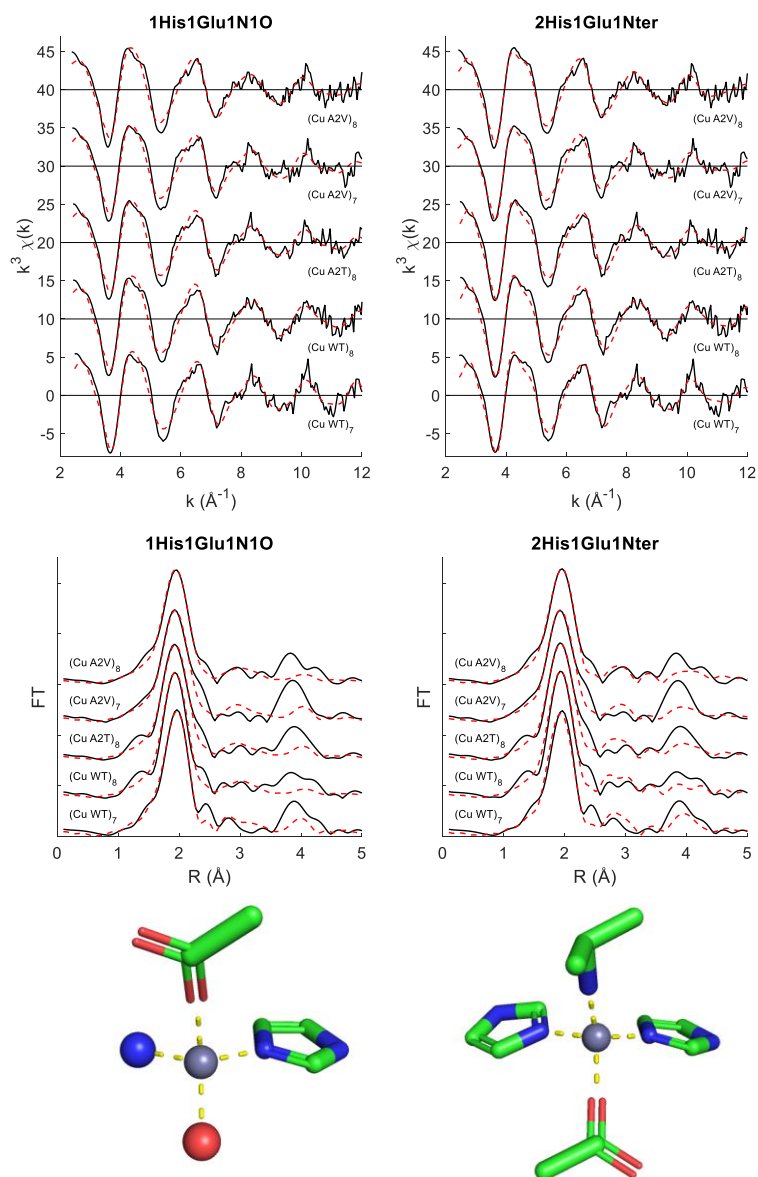


Figure S11 (cont.)

C.3 Fit Parameters

C.3.1 2His1Glu1O

Table S12 – Parameters for the best fits achieved with the 2His1Glu1O model for ZnA β . N is the shell occupation number, R is the shell distance, σ_{DW} is the Debye-Waller factor, E_f is the Fermi energy, R_{EXAFS} is the quality of fit. σ is a statistical standard deviation, calculated from the correlation coefficients. α and β are the twist and tilt angles, respectively.

Ligand	N	$R \pm 2\sigma$ (Å)	α / β (°)	$\sigma_{DW}^2 \pm 2\sigma$ (Å ²)	ΔE_f (eV)	R_{EXAFS}
(Zn-WT) ₇						
His	1	1.94 ± 0.08	0 / 0	0.006 ± 0.004	-1	26%
His	1	2.03 ± 0.09	0 / 0	0.006 ± 0.004		
O _{δ1} (Glu/Asp)	1	2.00 ± 0.04	28 / 15	0.006 ± 0.004		
O	1	1.98 ± 0.06		0.006 ± 0.004		
(Zn-WT) ₈						
His	1	2.0 ± 0.3	0 / 0	0.006 ± 0.004	0	25%
His	1	2.0 ± 0.3	0 / 0	0.006 ± 0.004		
O _{δ1} (Glu/Asp)	1	2.02 ± 0.06	30 / 19	0.006 ± 0.004		
O	1	1.94 ± 0.06		0.006 ± 0.004		
(Zn-A2T) ₈						
His	1	1.95 ± 0.03	0 / 0	0.005 ± 0.002	0	26%
His	1	2.05 ± 0.03	0 / 0	0.005 ± 0.002		
O _{δ1} (Glu/Asp)	1	2.03 ± 0.04	26 / 21	0.005 ± 0.002		
O	1	1.93 ± 0.04		0.005 ± 0.002		
(Zn-A2V) ₇						
His	1	1.93 ± 0.03	0 / 0	0.005 ± 0.002	-1	29%
His	1	2.08 ± 0.03	0 / 0	0.005 ± 0.002		
O _{δ1} (Glu/Asp)	1	1.95 ± 0.04	24 / 15	0.005 ± 0.002		
O	1	2.01 ± 0.05		0.005 ± 0.002		
(Zn-A2V) ₈						
His	1	1.93 ± 0.01	0 / 0	0.005 ± 0.002	0	28%
His	1	2.05 ± 0.05	0 / 0	0.005 ± 0.002		
O _{δ1} (Glu/Asp)	1	2.02 ± 0.07	24 / 21	0.005 ± 0.002		
O	1	1.97 ± 0.05		0.005 ± 0.002		

C.3.2 2His2Glu

Table S13 – Parameters for the best fits achieved with the 2His2Glu model for ZnA β . N is the shell occupation number, R is the shell distance, σ_{DW} is the Debye-Waller factor, E_f is the Fermi energy, R_{EXAFS} is the quality of fit. σ is a statistical standard deviation, calculated from the correlation coefficients. α and β are the twist and tilt angles, respectively.

Ligand	N	$R \pm 2\sigma$ (Å)	α / β (°)	$\sigma_{DW}^2 \pm 2\sigma$ (Å ²)	ΔE_f (eV)	R_{EXAFS}
(Zn-WT) ₇						
His	1	1.90 ± 0.06	0 / 0	0.004 ± 0.003	1	28%
His	1	2.01 ± 0.08	0 / 0	0.004 ± 0.003		
O _{δ_1} (Glu/Asp)	2	2.00 ± 0.04	27 / 19	0.004 ± 0.003		
(Zn-WT) ₈						
His	1	1.9 ± 0.3	0 / 0	0.006 ± 0.009	1	26%
His	1	2.0 ± 0.2	0 / 0	0.006 ± 0.009		
O _{δ_1} (Glu/Asp)	2	1.99 ± 0.04	29 / 15	0.006 ± 0.009		
(Zn-A2T) ₈						
His	1	1.95 ± 0.07	0 / 0	0.006 ± 0.002	0	27%
His	1	2.08 ± 0.08	0 / 0	0.006 ± 0.002		
O _{δ_1} (Glu/Asp)	2	1.97 ± 0.03	22 / 18	0.006 ± 0.002		
(Zn-A2V) ₇						
His	1	1.95 ± 0.07	0 / 0	0.007 ± 0.002	-1	30%
His	1	2.07 ± 0.07	0 / 0	0.007 ± 0.002		
O _{δ_1} (Glu/Asp)	2	1.98 ± 0.03	21 / 22	0.007 ± 0.002		
(Zn-A2V) ₈						
His	1	1.95 ± 0.07	0 / 0	0.006 ± 0.003	0	27%
His	1	2.06 ± 0.09	0 / 0	0.006 ± 0.003		
O _{δ_1} (Glu/Asp)	2	1.99 ± 0.03	25 / 17	0.006 ± 0.003		

C.3.3 2His2O

Table S14 – Parameters for the best fits achieved with the 2His2O model for ZnA β . N is the shell occupation number, R is the shell distance, σ_{DW} is the Debye-Waller factor, E_f is the Fermi energy, R_{EXAFS} is the quality of fit. σ is a statistical standard deviation, calculated from the correlation coefficients.

Ligand	N	$R \pm 2\sigma$ (Å)	$\sigma_{DW}^2 \pm 2\sigma$ (Å ²)	ΔE_f (eV)	R_{EXAFS}
(Zn-WT) ₇					
His	1	1.92 ± 0.03	0.005 ± 0.001	0	29
His	1	2.04 ± 0.04	0.005 ± 0.001		
O	2	1.99 ± 0.01	0.005 ± 0.001		
(Zn-WT) ₈					
His	1	1.90 ± 0.02	0.003 ± 0.001	0	27
His	1	2.09 ± 0.02	0.003 ± 0.001		
O	2	1.97 ± 0.01	0.003 ± 0.001		
(Zn-A2T) ₈					
His	1	1.92 ± 0.02	0.004 ± 0.001	0	28
His	1	2.09 ± 0.03	0.004 ± 0.001		
O	2	1.98 ± 0.01	0.004 ± 0.001		
(Zn-A2V) ₇					
His	1	1.92 ± 0.03	0.006 ± 0.001	0	32
His	1	2.07 ± 0.03	0.006 ± 0.001		
O	2	1.98 ± 0.01	0.006 ± 0.001		
(Zn-A2V) ₈					
His	1	1.93 ± 0.04	0.006 ± 0.001	-1	30
His	1	2.06 ± 0.03	0.006 ± 0.001		
O	2	1.99 ± 0.01	0.006 ± 0.001		

C.3.4 1His1Glu1N1O

Table S15 – Parameters for the best fits achieved with the 1His1Glu1N1O model for ZnA β . N is the shell occupation number, R is the shell distance, σ_{DW} is the Debye-Waller factor, E_f is the Fermi energy, R_{EXAFS} is the quality of fit. σ is a statistical standard deviation, calculated from the correlation coefficients.

Ligand	N	$R \pm 2\sigma$ (Å)	$\sigma_{DW}^2 \pm 2\sigma$ (Å ²)	ΔE_f (eV)	R_{EXAFS}
(Zn-WT) ₇					
His	1	1.96 ± 0.03	0.002 ± 0.002	1	29
N	1	1.86 ± 0.02	0.002 ± 0.002		
O _{δ_1} (Glu/Asp)	1	1.98 ± 0.03	0.002 ± 0.002		
O	1	2.02 ± 0.04	0.002 ± 0.002		
(Zn-WT) ₈					
His	1	2.01 ± 0.04	0.007 ± 0.003	0	29
N	1	2.0 ± 0.2	0.007 ± 0.003		
O _{δ_1} (Glu/Asp)	1	1.98 ± 0.03	0.007 ± 0.003		
O	1	2.0 ± 0.2	0.007 ± 0.003		
(Zn-A2T) ₈					
His	1	2.00 ± 0.03	0.008 ± 0.002	0	31
N	1	2.0 ± 0.2	0.008 ± 0.002		
O _{δ_1} (Glu/Asp)	1	1.97 ± 0.03	0.008 ± 0.002		
O	1	2.0 ± 0.2	0.008 ± 0.002		
(Zn-A2V) ₇					
His	1	2.01 ± 0.03	0.01 ± 0.02	0	35
N	1	1.94 ± 0.02	0.01 ± 0.02		
O _{δ_1} (Glu/Asp)	1	1.98 ± 0.03	0.01 ± 0.02		
O	1	2.0 ± 0.2	0.01 ± 0.02		
(Zn-A2V) ₈					
His	1	2.01 ± 0.04	0.007 ± 0.004	-1	31
N	1	2.1 ± 0.1	0.007 ± 0.004		
O _{δ_1} (Glu/Asp)	1	1.97 ± 0.03	0.007 ± 0.004		
O	1	1.96 ± 0.09	0.007 ± 0.004		

C.3.5 2His1Glu1N

Table S16 – Parameters for the best fits achieved with the 2His1Glu1N model for ZnA β . N is the shell occupation number, R is the shell distance, σ_{DW} is the Debye-Waller factor, E_f is the Fermi energy, R_{EXAFS} is the quality of fit. σ is a statistical standard deviation, calculated from the correlation coefficients.

Ligand	N	$R \pm 2\sigma$ (Å)	$\sigma_{DW}^2 \pm 2\sigma$ (Å ²)	ΔE_f (eV)	R_{EXAFS}
(Zn-WT) ₇					
His	1	1.93 ± 0.04	0.004 ± 0.001	1	30
His	1	2.04 ± 0.03	0.004 ± 0.001		
N (Asp1)	1	2.02 ± 0.03	0.004 ± 0.001		
O	1	1.95 ± 0.02	0.004 ± 0.001		
(Zn-WT) ₈					
His	1	1.91 ± 0.02	0.003 ± 0.001	1	30
His	1	2.06 ± 0.02	0.003 ± 0.001		
N (Asp1)	1	2.01 ± 0.02	0.003 ± 0.001		
O	1	1.95 ± 0.02	0.003 ± 0.001		
(Zn-A2T) ₈					
His	1	1.93 ± 0.03	0.005 ± 0.001	1	30
His	1	2.05 ± 0.03	0.005 ± 0.001		
N (Asp1)	1	2.03 ± 0.03	0.005 ± 0.001		
O	1	1.95 ± 0.02	0.005 ± 0.001		
(Zn-A2V) ₇					
His	1	2.02 ± 0.03	0.004 ± 0.002	-1	34
His	1	2.09 ± 0.04	0.004 ± 0.002		
N (Asp1)	1	1.98 ± 0.03	0.004 ± 0.002		
O	1	1.93 ± 0.02	0.004 ± 0.002		
(Zn-A2V) ₈					
His	1	2.02 ± 0.09	0.010 ± 0.003	0	30
His	1	2.1 ± 0.1	0.010 ± 0.003		
N (Asp1)	1	2.02 ± 0.03	0.010 ± 0.003		
O	1	1.91 ± 0.02	0.010 ± 0.003		